LBL-30043
UC-800

Lawrence Berkeley Laboratory

UNIVERSITY OF CALIFORNIA

EARTH SCIENCES DIVISION

Geotechnical Support and Topical Studies for Nuclear Waste Geologic Repositories

Annual Report, Fiscal Year 1989

December 1990

LOAN COPY
Circulates
for 4 weeks
Bldg. 50 Library.
Copy 2
LBL-30043

Prepared for the U.S. Department of Energy under Contract Number DE-AC03-76SF00098

DISCLAIMER

This document was prepared as an account of work sponsored by the United States Government. While this document is believed to contain correct information, neither the United States Government nor any agency thereof, nor the Regents of the University of California, nor any of their employees, makes any warranty, express or implied, or assumes any legal responsibility for the accuracy, completeness, or usefulness of any information, apparatus, product, or process disclosed, or represents that its use would not infringe privately owned rights. Reference herein to any specific commercial product, process, or service by its trade name, trademark, manufacturer, or otherwise, does not necessarily constitute or imply its endorsement, recommendation, or favoring by the United States Government or any agency thereof, or the Regents of the University of California. The views and opinions of authors expressed herein do not necessarily state or reflect those of the United States Government or any agency thereof or the Regents of the University of California.

LBL-30043

Geotechnical Support and Topical Studies for Nuclear Waste Geologic Repositories

Annual Report, Fiscal Year 1989

Earth Sciences Division
Lawrence Berkeley Laboratory
University of California
Berkeley, California 94720

December 1990

This work was supported by and prepared for the Office of Civilian Radioactive Waste Management, Office of Facilities Siting and Development, Siting and Facilities Technology Division, of the U.S. Department of Energy under Contract No. DE-AC03-76SF00098.

Table of Contents

EXECUTIVE SUMMARY, *C.F. Tsang* 1

GEOSCIENCE TECHNICAL SUPPORT FOR NUCLEAR WASTE GEOLOGIC REPOSITORIES, *D.C. Mangold and C.F. Tsang* 19

FRACTURE STUDIES

Radionuclides in Hydrothermal Systems as Indicators of Repository Conditions, *H.A. Wollenberg, S. Flexser, and A.R. Smith* 33

Normal Joint Stiffness as a Function of spatial Geometry, *D.L. Hopkins, N.G.W. Cook, and L.R. Myer* 42

Flow Channeling in a Single Fracture as a Two-Dimensional Strongly Heterogeneous Permeable Medium, *Y.W. Tsang and C.F. Tsang* 64

Hydrologic Characterization of Faults and Other Potentially Conductive Geologic Features in the Unsaturated Zone, *I. Javandel and C. Shan* 80

Mass Transport with Chemical Reactions in a Varying Thermal Field, *C.L. Carnahan* 100

Seismic Characterization of Fracture Properties, *L.R. Myer, L.J. Pyrak-Nolte, D. Hopkins, and N.G.W. Cook* 114

Application of Geophysical Methods for Fracture Characterization, *K.H. Lee, E.L. Majer, H.F. Morrison, and T.V. McEvilly* 133

A Mechanical Model for Repeated Slip Events Along Normal Faults in the Basin and Range: Applications to Yucca Mountain, Nevada, *J.M. Kemeny* 148

PUBLICATIONS LIST 184

Executive Summary

Chin-Fu Tsang

This multidisciplinary project was initiated in fiscal year 1986. It comprises two major interrelated tasks:

1. Technical Assistance. This part of the project includes: (a) reviewing the progress of the Yucca Mountain project in the DOE Office of Civilian Radioactive Waste Management (OCRWM) Program and advising the Engineering and Geotechnology Division on significant technical issues facing it; (b) analyzing geotechnical data, reports, tests, surveys and plans for the Yucca Mountain project; (c) reviewing and commenting on major technical reports and other program documents such as Study Plans; and (d) providing scientific and technical input at technical meetings.

2. Topical Studies. This activity comprises studies on scientific and technical topics, and issues of significance to in-situ testing, test analysis methods, and site characterization of nuclear waste geologic repositories. The subjects of study were selected based on discussions with DOE staff. Currently the major task, with subtasks involving various geoscience disciplines, is a study of the mechanical, hydraulic, geophysical and geochemical properties of fractures in geologic rock masses. One additional topic, initiated at DOE's suggestion, was a consideration of studies needed for preclosure monitoring and performance confirmation of a nuclear waste repository in an unsaturated zone. This has led to a white paper and proposed work plan to DOE for

studies that would demonstrate the usefulness of particular geophysical, geohydrological, and geochemical methods appropriate for use at different spatial and temporal scales of measurement for preclosure monitoring and performance confirmation.

Two important features of this project should be pointed out here. First, this project is multidisciplinary, involving LBL staff with expertise in a broad range of earth science disciplines. As seen from the list of LBL personnel below all major geoscience disciplines are represented. This group of scientists has many years of combined experience in the nuclear waste geologic isolation problem. Many times, the major issues and results presented to DOE have undergone multidisciplinary discussions and the scrutiny by the whole LBL team.

Name	*Principal Expertise*
Chalon L. Carnahan	Geochemistry
Steven Flexser	Geology
Harold A. Wollenberg	Geology
Neville G. W. Cook	Geomechanics
Larry R. Myer	Geomechanics
Ki Ha Lee	Geophysics
Ernest L. Majer	Geophysics
Thomas V. McEvilly	Geophysics
H. Frank Morrison	Geophysics
Iraj Javandel	Hydrogeology
Marcelo J. Lippmann	Hydrogeology
Chin-Fu Tsang	Hydrogeology

Second, both parts of the project, the technical assistance and the topical studies, are largely performed by the same personnel (with additional LBL staff participating in some of the topical studies). This ensures the participation of highly respected researchers working at the forefront of the state-of-the-art in providing DOE with comments and results relevant to the geotechnical aspects of nuclear waste geologic repositories. Often, technical reviews influence the direction and emphasis of topical studies, and topical studies provide inputs to the reviews.

The present report lists the technical reviews and comments made during the fiscal year 1989 and summarizes the technical progress of the topical studies.

In the area of technical assistance, there were numerous activities detailed in the next section. There were a total of 30 geotechnical support activities, including reviews of 15 Study Plans (SP) and participation in 5 SP Review Workshops; in-depth multidisciplinary review of 5 Exploratory Shaft Facility (ESF) Study Plans and presentation of results to DOE; preparation of a white paper and proposed work statement on preclosure monitoring and performance confirmation as on outgrowth of a request made by DOE to LBL, and its revision under draft QA procedures after a DOE preliminary review; the hosting of a DOE program review; with DOE's encouragement, preparation of 8 papers for the International High-Level Radioactive Waste Management Conference to be held in April, 1990 in Las Vegas, Nevada; and 5 instances of general technical assistance to DOE. These activities are described in a Table in the following section entitled "Geoscience Technical Support for Nuclear Waste Geologic Repositories."

During this fiscal year, LBL scientists also responded to DOE's request for consideration of the studies needed for preclosure monitoring and performance confirmation of a nuclear waste geologic repository in an unsaturated zone. This prompted several internal multidisciplinary discussions, where the critical parameters that should be monitored were reviewed and a number of monitoring methods based

on geophysics, geohydrology, and geochemistry were considered and assessed for their potential usefulness. These deliberations were summarized in a white paper and a proposed work plan entitled "Preclosure Monitoring and Performance Confirmation at Yucca Mountain: Applicability of Geophysical, Geohydrological, and Geochemical Methods." The proposed studies would demonstrate the usefulness of the suggested methods for observing system responses that can be most effectively utilized for preclosure monitoring and performance confirmation. They also would identify the methods most appropriate for use at different spatial and temporal scales of measurement. The white paper is attached as an Appendix of this report.

The subject of fracture studies forms the main part of the topical studies. The problem was approached from many directions:

Solid Mechanics,
Fluid Dynamics,
Geology,
Geophysics, and
Geochemistry.

The progress of our fracture studies is described in this report, with the article titles and authors listed in the Table of Contents. This multidisciplinary program included laboratory experiments and theoretical analyses as well as numerical simulations. Some of the studies are of a fundamental nature, which we expect will provide the basis for important practical geotechnical issues to be addressed, clarified or resolved in the near future. Other studies have already yielded results that provide new insights and analysis techniques for understanding the physics and chemistry of fractured repository rock systems at Yucca Mountain. A complete publication list of 40 reports from this project is presented at the end of this report. The major accomplishments over the past years of this project are summarized below.

LBL Studies of Fractured Rocks

Intact pieces of many rocks have extremely low values of fluid permeability and high (relative to, say, concrete) values of mechanical strength. If the properties of rock masses were the same as those of the intact rock there would be few, if any, questions concerning the effectiveness of nuclear waste isolation by deep geologic repositories. However, rock masses are heterogeneous structures comprising different compositions and textures separated and intersected by discontinuities on all scales; from microcracks through bedding planes, joints and fractures to faults. This heterogeneity significantly complicates the evaluation of transport of potentially contaminated groundwater away from a repository. Extensive discontinuities may allow significant quantities of groundwater to flow at much greater velocities than could occur in a porous rock medium. Therefore, the development of a successful geologic repository requires the ability to detect and characterize discontinuities and to evaluate fluid flow through them as a function of changes resulting from repository construction, waste emplacement, tectonic activity, and/or a different climate.

Recent interest in site characterization and performance assessment of rock masses for the design and construction of nuclear waste repositories provided the motivation for the LBL studies of the hydraulic, mechanical, geophysical, and geochemical properties of discontinuities. These studies are presented schematically in Figure 1, where the different focal points of these investigations are depicted and identified for reference. They are grouped into eight topics:

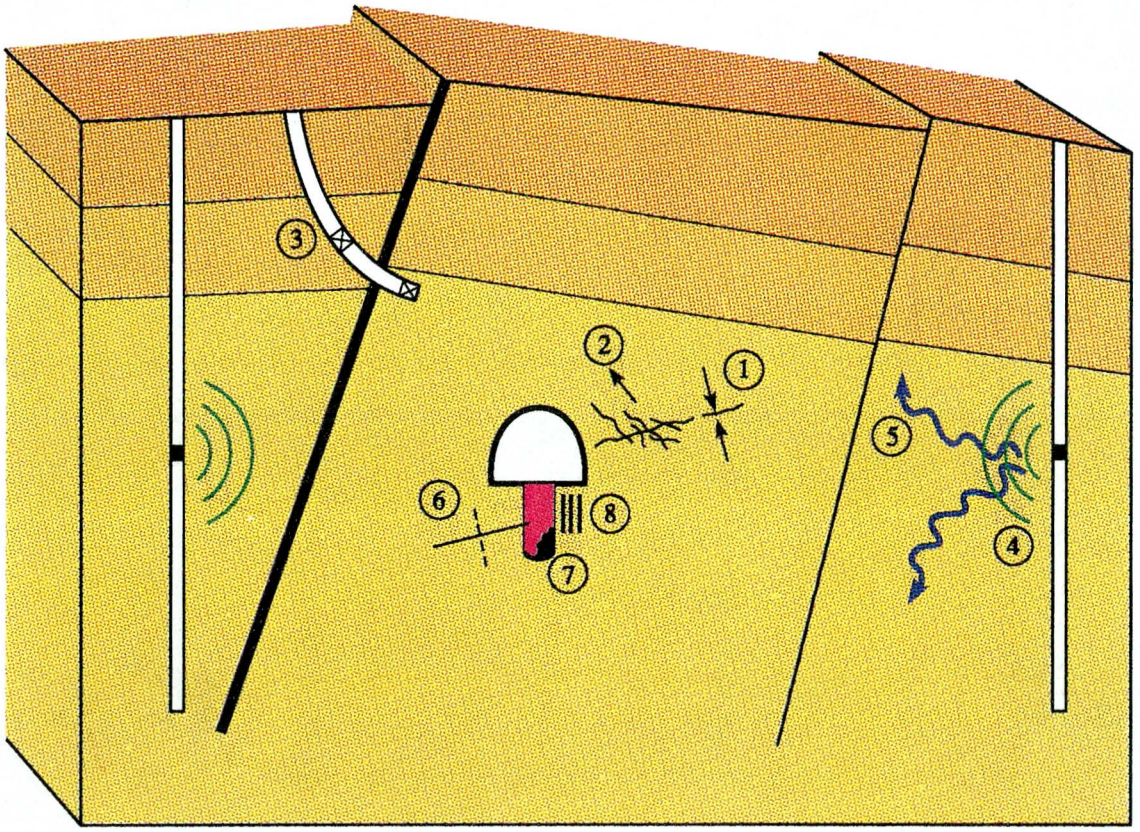

ESD-9011-0046

Figure 1

(1) Studies of the hydromechanical and geophysical properties of individual fractures.

(2) Studies of flow channeling in fractures.

(3) Development of hydrologic characterization methods for near-vertical faults and other potentially highly conductive features.

(4) Modeling studies associated with Vertical Seismic Profiling and other seismic techniques for characterizing fracture systems and fault zones.

(5) Modeling studies of electrical and electromagnetic geophysical techniques for the detection of fractures and their subsequent characterization using borehole data.

(6) Studies of the geochemical-hydrological regime of radionuclides in the material lining fractures.

(7) Studies of the effects of a varying thermal field on the precipitation of minerals and the possible reduction of mass diffusivity and fluid flow.

(8) Studies of canister borehole degradation under thermomechanical stress changes and the mechanical response of fractures to elevated temperatures.

correlation between the mechanical properties of a fracture, its hydraulic conductivity, and the amount of seismic attenuation it causes; (2) the phenomenon of flow channeling through preferred pathways in the fractures, which has important implications for radionuclide transport; (3) on a larger scale, the hydrologic characterization of near-vertical faults and other potentially highly conductive features with a view to analyzing the flow of water and air in an unsaturated fault-rock system; (4) also on a larger scale, the use of Vertical Seismic Profiling (VSP) and cross-hole seismic tomography to map elastic properties indicative of fracture density and structure, and to detect and characterize fractures and fault zones away from subsurface workings; (5) as a complement to seismic methods, studies of the use of electrical resistivity properties of the subsurface to detect the presence of fractures and their geometric orientation away from boreholes; (6) on a smaller scale near the waste canisters, investigations of the geochemical-hydrological interaction of radionuclides in the fluids with the material lining fractures in the rock; (7) also at this scale, numerical modeling studies to examine the effects of a varying thermal field on the precipitation of otherwise soluble minerals and the resulting decrease of porosity that could reduce the migration of solutes by diminishing mass diffusivity and fluid flow; (8) investigation of the mechanical degradation of the walls of the waste canister boreholes due to thermomechanical stress changes, and to understand the mechanical response of the fractured rock to elevated temperatures. The major findings in each of these areas are summarized briefly below.

Heterogeneous Flow in Fractures

Measurements of fluid flow through natural fractures in low permeability rocks have shown that, at low effective stresses, flow through a fracture diminishes much more rapidly with increasing stress than the cube of the apparent fracture aperture, but at high stresses it is asymptotic to a constant, stress-independent, irreducible flow

(Pyrak-Nolte *et al.*, 1987b). Important progress in understanding the real nature of the hydraulic and mechanical properties of natural fractures in low permeability rock has come from images of the fracture void space using Wood's metal porosimetry and a fractal construction for the correlated aperture distribution (Pyrak-Nolte *et al.*, 1988; Nolte *et al.*, 1989).

One result of the above studies showed that in a single fracture the void structure is a very heterogeneous two-dimensional system. This indicated that fluid flow through a fracture may be very non-uniform, and that the majority of the flow might be concentrated in a few preferred paths. A study of the heterogeneous nature of flow in a single fracture led to the concept of flow channeling to characterize mass transport in a system of realistic fractures having variable apertures. In the presence of flow channeling, the conventional methods of analyzing fluid flow and solute transport are generally not suitable since they have been formulated for relatively uniform flow in porous media.

Since it is impractical to obtain detailed data on fracture geometries in the field, our approach was to construct a conceptual model where the rock mass properties such as permeability to flow and dispersivity in tracer transport are correlated directly to a few basic geometric parameters. In our model these are the mean aperture value, its standard deviation, and the correlation length of the spatial distribution of fracture apertures. Because the heterogeneous nature of flow channeling implies that data from point measurements depend sensitively on the location of measurement, interpretation of data from a point measurement may not yield flow and transport parameters that are representative of the rock mass. We have used a statistical approach to analyze multiple-point measurements in order to calculate representative geometric parameters which characterize the flow and transport properties of the medium. Based on this framework we carried out a series of theoretical studies as well as applications to the analysis of field data.

The conceptual model of channeled flow and transport was first defined after a review of experimental evidence (Tsang and Tsang, 1987). Then the theoretical basis of the model was studied (Moreno *et al.*, 1988; Tsang and Tsang, 1989), and properties of the channel model were investigated (Tsang *et al.*, 1988). Implications of the model on experimental measurements of tracer transport in fractured rock will be explored and correlated with observations.

Hydrologic Characterization of Faults

The capability of characterizing near-vertical faults and other potentially highly conductive geologic features in the vicinity of a high-level waste repository is also of great importance. The existence of faults near a repository may provide a fast flow path from the disturbed zone to the accessible environment. Thus, part of our work was devoted to the development of mathematical solutions describing the hydrologic behavior of faults.

We studied the flow of water in a faulted multiple aquifer system and the flow of air in unsaturated faulted rock masses. These studies showed that if a permeable fault zone intercepts two horizontal aquifers, hydrologic characterization of the fault can be achieved by pumping water from one of the aquifers and monitoring drawdowns in nearby observation wells.

It has been proposed that the hydrologic properties of a fault crossing an unsaturated zone may be estimated by measuring subsurface air pressure changes. Analytical solutions were developed to calculate the pressure response of the faulted rock mass to atmospheric pressure variations (Javandel and Shan, 1990). Numerical methods were used to study multi-layered unsaturated systems like the Ghost Dance and Solitario Canyon faults at Yucca Mountain.

These studies suggest that when the fault permeability is at least an order of magnitude larger than that of the surrounding rocks, air pressure changes measured in

isolated intervals of a horizontal or inclined borehole drilled through the fault zone, could be used to estimate the fault/rock mass permeability ratio.

Seismic Properties of Fractured Rocks

One of the most crucial needs in the design and implementation of an underground waste isolation facility is a reliable method for the detection and characterization of fractures in zones away from boreholes or subsurface workings. Within underground workings we are able to examine fractures directly; however, a major problem exists in trying to extrapolate this information to unexposed regions. The techniques of Vertical Seismic Profiling (VSP) and cross-hole seismic imaging may be applicable to characterizing fractured media because of the anomalous behavior of fractures, faults, and joints relative to the propagation of seismic energy.

Previously, it was assumed that the ratio between the aperture of a fracture and seismic wavelengths was so small that individual fractures could not be located seismically. However, the combined effect of a number of fractures could be detected by seismic velocity anisotropy. A displacement- and velocity-discontinuity theory showed that single natural fractures do affect propagation of seismic waves at all wavelengths. The approach was extended by Pyrak-Nolte *et al.* (1987a) to investigate the effect of multiple fractures arranged in sets. The combined theoretical and laboratory results show that for such a system the expected variation in shear-wave velocity with propagation direction is significantly different from that expected for a conventional representation of a fractured rock mass as an anisotropic elastic medium. The displacement-discontinuity theory shows that a group time-delay and changes in seismic wave amplitude occur when a seismic wave encounters a fracture so that, in principle, the location and stiffness of fractures can be detected seismically even for a single fracture. Thus the techniques of VSP and crosshole tomography may be applicable in locating and characterizing fractures.

It is now necessary to relate the measured seismic properties to the overall hydrologic and geomechanical characteristics and predicted performance of the rock mass. There have been some attempts to relate geophysical anomalies to hydrologic or geomechanical parameters of geologic materials and to interpret the data for a better overall understanding of the rock properties, but there have been few reliable data sets available for such a study. Myer and others have been investigating whether a relationship exists between the mechanical stiffness of a fracture, its hydraulic conductivity, and the amount of seismic attenuation it causes. The relationships between the topography of fracture surfaces, mechanical stiffness, and hydraulic conductivity at different effective stresses have been examined using numerical models by Hopkins *et al.* (1987).

Modeling Seismic Wave Propagation through Fractured Rock Masses

Whereas several numerical techniques are available for predicting fluid flow through fracture networks, the corresponding computational tools for determining how a seismic wave is affected as it propagates through a network of arbitrarily located and oriented finite fractures was not available at the onset of this study. One-dimensional and two-dimensional ray tracing and synthetic seismogram models that originally relied on conventional welded boundary theory were modified to admit compliant fracture surfaces with arbitrary orientation by including the displacement-discontinuity boundary conditions in the solution for the propagation of the seismic wavelet. This allows us to vary fracture geometry, density and orientation in a medium and measure the seismic response. Parameter studies were carried out to determine the degree to which VSP is sensitive to interconnection, orientation, and other geometric properties of the fractures in the rock mass.

Due to the complex geometry of fractures and the complexity involved in ray tracing through many fractures, we soon realized that while the fracture displacement-

discontinuity approach greatly enhances our understanding of the mechanisms that affect the propagation of seismic energy, it is impracticable to model each individual fracture. Therefore, we maintained and improved our synthetic seismogram capability by integrating a more complete anisotropy theory into our numerical codes that trace rays through equivalent fractured media (Flueh *et al.*, 1989; Flueh and Okaya, 1989). Simultaneously, data from actual VSP field studies in crystalline, tuffaceous, and metamorphic fractured rocks were modeled to match the observed seismic wave behavior.

Electrical Methods to Characterize Fractured Rock Masses

Another aspect of our geophysical research was to investigate the relationship between the fluid saturation and the electrical conductivity of fractured rock masses. This relationship is needed to develop quantitative electrical and electromagnetic (em) imaging of fractures, fluid saturation, and to complement seismic imaging used in monitoring changes in the rock mass around the repository.

The electrical conductivity of rocks is controlled by pore fluids and their conductivity. Fluid saturation, in particular, has a dramatic effect on this parameter. As water is withdrawn from a saturated rock, the large pores and fractures desaturate first, but the bulk resistivity increases rather slowly since it is mainly controlled by the small interconnected water-filled pores and fractures. At this point the rock resistivity is roughly proportional to the inverse of saturation squared. As desaturation progresses, a critical saturation is reached at which point there is no longer any water to conduct along some pores and fractures. This breaking of the conduction paths leads to a much more rapid increase in resistivity, roughly proportional to the inverse of saturation to the fourth power. The critical saturation depends on the rock type (the nature of the porosity) and may also depend strongly on the fracture network pattern.

So far, our studies have emphasized the dc resistivity method, where current is injected through electrode pairs and the resulting voltage drops are measured in the vicinity with other pairs of electrodes. The measured voltage drops are then used to infer the distribution of electrical resistivity. Using a difference scheme in the dc method, a two-dimensional modeling study was carried out to simulate repository environments (Asch and Morrison, 1989). It was shown that resistivity measurements, using electrodes in boreholes located well away from the repository and on the surface, are sensitive to resistivity changes in the repository that could not be practically observed from surface measurements alone.

Another important practical problem addressed was the detection of any major fracture zone near, but not intersected by, boreholes. However, these boreholes still allow the use of subsurface em techniques to detect and characterize these nearby fractures. Using the integral equation modeling technique, A diffusion tomography technique was also developed (Zhou, 1989) for analyzing crosshole audio-frequency em data which is similar to diffraction tomography in seismic applications. Studies using synthetic two-dimensional models showed that this approach is very promising for detecting individual fractures and their dips in the region between boreholes. Other calculations indicated that two fractures could be resolved when the separation is as close as about one-tenth of the wave length. This is the first quantitative assessment of the resolution of fracture networks with em methods.

Radionuclide Transport in Fractured Rock Masses

The local geochemical-hydrological regime will be affected by high temperatures over long periods of time in the near field of a nuclear waste canister. These hydrogeochemical processes must be understood if the transport of radionuclides away from a breached canister is to be modeled and predicted. The objectives of these investigations were to develop an understanding of the interaction, under long exposure to

elevated temperatures, of radionuclides in the fluids with the materials lining the fractures in the rock, and to understand the mechanical response of the fractured rock to the elevated temperatures. To accomplish this, samples of core from holes that penetrated high-temperature hydrothermal zones and holes cored through heater-test zones were examined petrologically, geochemically, and geomechanically.

Initial emphasis was on core samples of quartz monzonite, obtained from rock previously subjected to a year-long heater experiment simulating high-level radioactive waste, conducted at Stripa, Sweden (Wollenberg and Flexser, 1986). Results indicated localized mobilization and deposition of uranium in an open fracture in the heated rock, and that differences in compressional- and shear-wave parameters between heated and less-heated rock can be attributed to differences in the density of microcracks.

As interest in tuff as a repository medium became apparent, we examined core from holes penetrating fractured hydrothermal systems in rhyolitic tuff of the Long Valley and Valles calderas, and are investigating heated and unheated, unsaturated tuff from experiments at G-tunnel, Nevada Test Site. The Long Valley and Valles studies indicate the localized mobilization of uranium and its daughter elements associated with iron-rich minerals in tuff and with carbonaceous minerals in underlying sedimentary rocks, at temperatures comparable to those expected in a repository environment. Investigations of welded tuff in cores from the G-tunnel heater experiment show that U is concentrated 4 to 10 times above whole-rock values in Fe-Ti-Mn-oxide minerals, with an apparent depletion in U observed in these minerals over the 10 cm of tuff adjacent to the heater. Observations to date suggest that U is mobile in hydrothermal systems, but that localized reducing environments provided by Fe-rich minerals and/or carbonaceous material concentrate U and thus attenuate its migration.

An aspect of geochemical behavior that can have important consequences in performance assessment is the effect of a variable thermal field on (1) the movement of major solution components and dissolved waste radionuclides, and (2) the stabilities of

minerals exposed to the changing thermohydrochemical environment. Variable thermal fields can arise in the near vicinity of nuclear waste canisters and from mixing of fluids having different temperatures. Such fields imposed on previously stable or metastable fracture minerals can induce dissolution of existing minerals, transport of dissolved chemical species, and precipitation of new solid phases. Redistribution of materials within fractures by chemical reactions and transport can produce changes of physical properties of the rock mass such as porosity, mass diffusivity, and permeability. Changes of these parameters can affect transport of both radionuclides and major components of subsurface fluids. In particular, precipitation of minerals at or near the fracture-matrix boundary can reduce diffusive transport of radionuclides into the matrix, thus decreasing the effective retardation of the radionuclides. On the other hand, alteration of some mineral species may enhance their ability to retard radionuclides.

Modeling studies have been performed to see whether a varying thermal field could induce precipitation of otherwise unstable (soluble) minerals, and that the resulting decrease of porosity could reduce migration of solutes by decreasing mass diffusion and fluid flow. The extent to which these mechanisms are effective in particular settings depends on the magnitudes of temperature changes, compositions and solubilities of existing minerals, and composition of the fluid phase.

Mechanical Degradation in Rock

Heat flow and solute transport near the waste canisters may also be affected by mechanical degradation of the walls of boreholes within which the canisters will be placed. This could adversely affect heat transfer, impose mechanical loads on waste canisters, and provide paths for groundwater flow to and from the canisters. A series of laboratory experiments on borehole breakout using Wood's metal porosimetry has shown how this phenomenon occurs by the subcritical growth of extensile cracks

driven by the tangential compressive stress around the hole, (Ewy *et al.*, 1988). One conclusion appears to be that time-dependent borehole degradation is likely to occur, but that it can be avoided easily by lowering rock temperatures or by installing appropriate borehole liners.

Summary

These brief summaries of the LBL fracture studies show that significant advances have been made in our understanding of basic phenomena and material properties affecting the hydrologic, mechanical, geophysical, and geochemical characteristics of fractured rock masses. Along with this increased understanding, new techniques were developed for detecting and characterizing fractures and fault zones in the subsurface, predicting the response of fractures to hydraulic, mechanical, and thermal stresses, and evaluating the main processes that control fluid flow and solute transport in fractured rock masses. This improved understanding and the analytical and practical methods developed in the past four years constitute part of LBL's contribution to the present state-of-the-art in site characterization and performance assessment of rock masses that will be needed in the design and construction of nuclear waste repositories.

Geoscience Technical Support for Nuclear Waste Geologic Repositories

D. C. Mangold and C. F. Tsang

The Geoscience Technical Support activities in the Geologic Repository Project (GRP) at LBL covered a range of reports and reviews in FY89, particularly reviews of Study Plans of the Yucca Mountain site and their associated Comment Resolution Workshops. In addition, in consultation with DOE/HQ, we investigated and presented DOE with well-considered scientific inputs to program directions and new areas of needed work. This included the development of a white paper and proposed work plan on prelcosure monitoring and performance confirmation that grew out of a request made by DOE to LBL to consider such studies for a repository in the unsaturated zone. The accompanying table, "Geotechnical Support Activities: Fiscal Year 1989," gives the type of technical review or other activities, the date when a report was sent to DOE, and a brief description of the material reviewed or meeting attended. This year also saw the beginning of a quality assurance (QA) program for GRP. The accompanying table, "Quality Assurance Activities: Fiscal Year 1989," gives a brief chronology of the GRP QA plan development.

The reviews of Study Plans were performed by a pool of highly knowledgeable and respected research scientists, who represent a broad range of disciplines in the earth sciences. The individuals and their specialities are listed in the table below. The diversity of backgrounds of the participating scientists is representative of the multidisciplinary teamwork that has characterized LBL's effort in this project. They have developed a close working relationship through frequent internal LBL discussion

meetings and through cooperative topical studies (reported in subsequent parts of this report) and based on this, they are able to perform the many different technical support tasks given by DOE in a timely and effective manner.

Name	*Principal Expertise*
Chalon L. Carnahan	Geochemistry
Steven Flexser	Geology
Harold A. Wollenberg	Geology
Neville G. W. Cook	Geomechanics
Larry R. Myer	Geomechanics
Ki Ha Lee	Geophysics
Ernest L. Majer	Geophysics
Thomas V. McEvilly	Geophysics
H. Frank Morrison	Geophysics
Iraj Javandel	Hydrogeology
Marcelo J. Lippmann	Hydrogeology
Chin-Fu Tsang	Hydrogeology

In total, there were 30 geotechnical support activities, including reviews of 15 Study Plans (SP) and participation in 5 SP Review Workshops; in-depth multidisciplinary review of 5 Exploratory Shaft Facility (ESF) Study Plans and presentation of results to DOE; preparation of a white paper and proposed work statement on preclosure monitoring and performance confirmation as on outgrowth of a request made by DOE to LBL, and its revision under draft QA procedures after a DOE preliminary review; the hosting of a DOE program review; with DOE's encouragement, preparation of 8 papers for the International High-Level Radioactive Waste Management Conference to be held in April, 1990 in Las Vegas, Nevada; and 5 instances of general

technical assistance to DOE. Each activity is described in the accompanying table at the end of this section. A brief summary of the activities is given below.

Study Plan Reviews

The Study Plans of the Yucca Mountain Project site were reviewed by LBL scientists in the areas of geology, geomechanics, geophysics, hydrology, and geochemistry. In general, reviews were done by a few specialists in each area in order to cover the technical aspects in each Study Plan. The comments on the technical aspects of these Study Plans were also provided to DOE in a timely way.

Those who performed the technical review were also participants in the rest of the review process. They held overall review discussions at LBL on the Study Plans to achieve a multidisciplinary overview and understanding of each one. After these discussions, many of the same scientists who reviewed a given section of a Study Plan also attended the SP Comment Resolution Workshops where all comments on that portion were considered. There they worked with the authors and DOE review leaders to suggest changes or revisions to improve the technical content of the text, particularly by helping to clarify technical points in the documents. Also, they later dealt with the dispositions of their comments by others so that a well-balanced review would be achieved.

DOE Program Review

In February, LBL hosted a program review of the GRP project at DOE's request. LBL scientists gave presentations of their research work at this time on laboratory studies of fracture properties and behavior, the channel model of fracture flow, multiphase flow in fractured media, and geophysical detection of fractures. A copy of the viewgraphs from the presentations was sent to DOE.

Review of Exploratory Shaft Facility Study Plans

At the request of DOE, LBL was sent 5 ESF Study Plans for a detailed preliminary technical review during April and May:

Technical Review of ESF Study Plans

S.P. Number	Title
8.3.1.2.2.2	Water Movement Tests
8.3.1.2.2.4	Characterization of the Yucca Mountain Unsaturated Zone Percolation Exploratory Shaft Facility Study
8.3.1.4.2.2	Characterization of Structural Features in the Site Area
8.3.1.15.1.5	Excavation Investigations
8.3.1.15.2.5	Characterization of the Site Ambient Stress Conditions

Ten scientists participated by individually reading the detailed content of the Study Plans in their area of expertise and then meeting together 14 times with intensive interdisciplinary discussions. The results from the review and discussions were summarized for each Study Plan. Then DOE/HQ personnel came to LBL for 1½ days, May 31–June 1, to hear presentations by the reviewers and to receive the summaries of LBL's discussions concerning the Study Plans.

Other Technical Assistance Related to the Exploratory Shaft Facility

One LBL investigator was invited to join the Exploratory Shaft Test Plan Committee (ESTF). He regularly attended committee meetings and kept the other GRP project members abreast of the latest developments in the plans for ESF experiments.

In September, we held an interdisciplinary discussion concerning key investigations that would need to be done between now and the start of the Exploratory Shaft Facility. A letter was sent to DOE with a suggestion that there was an urgent need for

a scientific steering committee for the work to be done at the G-Tunnel Test Facility to coordinate and focus all the G-Tunnel experiments in a scientifically integrated way in order to provide useful inputs to the ESF experiments later. However, the letter has become outdated because of the closure of G-Tunnel.

White Paper and Proposed Work Statement for Preclosure Monitoring and Performance Confirmation at Yucca Mountain

During this fiscal year, LBL scientists also responded to DOE's request for consideration of the studies needed for preclosure monitoring and performance confirmation of a nuclear waste geologic repository in an unsaturated zone. This prompted several internal multidisciplinary discussions, where the critical parameters that should be monitored were reviewed and two scales of measurement relevant to monitoring activities, room scale and repository scale, were found useful as a framework for investigation. A number of monitoring methods based on geophysics, geohydrology, and geochemistry were considered and assessed for their potential usefulness. Particular emphasis was given to measurement of the spatial distribution of parameters in contrast to single-point measurements.

These deliberations were summarized in a white paper and a proposed work plan entitled "Preclosure Monitoring and Performance Confirmation at Yucca Mountain: Applicability of Geophysical, Geohydrological, and Geochemical Methods." The proposed studies would demonstrate the usefulness of the suggested methods for observing system responses that can be most effectively utilized for preclosure monitoring and performance confirmation. They also would identify the methods most appropriate for use at each spatial and temporal scale of measurement.

Copies of both documents were first sent to DOE for review in January, 1989. LBL answered a query and took account of DOE suggestions to produce revised versions that were sent to DOE in May. Also, a draft project QA plan was developed

(see below) which included procedures for handling documents produced by the project. After concurrence by DOE/HQ, the white paper was sent in September to an external reviewer for comments. A copy of the white paper is included as an appendix to this report.

Other Technical Assistance to DOE

In February, at USGS request, a set of all GRP project publications was sent to the USGS Nuclear Hydrology Program office in Denver, Colorado. We hope that these will contribute useful inputs to their program within the Yucca Mountain Project.

In March, a report of research from Task 7 of this project, Coupling of Precipitation/Dissolution Reactions to Mass Diffusion, was sent to DOE. It had potential application to five or more of the site characterization activities.

With DOE's encouragement, in September LBL scientists submitted 7 abstracts on their topical studies supported by this project to the International High-Level Radioactive Waste Management Conference to be held April 8–12, 1990 in Las Vegas, NV and sent copies to DOE on September 22. In addition, we also prepared one invited paper entitled "Dynamic Use of Geoscience Information to Develop Scientific Understanding for a Nuclear Waste Repository" by N. G. W. Cook and C. F. Tsang.

QA Plan Development

As DOE/OCRWM began its QA program, the GRP project initiated its own project QA plan to conform to the DOE/OCRWM standards for QA Level 1. A chronology of its development is presented in the accompanying table.

On March, 16, 1989, LBL received controlled copies of the Quality Assurance Requirements (QAR) and Quality Assurance Program Description (QAPD) documents from DOE/HQ. LBL began internal discussions on March 24 of how to apply the QA requirements from the QAR and QAPD to have a QA program for this project. In

April, LBL received from DOE/OCRWM controlled copies of the Quality Assurance Manual (QAM) and Quality Assurance Administrative Procedures (QAAP) documents. A new staff member who had experience in implementing other QA programs at LBL was added to the project at the beginning of May in order to start writing the GRP project QA Plan. He incorporated relevant materials from the QAR, QAPD, QAM, and QAAP documents into the plan. A preliminary draft QA procedure was completed for handling documents produced by the project by the end of May.

During the period of May through September, LBL continued to receive DOE/OCRWM controlled copies of QAAP procedures and other QA materials including the Implementing Line Procedure (ILP) Manual and ILP 22.1.3, DOE/HQ Review of Study Plans. The relevant materials from these documents were incorporated into the project QA plan.

As mentioned above, after consultation with DOE/HQ, the LBL white paper and proposed work statement entitled "Preclosure Monitoring and Performance Confirmation at Yucca Mountain: Applicability of Geophysical, Geohydrological, and Geochemical Methods" were sent to an external reviewer under the draft preliminary project QA procedures, including a Reviewer Qualification Verification Statement and Review Comment Sheets.

By the end of the fiscal year in September, a preliminary draft QA plan was in final stages of preparation for all areas of project activity and was undergoing internal review. Also, steps were being taken to have a permanent staff member to handle all QA-related matters for the project. The draft QA plan was later sent on December 6 to DOE/HQ for review and comments.

Conclusion

LBL sought to be responsive and active in meeting DOE's need for geoscience technical support for nuclear waste repositories. The ability of LBL scientists from

many disciplines to work together was an important part of the effort to provide DOE with timely, helpful, and balanced technical comments to meet its on-going responsibilities. In consultation with DOE, from time to time we also developed and provided well-considered scientific inputs to program directions and new areas that need attention.

GEOTECHNICAL SUPPORT ACTIVITIES

FISCAL YEAR 1989

Activity	Delivery	Description
SP Review	11/11/88	Study Plan 8.3.1.5.2.1, Quaternary Regional Hydrology
SP Review	11/22/88	Study Plan 8.3.1.2.2.3, Characterization of Yucca Mountain Unsaturated Zone Percolation: Surface-Based Studies
SP Review	12/6/88	Study Plan 8.3.1.2.2.4, Characterization of Yucca Mountain Unsaturated Zone Percolation—ESF Study
SP Review	1/9/89	Study Plan 8.3.1.17.4.2, Location and Recency of Faulting Near Prospective Surface Facilities
SP Review Workshop	1/18–19/89	Comment Resolution Workshop for Study Plan 8.3.1.17.4.2, Location and Recency of Faulting Near Prospective Surface Facilities held in Albuquerque, NM
SP Review	1/30/89	Study Plan 8.3.1.17.4.6, Quaternary Faulting Within the Site Area
White Paper and Proposed Work Statement	1/30/89	White Paper and Proposed Work Statement on Preclosure Monitoring and Performance Confirmation at Yucca Mountain: Applicability of Geophysical, Geohydrological, and Geochemical Methods, sent to DOE from LBL, an outgrowth of a request made by DOE to LBL to consider studies which would be required for preclosure monitoring and performance confirmation of a repository in the unsaturated zone
SP Review Workshop	2/1–3/89	Comment Resolution Workshop for Study Plan 8.3.1.2.2.3, Characterization of Yucca Mountain Unsaturated Zone Percolation: Surface-Based Studies held Denver, CO
SP Review	1/2/89	Study Plan 8.3.1.3.2.2, History of Mineralogic and Geochemical Alteration of Yucca Mountain
Hosted DOE Program Review	2/16–17/89	At DOE's request, LBL hosted a two-day program review of the GRP project; copies of the viewgraphs of the review presentations were given to DOE along with copies of all publications from the beginning of the project to the present and the draft annual report

GEOTECHNICAL SUPPORT ACTIVITIES

FISCAL YEAR 1989 (Continued)

Activity	Delivery	Description
Technical Assistance	2/22/89	A letter was sent to DOE to answer a query on the white paper mentioned above by showing that LBL's choice of critical parameters included those of a previous major study
Technical Assistance	2/27/89	A copy of all GRP project publications was sent to the USGS Nuclear Hydrology Program office in Denver, CO at USGS request
Technical Assistance	3/14/89	A topical research report for Task 7, Coupling of Precipitation/Dissolution Reactions to Mass Diffusion, was sent to DOE
SP Review	3/28/89	Study Plan 8.3.1.15.1.2, Laboratory Thermal Expansion Testing
SP Review Workshop	4/12–13/89	Comment Resolution Workshop for Study Plan 8.3.1.17.4.6, Quaternary Faulting Within the Site Area held at DOE/HQ in Washington, DC
White Paper and Proposed Work Statement	5/31/89	Revised versions of the LBL White Paper and Proposed Work Statement on Preclosure Monitoring and Performance Confirmation at Yucca Mountain: Applicability of Geophysical, Geohydrological, and Geochemical Methods, were sent to DOE
Review of 5 Exploratory Shaft Facility Study Plans	5/31–6/1/89	At DOE's request, LBL reviewed 5 Exploratory Shaft Facility Study Plans in depth during April and May: SP 8.3.1.2.2.2 Water Movement Tests SP 8.3.1.2.2.4 Unsaturated Zone Percolation SP 8.3.1.4.2.2 Structural Features SP 8.3.1.15.1.5 Excavation Investigations SP 8.3.1.15.2.5 Site Ambient Stress 10 scientists participated by individually reading the detailed content of the Study Plans in their area of expertise and then meeting together 14 times with strong interdisciplinary discussions; DOE/HQ personnel were invited to come to LBL for 1½ days, May 31–June 1, to hear presentations of the results from this review, and to receive a summary LBL's discussions for each Study Plan

GEOTECHNICAL SUPPORT ACTIVITIES

FISCAL YEAR 1989 (Continued)

Activity	Delivery	Description
SP Review Workshop	5/31–6/1/89	Comment Resolution Workshop for Study Plan 8.3.1.3.2.2, History of Mineralogic and Geochemical Alteration of Yucca Mountain held at LANL, NM
SP Review Workshop	7/31–8/2/89	Comment Resolution Workshop for Study Plan 8.3.1.15.1.2, Laboratory Thermal Expansion Testing held at DOE/HQ in Washington, DC
Technical Assistance	8/26/89	At DOE's suggestion, LBL held a series of four inter-disciplinary discussions concerning a dynamic decision process for site characterization, and a letter and chart summarizing the outcome were sent to DOE
SP Review	8/29/89	Study Plan 8.3.1.2.1.2, Characterization of the Yucca Mountain Regional Surface-Water Runoff and Streamflow
SP Review	8/29/89	Study Plan 8.3.1.2.1.2, Characterization of the Site Saturated-Zone Ground-Water Flow System
SP Review	8/29/89	Study Plan 8.3.1.15.1.1, Laboratory Thermal Properties
SP Review	8/29/89	Study Plan 8.3.1.16.1.1, Characterization of Flood Potential and Debris Hazards of the Yucca Mountain Site
Papers for IHLRWM Conference	9/6/89	With DOE's encouragement, LBL scientists submitted 7 abstracts on their topical studies supported by this project to the International High-Level Radioactive Waste Management Conference to be held April 8–12, 1990 in Las Vegas, NV and sent copies to DOE on September 22; in addition, there was one invited paper from this project
SP Review	9/12/89	Study Plan 8.3.1.3.3.2 & 3.3, Kinetics and Thermo-dynamics of Mineral Evolution and Conceptual Model of Mineral Evolution
SP Review	9/21/89	Study Plan 8.3.1.2.2.5, Diffusion Test in the Explora-tory Shaft
SP Review	9/21/89	Study Plan 8.3.1.3.7.1, Retardation Sensitivity Analysis

GEOTECHNICAL SUPPORT ACTIVITIES

FISCAL YEAR 1989 (Continued)

Activity	Delivery	Description
SP Review	9/28/89	Study Plan 8.3.1.2.2.6, Characterization of the Yucca Mountain Unsaturated-Zone Gaseous Phase Movement
Technical Assistance	9/29/89	LBL held an interdisciplinary discussion concerning key investigations that would need to be done between now and the start of the Exploratory Shaft Facility (ESF), and a letter was sent to DOE with a suggestion for a scientific steering committee for the work to be done at the G-Tunnel Test Facility to coordinate and focus all the G-Tunnel experiments in a scientifically integrated way in order to prepare for the ESF experiments later

QUALITY ASSURANCE ACTIVITIES

FISCAL YEAR 1989

Activity	Delivery	Description
DOE QA Document Transmittal	3/16/89	LBL received from DOE/OCRWM copies of the Quality Assurance Requirements (QAR) and Quality Assurance Program Description (QAPD) documents
QA Plan Development	3/24/89	LBL began internal discussions of how to apply the QA requirements from the QAR and QAPD to have a QA Level 1 program for this project
DOE QA Document Transmittal	4/21/89	LBL received from DOE/OCRWM Controlled Copy No. 324 of the Quality Assurance Manual (QAM) and Quality Assurance Administrative Procedures (QAAP) documents
QA Plan Development	5/1/89	In May a new staff member who had experience in implementing other QA programs at LBL was added to the project in order to begin the writing of the GRP project QA Plan, incorporating the relevant materials from the QAM and QAAP documents
DOE QA Document Transmittal	5/89–9/89	During the period of May through September, LBL continued to receive DOE/OCRWM controlled copies of QAAP procedures and other QA materials; these were inserted into the manuals as required and the signed acknowledgements for the receipts were sent back to DOE in a timely manner
QA Plan Development	5/26/89	A preliminary draft QA plan was completed for handling documents produced by the project
DOE QA Document Transmittal	8/8/89	DOE/OCRWM sent to LBL a controlled copy of the Implementing Line Procedure (ILP) Manual and ILP 22.1.3, DOE/HQ Review of Study Plans, and relevant materials from these documents were incorporated into the project QA plan

QUALITY ASSURANCE ACTIVITIES

FISCAL YEAR 1989 (Continued)

Activity	Delivery	Description
Review of White Paper and Proposed Work Statement by Preliminary QA Procedures	9/12/89	After concurrence by DOE/HQ, the LBL White Paper and Proposed Work Statement on Preclosure Monitoring and Performance Confirmation at Yucca Mountain: Applicability of Geophysical, Geohydrological, and Geochemical Methods, was sent to an external reviewer under the draft preliminary project QA procedures, including a Reviewer Qualification Verification Statement and Review Comment Sheets
QA Plan Development	9/89	A preliminary draft QA plan was in final stages of preparation for all areas of project activity and was undergoing internal review; also, plans were being made to have a permanent staff member to handle all QA-related matters for the project

Radionuclides in Hydrothermal Systems as Indicators of Repository Conditions

H.A. Wollenberg, S. Flexser, and A.R. Smith

Abstract

Hydrothermal systems in tuffaceous and older sedimentary rocks contain evidence of the interaction of radionuclides in fluids with rock matrix minerals and with materials lining fractures, in settings somewhat analogous to the candidate repository site at Yucca Mountain, NV. Earlier studies encompassed the occurrences of U and Th in a "fossil" hydrothermal system in tuffaceous rock of the San Juan Mountains volcanic field, CO. More recent and ongoing studies examine active hydrothermal systems in calderas at Long Valley, CA and Valles, NM. At the Nevada Test Site, occurrences of U and Th in fractured and unfractured rhyolitic tuff that was heated to simulate the introduction of radioactive waste are also under investigation. Observations to date suggest that U is mobile in hydrothermal systems, but that localized reducing environments provided by Fe-rich minerals and/or carbonaceous material concentrate U and thus attenuate its migration.

Introduction

Hydro-geochemical processes must be understood if the movement of radionuclides away from a breached radioactive waste canister is to be modeled and predicted. Hydrothermal systems in tuffaceous and underlying sedimentary rocks contain evidence of the interaction of radionuclides in fluids with materials lining fractures, in settings that are somewhat analogous to the candidate repository site at Yucca Mountain, NV. Earlier studies [1,2] encompassed the occurrences of U and Th in a "fossil" hydrothermal system in tuffaceous andesitic rock of the San Juan Mountains volcanic field, CO. At this site,where a regional hydrothermal system occurred in response to intrusion of monzonite into andesitic tuff, U and Th were confined to accessory minerals, and thus were essentially unaffected by hydrothermal alteration or by intense heating at the monzonite-tuff contact. More recent and ongoing studies examine active hydrothermal systems at the Long Valley caldera, CA and the Valles caldera, NM. The occurrences of U and Th in fractured and unfractured rhyolitic tuff that was heated to simulate the introduction of radioactive waste are also under investigation. In these studies high-resolution gamma spectrometry and

fission-track radiography are coupled with observations of alteration mineralogy, stable-isotope ratio measurements, and thermal profiles to deduce the evidence of, or potential for movement of U and Th in response to the thermal regimes.

Long Valley Caldera

Samples of core were examined from a 730 m-deep hole in rhyolitic tuff of the active hydrothermal system of the Long Valley caldera [3]. The hole penetrates a thermal regime from near ambient temperature to over 200°C (Fig.1,2). Evidence of disequilibrium in the U decay series was observed in calcite-cemented breccia of a fracture zone at ~150°C, in a region of rapidly increasing temperature with depth where oxygen isotope ratios concomitantly decrease from +3 to -2. Illite is the principal clay mineral in this zone[4]. Fission-track radiography shows that U associated with Fe-rich mineral phases in the breccia is concentrated to 30 to 50 ppm, compared to 11 to 13 ppm in the calcite and ~6 ppm in unbrecciated tuff. Thorium in the high-U zone is also somewhat elevated, ~24 ppm, compared to a local background of ~20 ppm. The U/Th ratio in this zone, ~1, is anomalously high, compared to ~0.3 in the rest of the core. High-resolution gamma spectrometry indicates that the U in the breccia zone is not in secular equilibrium with its daughter elements, (in some cases Ra is in excess with respect to U , in others U daughters appear depleted), suggesting localized mobilization/deposition of parent U and/or its daughters in the hydrothermal environment.

Valles Caldera

In quartz-rich welded rhyolitic tuff of the Valles caldera, a ~530 m-deep core hole intersected the vapor zone (at temperatures ~100° C) that caps the active fluid-saturated hydrothermal system [5]. Relatively high concentrations of U (9 to 16 ppm) are observed in this zone (Fig. 3); they are nearly equal to Th concentrations [6]. The high-U zone also contains relatively high concentrations of Mo (in the form of poorly crystalline molybdenite), suggesting that it was deposited in an earlier saturated regime at ~200°C [7]. The presence of an earlier saturated regime is substantiated by the decrease in whole-rock oxygen isotope ratios over the upper ~ 100 m of the hole (Fig. 3). Gamma-spectrometric evidence of equilibrium in the U-decay series in these high-U samples suggests that there has been little if any mobility of U over the life of the vapor-dominated system. In the underlying saturated zone where temperature rapidly increases with depth (Fig. 3), U

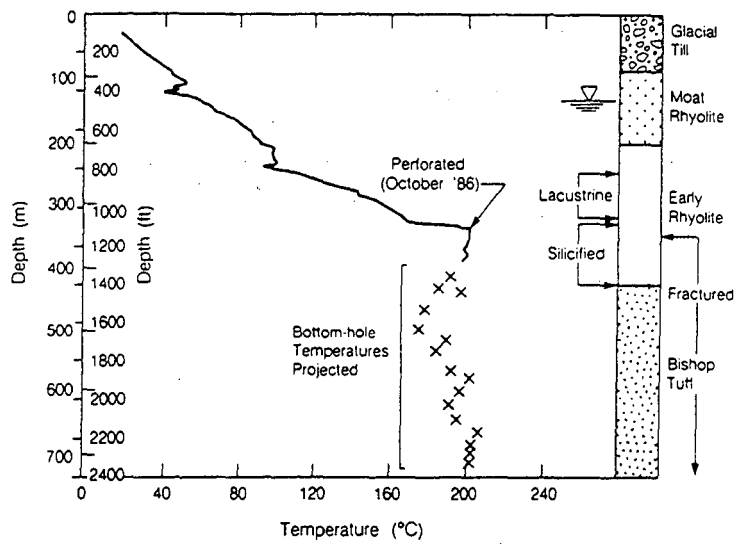

1. Thermal and lithologic diagram of a hole cored in tuff of the Long Valley caldera. Projected temperatures are from bottom-hole measurements made during coring (from [3]).

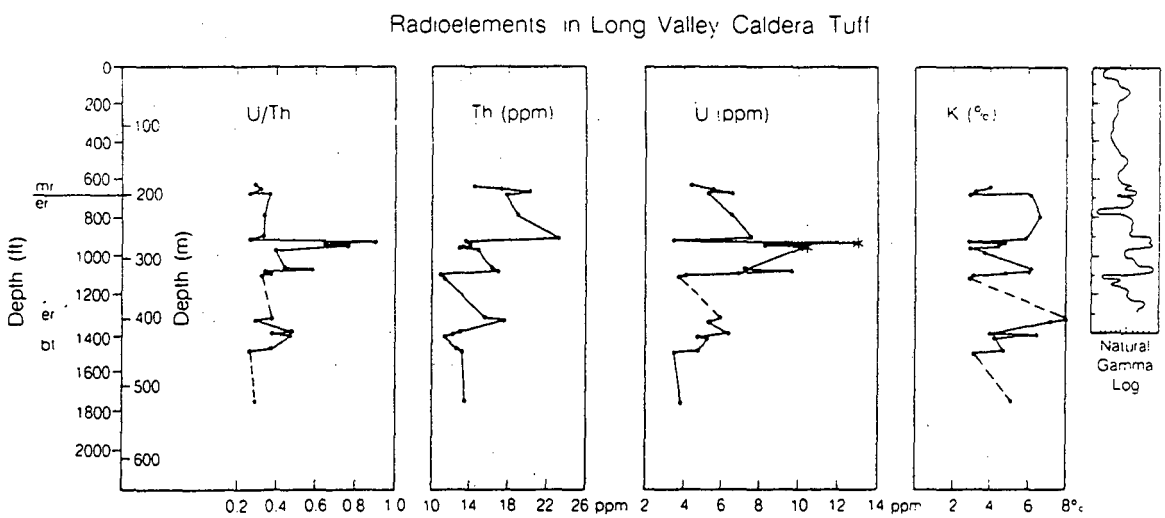

2. Distribution of radioelements over a temperature range 60 to 150°C in the Long Valley core hole. Asterisks in the U diagram indicate U-series disequilibrium. mr = Moat Rhyolite, er = Early Rhyolite, bt = Bishop Tuff.

concentrations drop to 6 to 8 ppm, while Th continues to rise with depth. However, in the saturated zone the pattern of U distribution generally follows that of Th. Fission-track radiography is underway to determine the mineral asociations of U in the tuff of the vapor-dominated and saturated zones, and will help explain the cause of the enrichment of U at depths below ~ 150 m.

In the outflow zone of the caldera's hydrothermal system [8] Ra in anomalously high concentrations occurs at sites in the Paleozoic calcareous Abo shale (80° C) that underlies the Quaternary volcanic rocks. At these sites, Ra is unsupported by parent U, suggesting preferential removal of U or addition of Ra by hydrothermal fluids [9]. Uranium concentrations of several tenths of a percent are associated with carbonaceous material in the underlying Madera limestone (at ~120° C).

The Valles and Long Valley studies thus provide evidence for at least localized mobility of U and its daughters in tuff and underlying sedimentary rocks, at temperatures comparable to those expected in a repository environment.

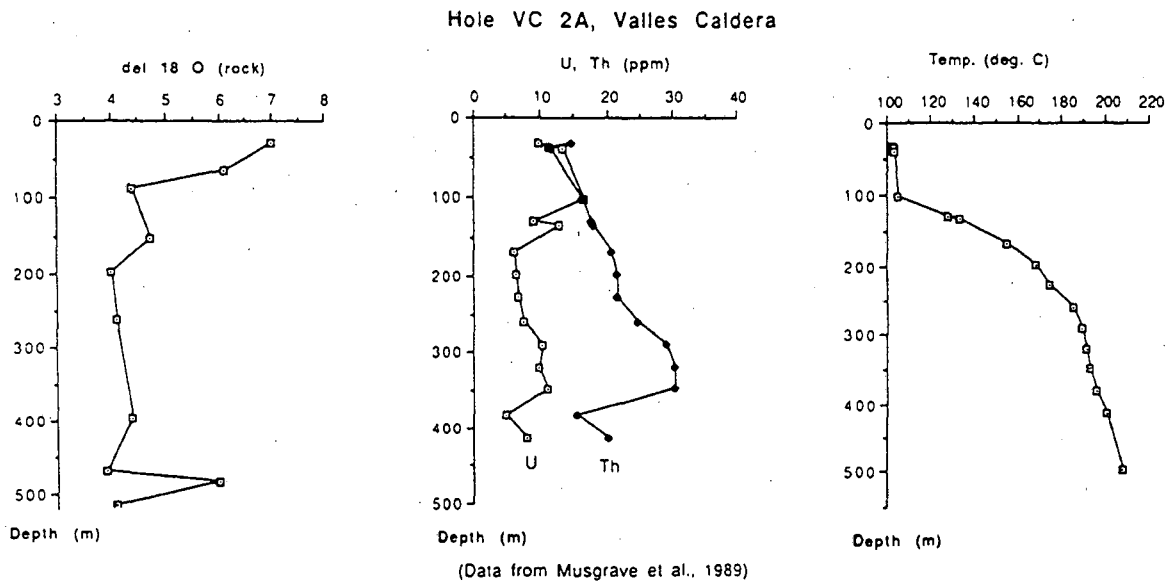

3. Radioelement, temperature, and O-isotope diagrams for hole VC-2A, in rhyolitic tuff of the Valles caldera (data from [6]).

Nevada Test Site

At the G-tunnel test facility, Nevada Test Site, core has been obtained for mineralogical, geochemical and geomechanical studies of welded tuff from the unsaturated zone that has been artificially heated to repository temperature. The mineralogical and physical properties of this tuff, the Grouse Canyon, are similar to those of the densely welded Topopah Springs tuff, the candidate repository medium [10]. In an experiment conducted by Lawrence Livermore National Laboratory (LLNL), an electric heater simulated the localized thermal field caused by introduction of high-level waste [11]. The heater was at full power for 4 months, with a temperature of 240° C at the heater edge and 120° C in rock at a distance of 0.7m. A small steam-dominated system developed in the rock within 0.6-0.7m of the heater and lasted for at least 70 days.

To provide baseline data, we selected unheated core from a hole, designated NE-2, that passes within 1 m of the electric heater (Fig. 4). The distribution of radioelements in this core was investigated by gamma spectrometry, and results showed a relatively even distribution of U and Th over the length of the core (mean values: U=3.4 +/- 0.4 ppm, Th= 15.6 +/- 2.1 ppm). More detailed gamma spectrometry indicated high concentrations of U and Th associated with an open fracture, coated partially with amorphous silica. This occurrence was examined by fission-track radiography, disclosing that U, at ~20 ppm, is concentrated by a factor of 5 in the silica coating relative to the tuff matrix. This U-rich coating could have been associated with the hydrothermal system that developed soon after deposition of the tuff, or with a cooler, fracture-controlled groundwater system that subsequently developed.

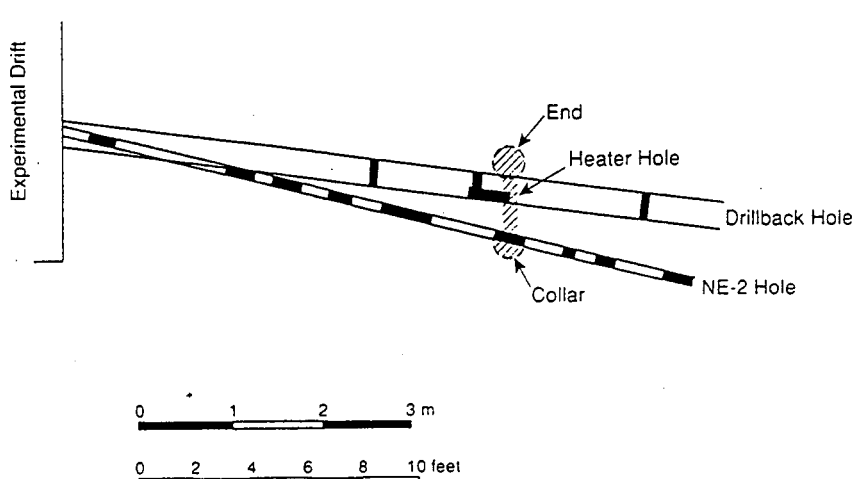

4. Vertical section perpendicular to heater hole in G-tunnel, Nevada Test Site, showing sampled intervals in core from the NE-2 hole, drilled prior to the heater hole, and the "drillback" hole that intersected the heater hole. The heater hole projects into the figure, with the end of the hole ~1 m above the elevation of its collar.

Investigations of heated core, obtained by drilling through the heater hole are presently underway. We are examining the core from sites where localized heating may have affected fracture-lining and rock-matrix constituents; preliminary results are presented here. Five subcores perpendicular to the axis of the 30 cm-diameter drillback core and 1 core parallel to the axis have been obtained, covering a span of 30 cm from the edge of the heater hole . Whole-rock gamma spectrometry of these subcores indicates a slightly lower U concentration (3.3 ppm) in the core closest to the heater hole (3.5 cm) than in the more distant cores, which average 3.5 ppm U. Thorium, averaging 16.5 ppm is nearly the same in all cores, with only a small depletion (to16.2 ppm) evident in the subcore at 10 cm from the heater hole. The mean concentrations of U and Th in the heated subcores are similar to those of the unheated core. Preliminary comparison of radioelement correlations in heated and unheated rock (Table 1) indicates that U and Th are correlated similarly, while U and K are more strongly correlated in the heated than in the unheated rock. Th and K are strongly correlated in both the heated and unheated rock.

Table 1. Correlations (r^2) Between Radioelements

	U with Th	U with K	Th with K
Heated tuff	0.47	0.59	0.96
Unheated tuff	0.43	0.28	0.93

The apparently more independent behavior of U than of Th and K in both heated and unheated tuff might be influenced by the loci of U in the rock. This is indicated by the aforementioned association of U with fracture - lining silica and also by the results of fission-track radiography of tuff close to the heater. Radiography in combination with x-ray spectroscopy (EDAX)on the scanning electron microscope show that U is asociated both with primary magnetite and ilmenite, and with secondary disseminated Mn-oxyhydroxide minerals (Fig. 5). Uranium has probably been localized in the secondary minerals by adsorption, while it appears to be incorporated in the grains and on the surfaces of the primary minerals. Fission-track determinations of U in 5 thin sections from within 10 cm of the heater hole (Fig. 6) show that U is concentrated 8 to 10 times above whole-rock values where it is associated with the primary Fe-Ti-oxide minerals and 4 to 5 times whole-rock values where it is

5. Uranium associated with primary and secondary opaque minerals in heated tuff. Top: Backscattered electron image of primary Fe-rich grain (center) and secondary disseminated Mn-rich mineral (left). Bottom: Associated fission tracks. Length of field 1.3mm.

associated with secondary, mainly Mn-oxide minerals. Where U is associated with Fe-Ti-oxide minerals in unheated core from the NE-2 hole, U concentrations are ~150 ppm, considerably higher than the concentrations shown in Fig. 6. This, together with the apparent gradient in U shown in Fig. 6 suggests a relative depletion of U associated with Fe-Ti-oxide minerals in close proximity to the heater. Electron microscopy with EDAX is being used to determine more accurately the composition of these opaque minerals. Detailed fission-track radiography and EDAX are proceeding as well on thin sections from the 5 subcores, covering a broader range (30 cm) of distance from the heater.

Taken together, observations to date suggest that U is mobile in hydrothermal systems, but that localized reducing environments provided by Fe-rich minerals and/or carbonaceous material concentrate U and thus attenuate its migration.

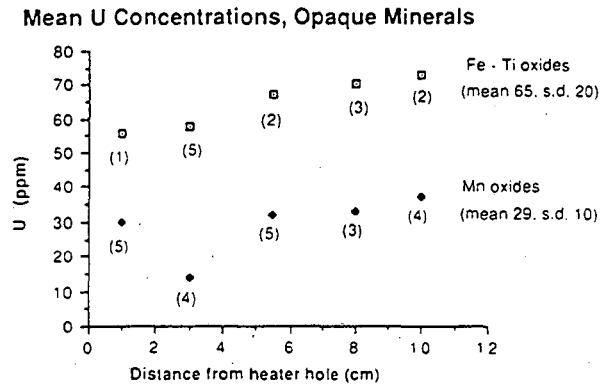

6. Uranium concentrations, by fission-track radiography, in primary Fe-Ti and secondary Mn-oxyhydroxide minerals in welded tuff within 10 cm of the heater hole. Numbers of observations are shown in parentheses.

Acknowledgements

We thank Abelardo Ramirez of LLNL for his help in arranging the drillback coring at G-tunnel, and William Glassley of LLNL for his collaboration in obtaining samples of the core.

References

1. D.G. Brookins, M.S. Abashian, L.H. Cohen, A.E. Williams, H.A. Wollenberg, and S. Flexser; Natural Analogues: Alamosa River monzonite intrusive into tuffaceous and andesitic rocks. Scientific Basis for Nuclear Waste Management VI, p. 299-306, North Holland, New York (1983).

2. Wollenberg, H.A. and S. Flexser, Contact zones and hydrothermal systems as analogues to repository conditions. Chemical Geology, 55, 345-359 (1986).

3. H. Wollenberg, M. Sorey, C. Farrar, A. White, S. Flexser, and L. Bartel; A core hole in the southwestern moat of the Long Valley caldera. EOS, 68, 649, (1987).

4. S. Flexser; Hydrothermal alteration and past and present temperature regimes in the western moat of the Long Valley caldera. Submitted to Jour. Volcanological and Geothermal Res.(1990).

5. F. Goff, D. Nielson, J. Gardner, J. Hulen, P. Lysne, L. Shevenell and J. Rowley; Scientific drilling at Sulphur Springs, Valles caldera, New Mexico: corehole VC-2A. EOS, 68, 661 (1987).

6. J. Musgrave et al.; Selected data from continental scientific drilling core holes VC-1 and VC-2A, Valles caldera, New Mexico. Los Alamos National Lab. Rept. LA-11496-OBES (1989).

7. J. Hulen, D. Nielson, F. Goff, J. Gardner and R. Charles; Molybdenum mineralization in an active geothermal system, Valles caldera, New Mexico. Geology, 15, p. 748-752 (1987).

8. F. Goff, L. Shevenell, J. Gardner, F. Vuataz, and C. Grigsby; The hydrothermal outflow plume of the Valles caldera, New Mexico, and a comparison with other outflow plumes. Jour. Geophys. Res., 93(B6), 6041 - 6058 (1988).

9. H. Wollenberg, S. Flexser, and A. Smith; Investigation of radiometric anomalies in the VC-1 hole, Valles Caldera, New Mexico. Abs. Trans. Amer. Geophys. Un., 66, p. 1081 (1985).

10. J. Connolly et al.; Petrology and geochemistry of the Grouse Canyon member of the Belted Range tuff, rock mechanics drift, G-tunnel, Nevada Test Site. Sandia National Labs. Rept. SAND 81-1970 (1983).

11. A. Ramirez, et al.; Prototype heater test of the environment around a simulated waste package. Proc. International Topical Meeting on High Level Waste Management; Amer. Nuc. Soc., Las Vegas, NV (1990).

Normal Joint Stiffness as a Function of Spatial Geometry

D. L. Hopkins, N. G. W. Cook and L. R. Myer

Introduction

Normal joint stiffness was introduced by Goodman et al. (1968) as a parameter that can be used to describe the potential behavior of a joint. An advantage of joint stiffness as a prediction parameter is that it can be measured in the laboratory without detailed analysis of the joints themselves. Stiffness has been shown to be an important parameter in determining seismic wave propagation across joints (e.g. Hopkins, 1990, and Pyrak-Nolte et al., 1990) and is probably related to their hydraulic properties.

Defined as the derivative of the curve of stress versus normal joint deformation, normal stiffness has been measured by several researchers for a large range of rock types and for both natural and induced joints (e.g. see Goodman, 1976, Bandis et al., 1983, and Pyrak-Nolte et al., 1987). In general, normal stiffness is found to be a rapidly changing curve initially that tends to flatten at high stresses. Hysteresis is usually observed for the first few loading cycles but becomes small or disappears with subsequent loading cycles (e.g. see Barton et al., 1985 and Pyrak-Nolte et al., 1987). Assuming that the hysteresis is largely due to sample preparation, the laboratory experiments show that the mechanical response of joints is elastic. The curve of joint deformation as a function of stress is also found to be highly nonlinear. It is assumed here that the nonlinearity is due to increasing numbers of asperities coming into contact with increasing stress.

While stiffness is a function of contact area, it will be shown here that stiffness is not uniquely determined by contact area. The objective of this study is to examine the relationships between normal joint stiffness and asperity dimensions, the spatial geometry of the asperities, and surface roughness.

Joint Deformation Model

It is assumed that a joint can be modeled by two parallel half-spaces separated by variable height asperities. A normal load results in displacement across the joint due to the compression of the asperities and the deformation of the half-spaces defining the joint. It has been shown that the displacement due to asperity compression is generally small (less than ten percent) compared to that due to half-space deformation (see Hopkins, 1990).

The displacement of the half-spaces is calculated from the Boussinesq solution for deformation of a semi-infinite half-space under a distributed load (see Timoshenko and Goodier, 1970). The asperities are modeled as disks and their deformation is calculated from the elastic compression of the disks. The principle of superposition is used to account for mechanical interaction between the asperities; i.e., it is assumed that displacement at any point on the half-spaces is a linear combination of the displacements due to all forces acting on asperities in the region. Since mechanical interaction is accounted for, asperities can be placed contiguously to form complicated surfaces such as those discussed in Section 4.

Given the location and height of each asperity, a displacement boundary condition is specified and numerical methods are used to find the distribution of forces across the asperities that minimizes the strain energy in the system. The model has been validated against analytical solutions including the Boussinesq solution for the distribution of stress across a rigid punch pressed into a semi-infinite half-space, and the solution for displacement due to a row of coplanar cracks derived using methods from linear elastic fracture mechanics (Hopkins, 1990).

Stiffness as a Function of Contact Geometry

For a contact area fixed at 25 percent, the joint deformation model was used to study the effect of asperity size. The asperities were of equal height (50 microns) but their diameter was varied (see Figure 1). All results in this section were generated assuming Young's modulus for the asperities and surrounding rock to be equal to 50 GPa and Poisson's ratio equal to 0.23. Results from the theory of elasticity show that for circular areas subjected to the same stress, the maximum normal displacement increases directly with the radius of the loaded area (Timoshenko and Goodier, 1970). Thus, joints comprised of large asperities would be expected to be less stiff than those with small asperities.

In designing the arrays of asperities, the relative distances between the disks were held as constant as possible so that the degree of mechanical interaction would be the same for the different arrangements. Therefore, differences in stiffness are due to the differences in the asperity dimensions. A plot of stiffness as a function of the asperity radius is shown in Figure 2. For a constant contact area, stiffness increases rapidly as the asperity radius gets small and the number of asperities gets large. The implication for joints in rock is that surfaces that form small, dispersed contacts are much stiffer than joints where the contact points are large or comprised of large clusters of contacts.

In the previous example, the distance between asperities was held constant while the size of the asperities was varied. In the next example, the dimension of the asperities was held constant and the distance between them was varied. What is really being measured is the effect of interaction. If asperities are close enough together to interact mechanically, displacement will be greater than if the asperities were more widely separated. Thus, the joint is stiffest when asperities are far apart and mechanically independent.

Consider the simple case of 25 equal height asperities arranged on a grid within the same projected area of a joint. The joint deformation model was used to calculate the stiffness of the interface as a function of the separation distance between the asperities. At the closest spacing the asperities were contiguous, and at the largest spacing they were separated by a distance equal to five times the asperity diameter (see Figure 3). Stiffness was calculated assuming that the total joint area was the same in all cases. The contiguous arrangement is found to be 80 percent less stiff than the pattern with the greatest separation distance. A plot of stiffness as a function of separation distance is shown in Figure 3. It should be noted that if interaction between the asperities were not accounted for, all of the arrangements would have the same stiffness.

For these first two examples, the contact area was held constant and it was shown that both the distance between asperities and the asperity size can significantly affect the joint stiffness. In the next example, the effect of asperity clustering is studied as a function of contact area. Stiffness was calculated for four asperity geometries (clusters of one, two, four, and eight, respectively) at six contact areas. Differences in stiffness are largely due to the differences in the size of the clusters. However, the clusters of two and eight form rectangular contacts whereas the clusters of one and four form circular and square contacts, respectively. For mechanically isolated asperities, rectangular contacts form a stiffer interface than circular or square ones (see Timoshenko and Goodier, 1970). Thus, some of the difference in stiffness observed for the different patterns is due to the difference in the geometry of the contact points.

Shown in Figure 4 are the location of the disks for three of the contact areas studied. The disks are 1 mm in diameter and 50 microns in height. Note that an attempt was made to keep the clusters as uniformly spaced over the joint area as possible. Figure 5 is a plot of stiffness versus contact area for each of the four asperity geometries. In general, consistent with the previous results, the geometries with the largest clusters are the least stiff.

Also note that there is a relatively large difference between the curves of stiffness versus contact area for clusters of four and clusters of eight at a contact of 26.0 percent (indicated by the arrow in Figure 5). The reason appears to be due to the way the clusters are arranged: the clusters of eight are arranged on a perfect rectangular grid whereas the clusters of four are arranged such that adjacent lines are staggered with respect to one another (compare Figures 4.b3 and 4.b4). At a contact of 35.7 percent, both the clusters of four and eight have a staggered arrangement (see Figures 4.c3 and 4.c4) and at a contact of 15.6 percent, both are arranged on nearly regular grids (see Figures 4.a3 and 4.a4). For both of these contact areas, the stiffness curves are much closer than for a contact of 26.0 percent; i.e. when the clusters are arranged the same way, the curves are relatively close and the difference between them is largely due to the differences in cluster size and geometry. When the arrangement of the clusters is not the same (regular grid versus staggered), there is a much bigger difference in stiffness. Thus, in addition to the dimensions and geometry of the clusters themselves, stiffness is very sensitive to the spatial relationships between the clusters.

Is it possible for stiffness to decrease when contact area increases? Recall that normal joint stiffness is the derivative of the curve of stress versus normal joint deformation. It follows that stiffness is zero for an open joint and infinite for a perfectly welded joint. Thus, by definition, stiffness is an increasing function of contact area. However, the results of this section show that contact geometry is also a very important parameter. It is possible that significant changes in geometry could cause perturbations in the otherwise increasing function of stiffness with contact area. In other words, if an increase in contact area comes about in such away so as to substantially increase interaction between the contact points from what it was at the previous level of contact, it is conceivable that stiffness would decrease.

Stiffness as a Function of Void Geometry

A joint can be envisioned as two rough surfaces in partial contact. Under a normal stress, the joint deforms, but even at high stresses large areas of void space remain. An understanding of how the geometry of the void space changes with stress is important because it strongly affects both the mechanical and hydraulic properties of the joint.

Many studies have been made of the topography of joint surfaces e.g. Brown and Scholz (1985) have derived power spectra for natural joint surfaces and Barton et al. (1985) defined a parameter that characterizes surface roughness. However, such information does not lead directly to a description of the void geometry which is defined by the difference of the two joint surfaces. As a result, not much data is available on the geometry of the void space in natural joints. For analytical and numerical studies, one alternative to measured data is data generated mathematically (e.g. see Brown, 1987). An advantage of simulating joints is that they can be modified in a controlled way so that the relationships between surface and void geometry and mechanical behavior can be studied.

In this study, the void geometry is modeled by a composite surface meaning the height at any point is the sum of the asperity heights from the upper and lower joint planes. To accurately represent natural joints, it is important to account for spatial correlation. Further, it is appealing to be able to quantify the degree of spatial correlation so that it can be tied to the mechanical response of the joint. The composite surfaces analyzed here were generated using a weighted averaging procedure. An averaging scheme is appealing in that it may replicate the metamorphosis of joints in the field.

To generate the composite surfaces a grid is defined in the x-y plane resulting in an array of contiguous, square elements. Each element is assigned a height randomly drawn from the same uniform distribution independent of the other elements. This

results in a surface where the height of each element is uncorrelated to the heights of neighboring elements. As would be expected, this surface is very rough and irregular (see Figure 6.a). The height of each element is then replaced by a weighted average of the heights of neighboring elements. The area over which the surface heights are to be correlated determines the number of neighboring elements used to compute the average. The effect of averaging is to smooth the surface. Thus, choosing to average over a very large area leads to a smoother surface than averaging over a small area.

For the surfaces described here, the weights are an exponential function of distance. The further the element from that whose height is being replaced, the smaller the weight. In all cases, the weights were assigned according to the function:

$$\text{weight}(x) = e^{-\alpha x}$$

where x is the distance to the center of the element whose height is being replaced by the weighted average and α is a parameter that was varied. For low values of α, the weights are nearly equal regardless of distance so that all elements contribute almost equally to the average. At the other extreme, for high values of α, the weights drop off very quickly as a function of distance so that outer elements contribute very little to the average.

Once all elements in the array have been reassigned heights according to the weighted average, the entire averaging procedure can be repeated which increases the area over which the heights are correlated. This arises from the fact that the heights of neighboring points are no longer independent. In summary, for fixed weights, the degree of spatial correlation is determined by the area over which the averaging procedure is applied and the number of times the averaging procedure is repeated. The smoothness of the surface is increased by increasing the area over which the averaging is done, by repeating the averaging procedure, and by a weighting scheme that gives high or equal weight to points regardless of distance.

The method described above was used to generate composite surfaces with varying degrees of spatial correlation (Figure 6.b-6.f). The total surface area is 4.84 cm^2 and the asperities have a diameter of 1 mm. Composite surface 6.b was obtained using exponential weights with α equal to 2 resulting in heights that are correlated over an area about 0.05 times the total surface area. As the figure shows, the surface is still very irregular and rough. Composite surfaces 6.c and 6.d have heights that are correlated over the same area as 6.b, but the value of α used to compute the weights was decreased to 0.8 for surface 6.c, and to 0.4 for surface 6.d. Recall that the effect of decreasing α is to give more weight to distant points so that outlying asperities have a greater effect on the average than when α is large. Increasing the weights of distant points increases the effect of smoothing as can be seen by comparing surfaces 6.b-6.d.

To obtain composite surfaces 6.e and 6.f, surface 6.d was smoothed by repeated averaging: three times to obtain surface 6.e, and ten times to obtain surface 6.f. As explained above, this results in surfaces with heights correlated over larger areas. As can be seen in Figure 6, repeating the averaging procedure three times leads to a very smooth surface and repeating it ten times leads to a surface that is essentially uniform.

For composite surfaces 6.b-6.f, the joint deformation model was used to calculate stiffness for several values of normal displacement assuming Young's modulus for the asperities and surrounding rock to be equal to 50 GPa and Poisson's ratio to be equal to 0.23 (see Figure 7). Note that the plots of stiffness versus stress are nearly linear with differences in slope reflecting the differences in the roughness of the composite surfaces (see the histograms in Figure 8 which show the distribution of element heights for each surface). In general, as would be expected, the smoother the composite joint surfaces, the stiffer the interface.

Figure 9 shows contact area for joints represented by composite surfaces 6.c and 6.e at two levels of stress. In both cases, the contact areas tend to form clusters that increase in size with increasing stress. The difference in contact areas for the two

surfaces at comparable stresses indicates the importance of considering surface roughness in fluid flow calculations.

The calculations of stiffness plotted in Figure 7 were made up to relatively high stresses (over 60 MPa). At these high stresses, elements are still coming into contact which is why the curves continue to increase with stress. As discussed previously, curves of normal stiffness versus stress obtained from natural joints often exhibit a different behavior than that shown in Figure 7; stiffness is often found to be an initially rapidly increasing function with stress, that tends to flatten and reach an asymptote at high stresses. For stiffness to reach a constant value, contact area must remain constant with increasing stress. Using a polyester film, Bandis et al. (1983) measured contact areas of approximately 40 to 70 percent for stresses up to about 50 MPa. Using a metal injection technique, Pyrak-Nolte et al. (1987) report a maximum contact area of about 40 percent for a stiff joint they tested up to a stress of about 80 MPa. Thus, 50 percent contact area is a typical value even for a stiff joint subjected to a high normal stress.

Part of the explanation for a large percentage of void area at high stresses is half-space deformation. Asperities in contact deform the joint surfaces creating pockets that remain open even under very high stresses. However, the fact that stiffness is often observed to reach a constant value at contact areas as low as 40 and 50 percent, suggests that for many joints there is not a continuum of asperity heights, but rather, tall asperities and short asperities and very few asperities with heights in-between. As a result, the tallest asperities are able to prop the joint open enough so that even at high stresses, the shortest asperities do not come into contact.

A constant stiffness at a contact area near 50 percent could never be achieved for surfaces with distributions of asperity heights like those shown in Figure 8. For these surfaces, there is a continuum of asperity heights and it would be very difficult to increase stress substantially without bringing additional asperities into contact. Note

also that the stiffnesses measured correspond to what would be expected for a relatively compliant joint (see Pyrak-Nolte et al., 1987 and Bandis et al., 1983).

For their tightest joint, Pyrak-Nolte et al. measured a stiffness that was greater than 25xE6 MPa/m for a stress of 70 MPa, and greater than 10xE6 MPa/m at the relatively low stress of 10 MPa. In an attempt to generate a surface with the high stiffnesses observed for some natural joints, the composite surface displayed in Figure 6.d was transformed to make the heights of the tallest asperities more uniform. In addition, to try and simulate the behavior whereby stiffness reaches an asymptote at high stresses, the transformation was designed so that the resulting composite surface exhibits two levels of roughness; i.e. approximately 60 percent of element heights are centered around a low value, and the remaining 40 percent are concentrated between 48 and 50 microns (see Figure 10 which shows histograms of the element heights for the original and transformed surfaces). A plot of the transformed surface is shown in Figure 11. Because of the distribution of element heights for the transformed data, the tallest 40 percent of the elements should come into contact relatively quickly and then the contact area should remain nearly constant unless high enough stresses are applied to bring the very short elements into contact. The stiffnesses calculated for this surface are plotted in Figure 12. For comparison, the curve of stiffness versus stress obtained by Pyrak-Nolte et al. for their stiffest joint is also shown. The two surfaces have roughly the same percent contact area at high stresses, but it is interesting that the curves match so well given that no attempt was made to generate a surface that matched that of Pyrak-Nolte et al. in contact geometry or in the distribution of asperity heights.

As expected, the stiffness of the transformed surface is greater than the original surface and does approach a constant value at high stress. Note that at 60 MPa, the stiffness of the transformed surface is roughly 6.5 times stiffer than the original surface (see Figure 8, Surface 6.d). This demonstrates that the uniformity in height of the

tallest asperities is an important parameter in determining the normal joint stiffness.

Summary

The results of Section 3 show that mechanical interaction between contact points is a significant parameter in determining joint stiffness and should not be neglected. The results also show that no absolute statements about the relationship between normal stiffness, contact area, and contact geometry can be made. However, some relationships are found to be generally true. The clustering of the asperities tends to make the arrangement less stiff than if the asperities were separated. Small points of contact dispersed over the entire area of the joint form a stiffer interface than large contact areas or small contacts that form clusters.

When the composite heights of the asperities form a continuum, normal stiffness increases with stress and the rate of increase is greatest for the smoothest surfaces. When the distribution of asperity heights is such that asperities tend to be either relatively tall or short, with few asperities with heights in-between, stiffness tends to level off and approach an asymptote at high stresses. Joints in which the tallest asperities are very uniform in height are much stiffer than ones where they are not. It is also shown that under constant stress, joints with different roughnesses can have significantly different contact areas which has important implications for fluid flow through joints.

References

Bandis, S.C., A.C. Lumsden and N.R. Barton, 1983, Fundamentals of rock joint deformation, *Int. J. Rock Mech. Min. Sci. & Geomech. Abstr.*, 20(6):249-268.

Barton, N., S. Bandis and K. Bakhtar, 1985, Strength, deformation and conductivity coupling of rock joints, *Int. J. Rock Mech. Min. Sci. & Geomech. Abstr.* 22(3):121-140.

Brown, S.R., 1987, Fluid flow through rock joints: the effects of surface roughness, *J. Geophysical Res.* 92:1337-1347.

Brown, S.R. and C.H. Scholz, 1985, Broad bandwidth study of the topography of natural rock surfaces, *J. Geophysical Res.* 90:12575-12582.

Goodman, R.E., 1976, *Methods of Geological Engineering in Discontinuous Rocks,* St. Paul: West Publishing Co.

Goodman, R.E., L. Taylor and T.L. Brekke, 1968, A model for the mechanics of jointed rock, *J. of the Soil Mechanics and Foundations Division,* Proc. Am. Soc. Civil Engrs. SM3:637-659.

Hopkins, D.L., 1990, The effect of surface roughness on joint stiffness and aperture, Ph.D. thesis, Univ. of California, Berkeley, California.

Pyrak-Nolte, L.J., L.R. Myer, and N.G.W. Cook, 1990, Transmission of seismic waves across single, natural fractures, Accepted for publication, *J. Geophysical Res.*

Pyrak-Nolte, L.J., L.R. Myer, N.G.W. Cook, and P.A. Witherspoon, 1987, Hydraulic and mechanical properties of natural fractures in low permeability rock, Proc. 6th Int. Cong. Rock Mech., Montreal, p. 225-231. Rotterdam: Balkema.

Timoshenko, S. P. and J. N. Goodier, 1970, *Theory of Elasticity,* New York: McGraw-Hill.

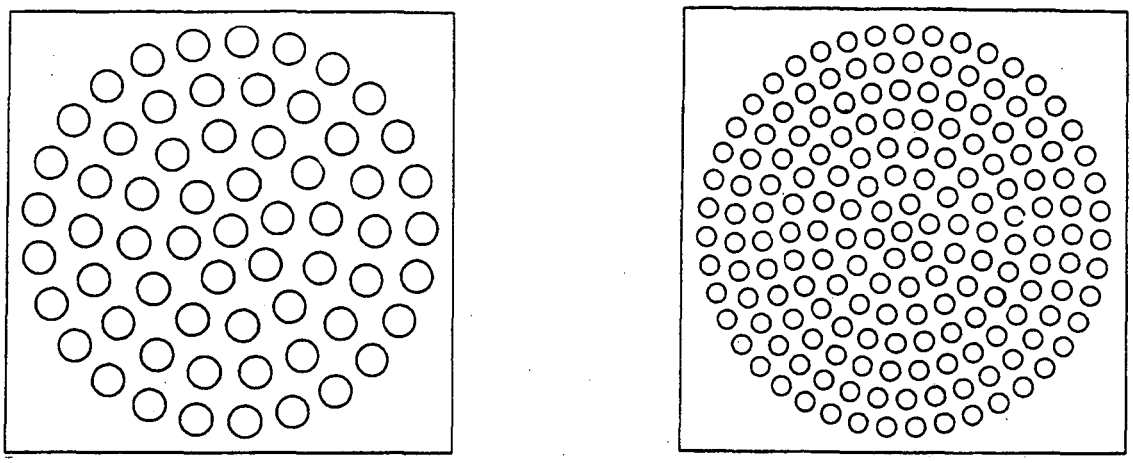

Figure 1. Location of disks for two of the arrays whose stiffness is plotted in Figure 2. Both arrays have a contact area of 25 percent. The calculated stiffnesses for the left and right-hand figures are 18.5xE6 and 50.8xE6 MPa/m, respectively.

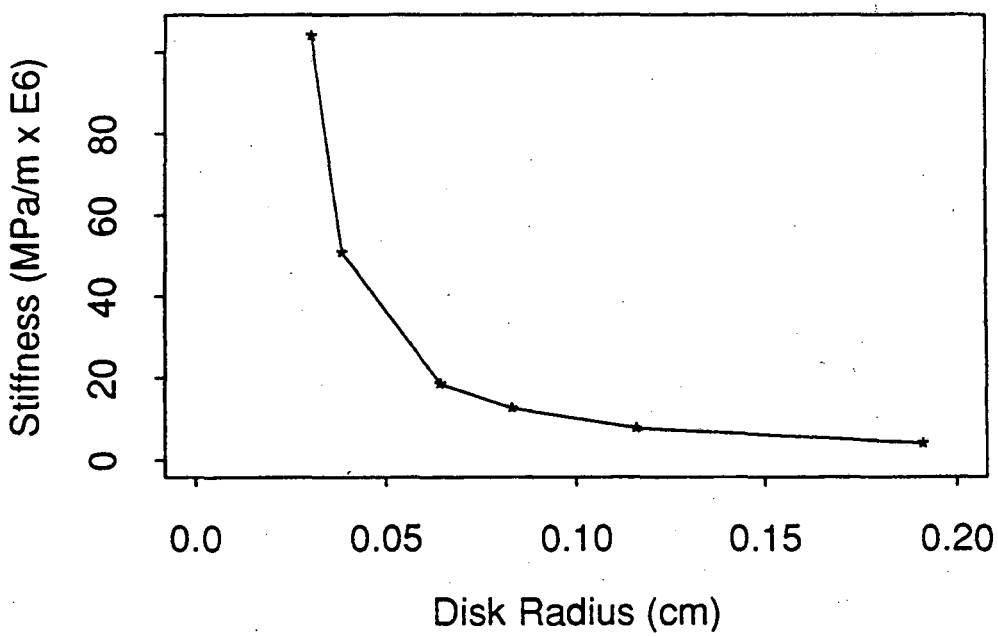

Figure 2. Normal stiffness as a function of disk radius for arrays of circular disks (see Figure 1) with contact area equal to 25 percent.

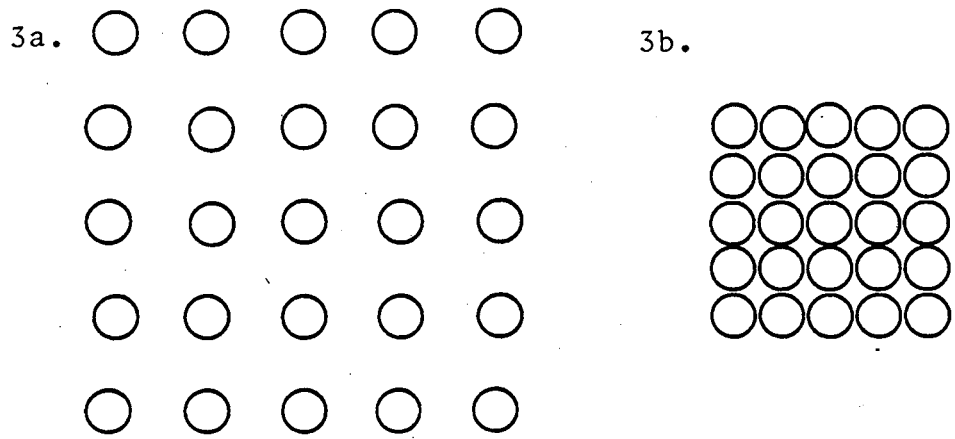

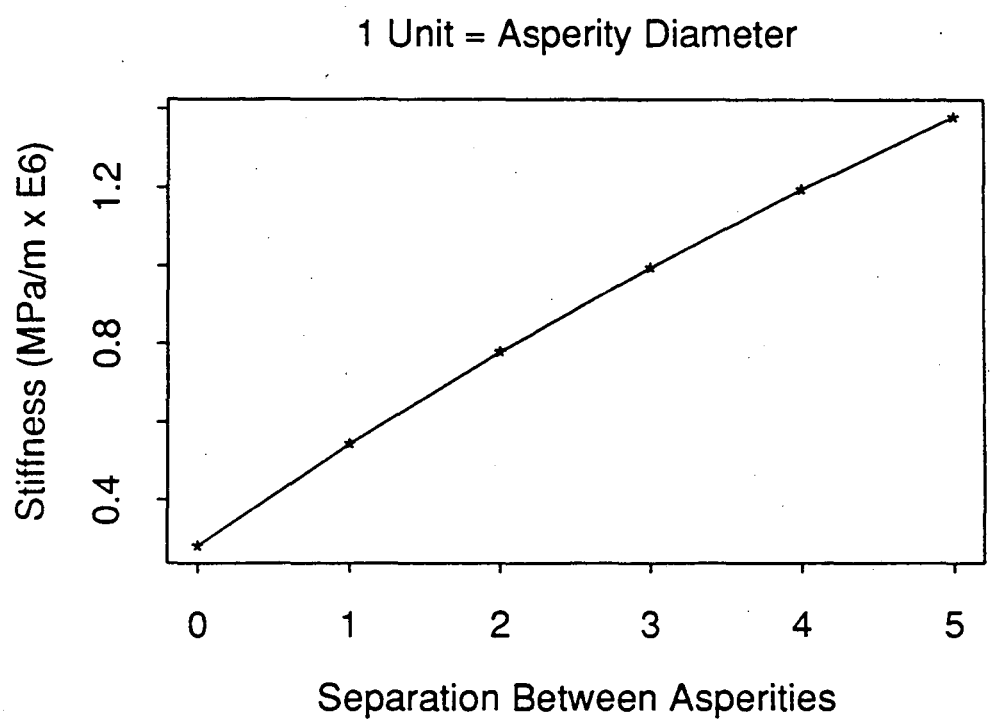

Figure 3. Normal stiffness as a function of the separation distance between asperities for a rectangular array of 25 asperities (see 3.a). At the closest spacing the asperities are contiguous (see 3.b) and at the largest spacing they are separated by a distance equal to five times the asperity diameter.

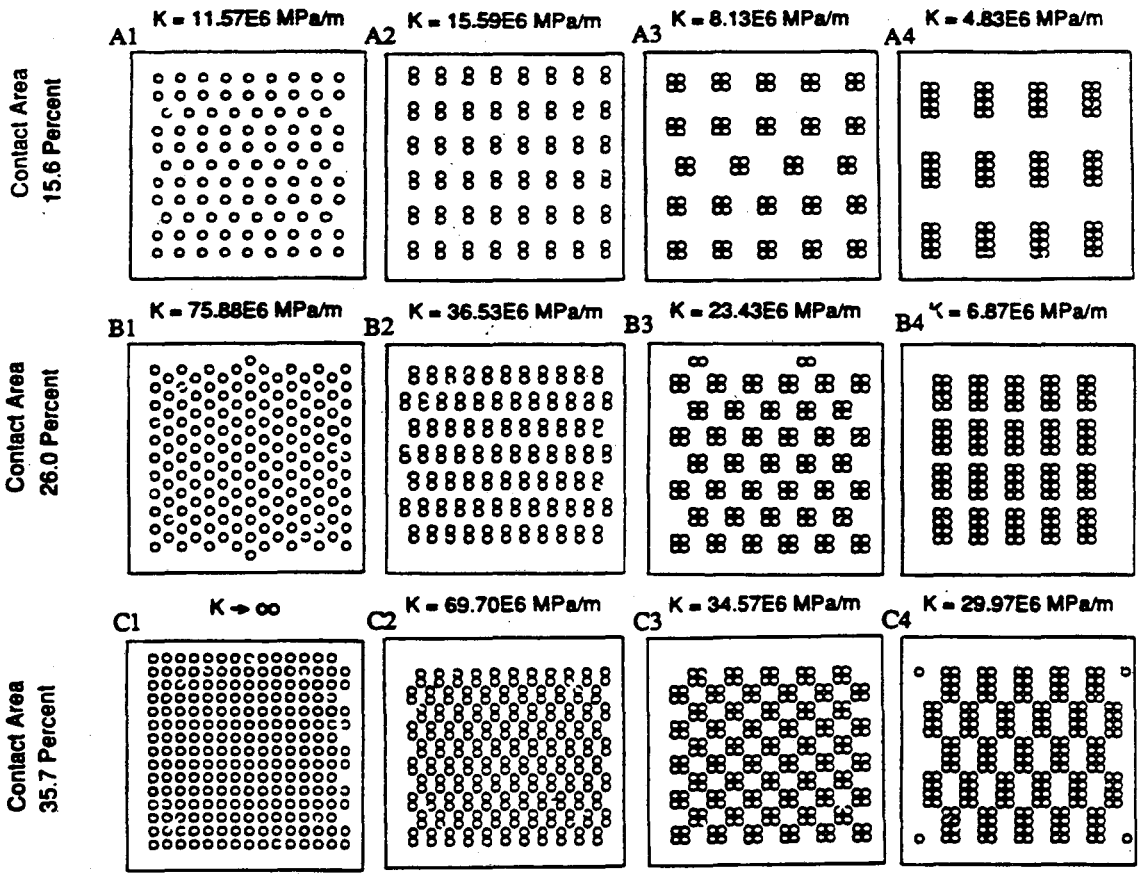

Figure 4. Locations of asperities and calculated stiffnesses for four geometries (asperities in clusters of one, two, four, and eight) and three contact areas. These stiffnesses, and those calculated for three additional contact areas, are plotted in Figure 5.

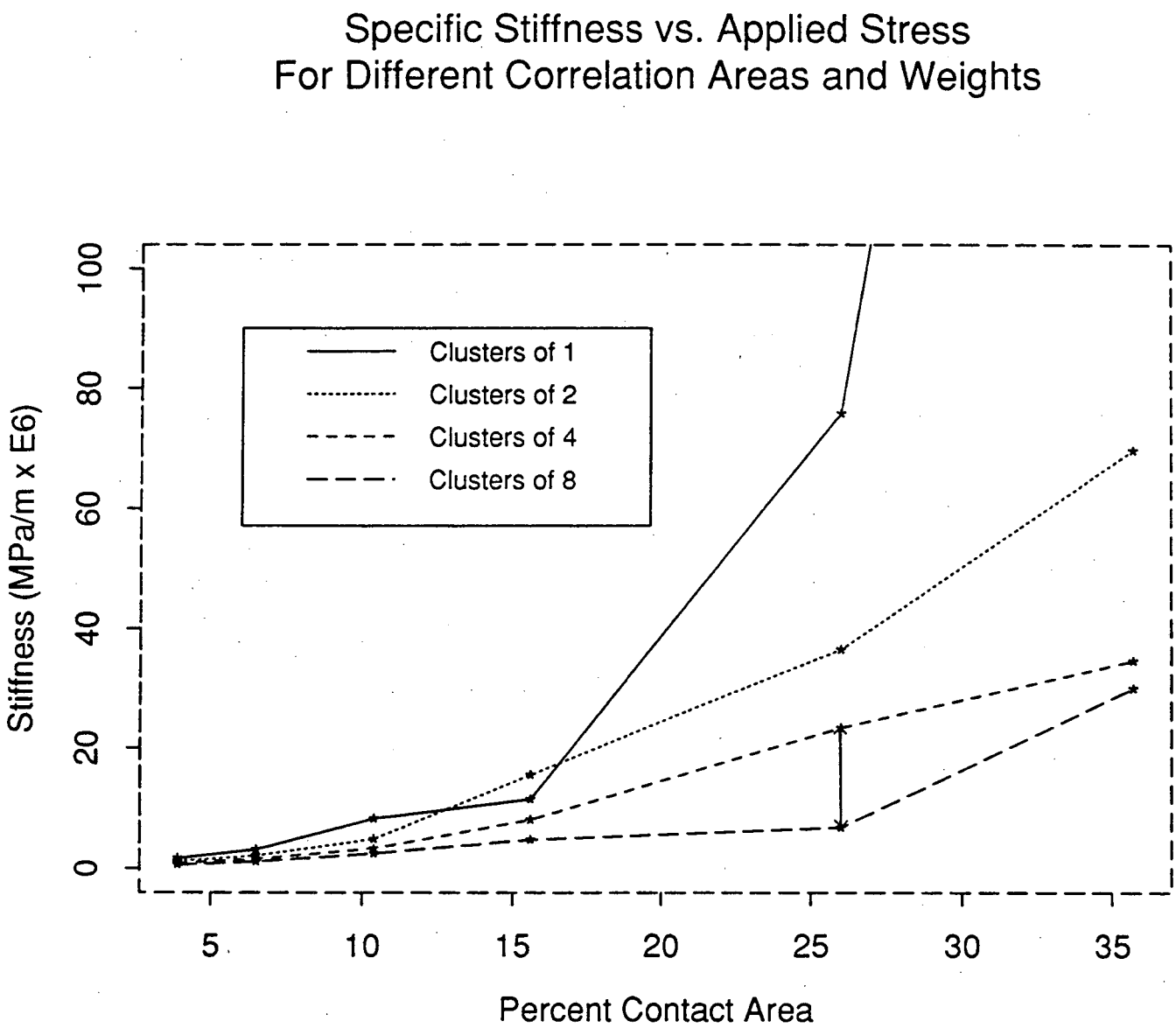

Figure 5. Normal stiffness as a function of contact area for four geometries (asperities in clusters of one, two, four, and eight) and six contact areas (see Figure 4).

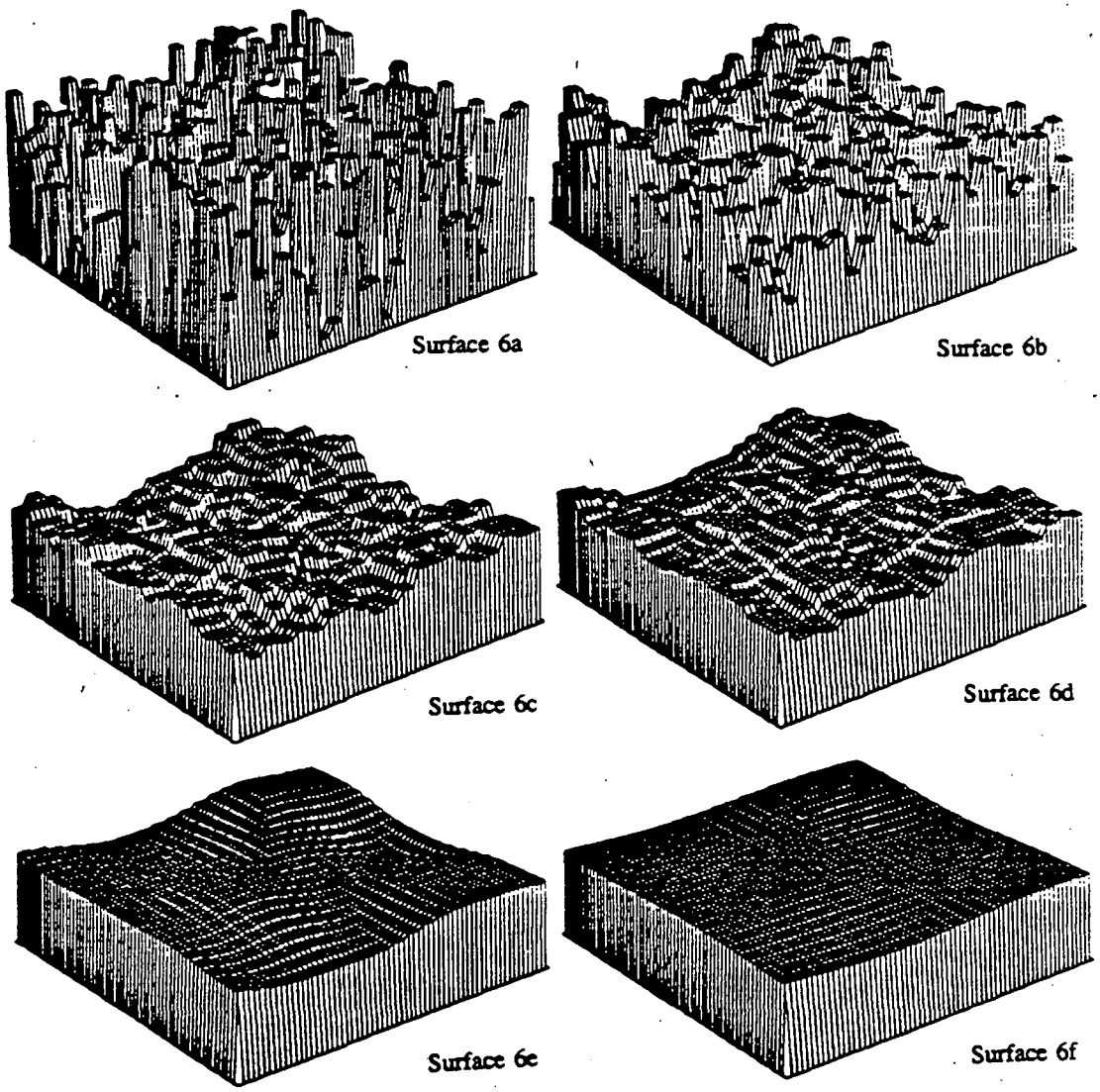

Figure 6. Composite surface 6.a is comprised of elements with heights that are uncorrelated and uniformly distributed. Surfaces 6.b-6.d were generated by smoothing Surface 6.a using a weighted averaging procedure with different weights for each of the three surfaces. Surfaces 6.e and 6.f were generated by repeated averaging of Surface 6d.

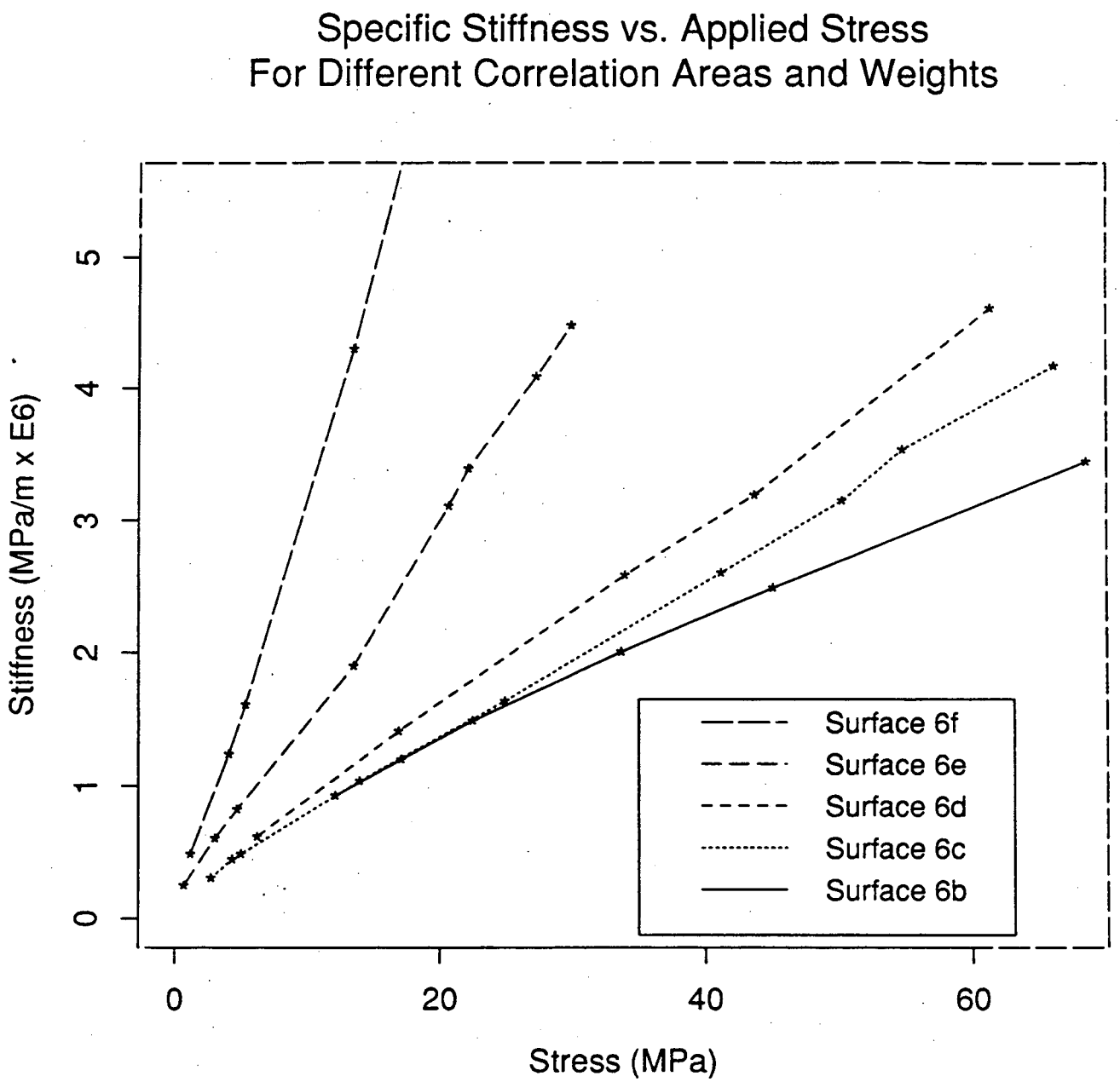

Figure 7. Normal stiffness as a function of stress for the composite surfaces displayed in Figure 6.

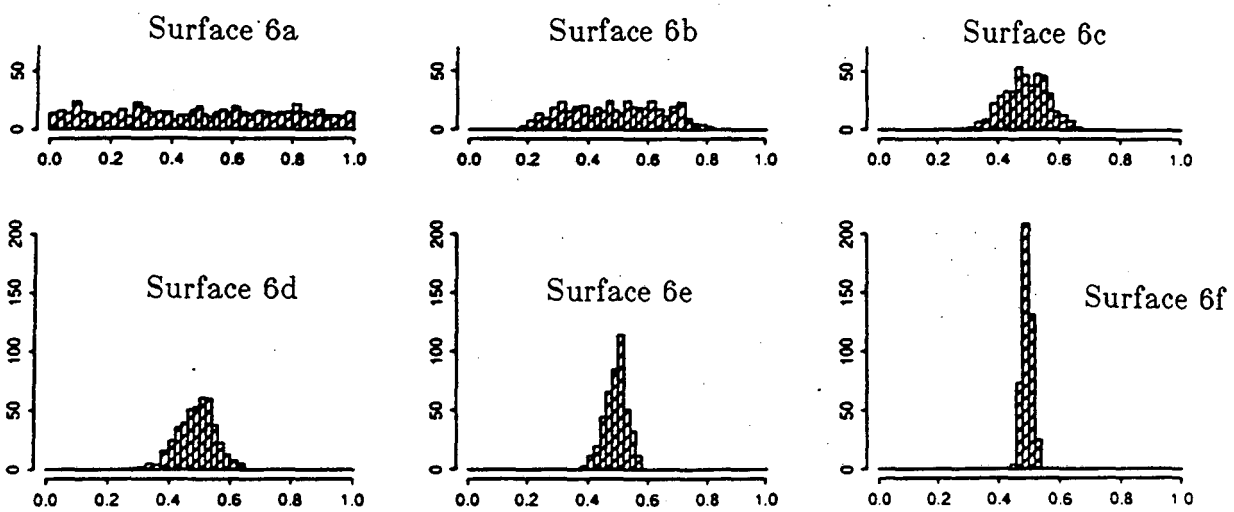

Figure 8. Histograms of the element heights for the surfaces displayed in Figure 6.

Surface 1c

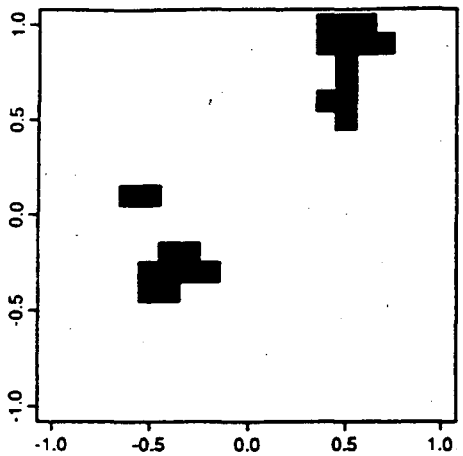

stress = 2.7 MPa

4.8% contact

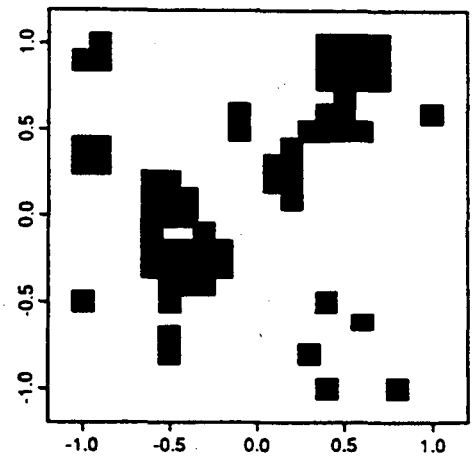

stress = 13.9 MPa

15.0% contact

Surface 1e

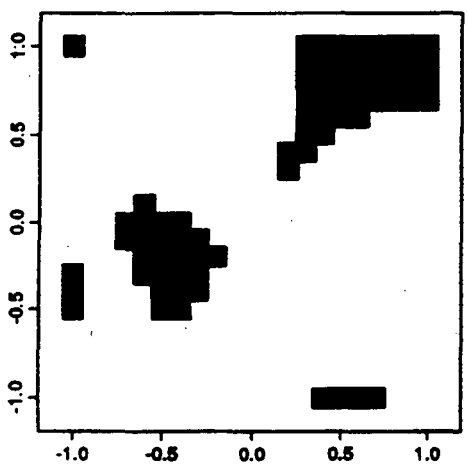

stress = 3.0 MPa

16.3% contact

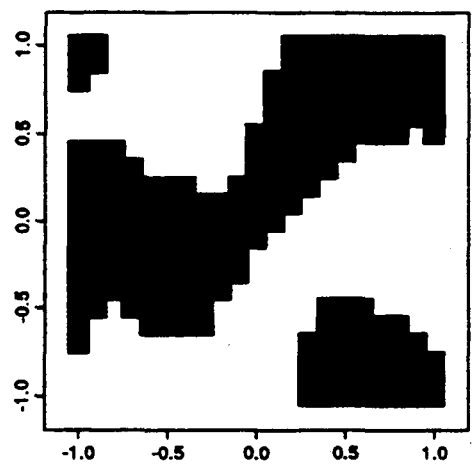

stress = 17.7 MPa

47.6% contact

Figure 9. Contact area as a function of stress for composite surfaces 6.c and 6.e. Note that for comparable stresses, the two surfaces have substantially different contact areas.

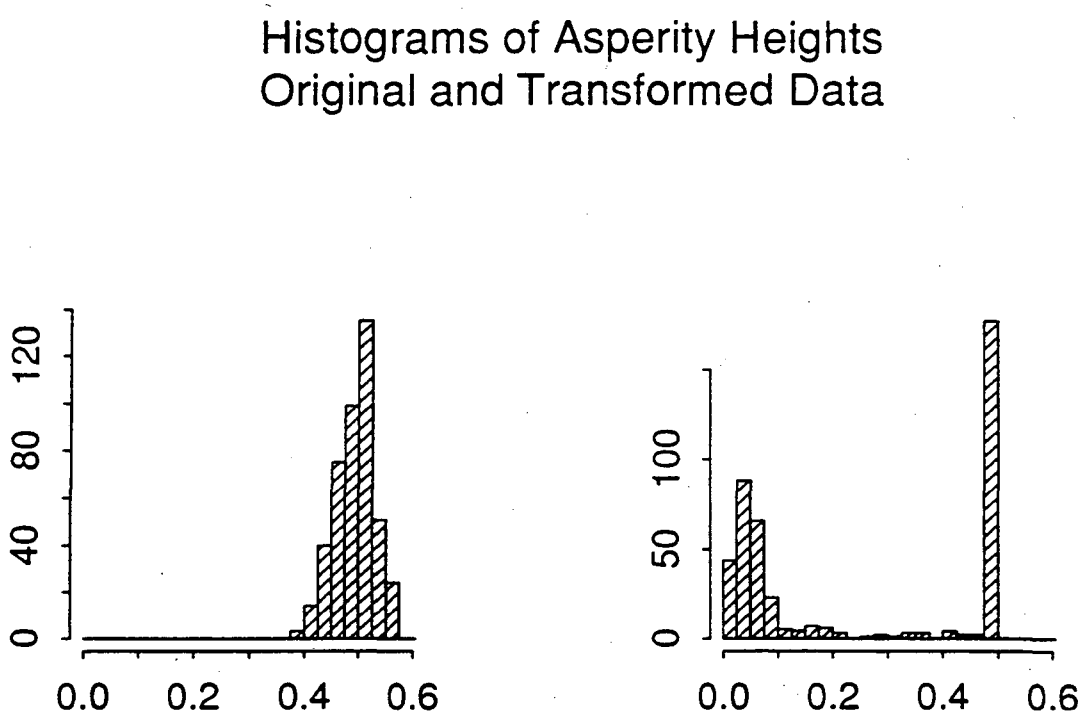

Figure 10. Histograms of the asperity heights for composite surface 6.d and 6.d with heights transformed.

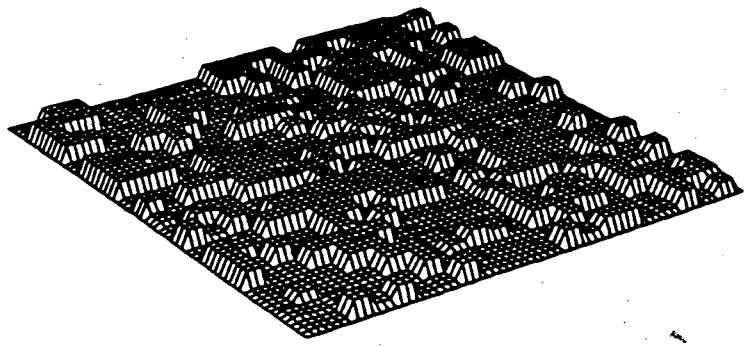

Figure 11. Composite surface 6.d transformed such that the element heights are bimodal and the tallest asperities are very uniform in height.

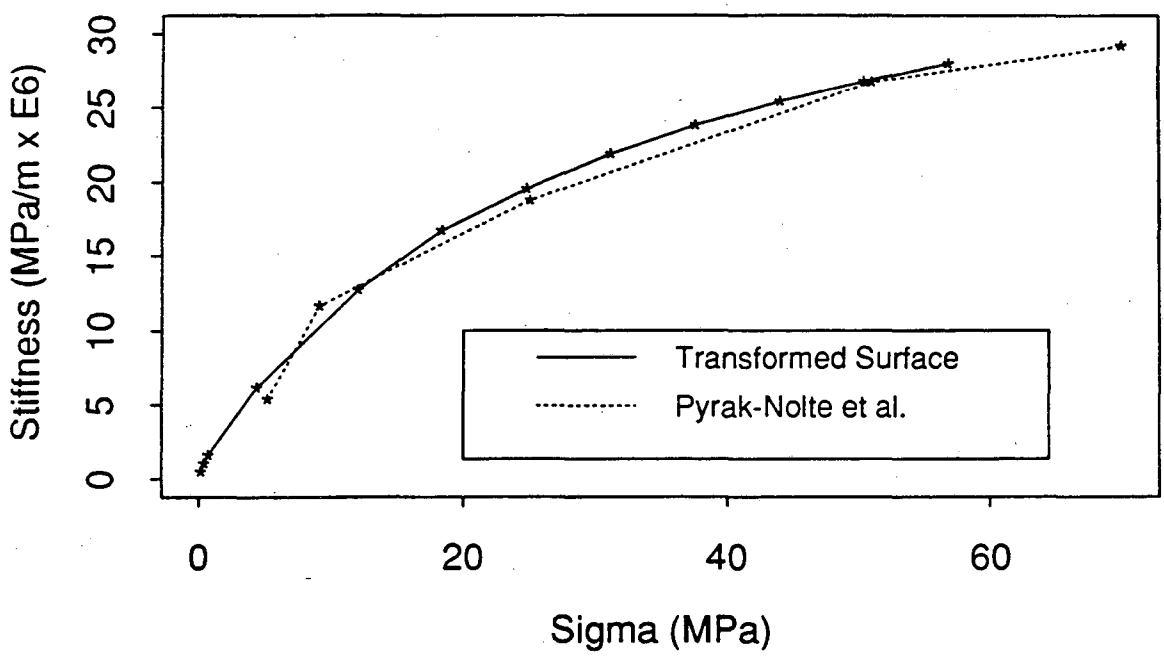

Figure 12. Stiffness as a function of stress for the composite surface displayed in Figure 11 and for a natural joint tested by Pyrak-Nolte et al. (1987).

Flow Channeling in a Single Fracture as a Two-Dimensional Strongly Heterogeneous Permeable Medium

Y. W. Tsang and C. F. Tsang

Introduction

Recent interest in the evaluation of contaminant transport in bedrock aquifers and in the performance assessment of geologic nuclear waste repositories has motivated many studies of fluid flow and tracer transport in fractured rocks. Until recently, numerical modeling of fluid flow in the fractured medium commonly make the assumption that each fracture may be idealized as a pair of parallel plates separated by a constant distance which represents the aperture of the fracture. More recent theoretical work has taken into account that the aperture in a real rock fracture in fact take on a range of values (e.g. Neuzil and Tracy, 1981; Brown, 1984). The wide range of aperture values in a single fracture give rise to a very heterogeneous two-dimensional system that one might expect the fluid flow to concentrate in a few preferred paths of least fluid resistance. Evidence that flow in fractures tends to coalesce in preferred paths has been found in the field (e.g. Abelin et al., 1988; Bourke, 1987). Motivated by these data, Tsang and Tsang (1987) proposed the variable-aperture channel model for transport through fractured media. The properties of the channel model were further developed by Tsang et al. (1988) and the channeling characteristics of flow through a two dimensional single fracture were analyzed in detail by Moreno et al. (1988). Readers are referred to those papers for more complete reference lists of previous work. Our current studies of flow channeling in a fracture as a result of the

variable apertures lead to several interesting observations that are not restricted only to flow in a fracture, but may be applicable also to flow and transport in a strongly heterogeneous porous medium. We would like to report these observations in this technical note. We shall first review briefly the methodology we use to study the flow channeling and tracer transport in a single fracture consisting of variable apertures (Moreno et al., 1988; Tsang et al., 1988). We shall then identify the relevant parameters that control flow channeling and point out how the results relate to the general problem of flow in a heterogeneous porous medium.

Channeling in Two-Dimensional Single Fractures with Strongly Varying Apertures

We use an aperture density distribution to characterize the range of aperture values in a single fracture. Based on measurement of aperture values in laboratory core samples of fractures (Gentier, 1986; Gale, 1987), we assume that the aperture values obey a log normal distribution, which is characterized by two parameters: the mean log aperture log b_o and the standard deviation (in log b) σ. In addition to the aperture density distribution parameters, the spatial correlation length λ and its anisotropy ratio λ_x/λ_y (where $\lambda^2 = \lambda_x^2 + \lambda_y^2$) for the variable apertures are needed to fully define the fracture. Given the aperture distribution and an exponential spatial covariance, variable apertures are generated by geostatistical methods similar to a procedure described in our earlier work (Moreno et al., 1988), the only difference being that the spatial correlation was assumed to be isotropic in that earlier work. Variable apertures in a fracture may also be characterized by fractal geometry (Brown, 1987; Wang et al., 1988). Given a realization of apertures, numerical flow experiments may be performed.

Figure 1 show three schematic representations of the fractures so generated. Each of the three square region in Figure 1 represents a single fracture which is discretized

into square meshes to which different aperture values are assigned. The five shadings used in the figure illustrate the varying aperture values in five steps from $b < 29$ μm to $b > 116$ μm, with the darkest shading representing the smallest apertures. The three realizations in Figure 1 are based on the same input log normal distribution with $\log b_o = 1.7$, where the aperture b_o is in μm and $\sigma = 0.43$. They have the same correlation length $\lambda = 0.2L$, where L is the dimension of the single fracture, but have different correlation anisotropy ratios of $\lambda_x/\lambda_y = 1$, 3, and 5 respectively in Figures 1a, 1b and 1c. Variograms have been computed for the apertures of all the fractures to confirm that the aperture variation obeys the required correlation length and anisotropy ratios. The increase of the correlation anisotropy ratio from 1 to 5 in the Figures 1a, 1b and 1c is also visually evident.

Following our earlier formulation (Moreno et al., 1988), we write down Darcy's law locally for each grid block where the permeability is assumed to be proportional to the square of the local aperture. Then the fluid pressure at each node may be computed with a constant pressure difference maintained across the single fracture on two opposite fracture boundaries, and no flow conditions imposed on the two remaining boundaries. From the calculated fluid potential at each node, the fluid flow rate between each pair of nodes within the fracture may be computed. We carried out our numerical experiments on over 200 realizations of fractures, but will based our discussion of results on typical illustrative examples as shown in Fig 1. The flow rates calculated for the fracture as shown in Figure 1b are displayed in Figure 2. Figure 2a shows the fluid flow when the pressure difference is applied on the left and right boundaries of the fracture and no flow boundary conditions are imposed on the top and bottom boundaries; Figure 2b shows the fluid flow when the pressure difference is applied on the top and bottom boundaries of the same fracture, while no flow condition is imposed on the left and right boundaries. The calculated flow rates between nodes cover a range of values over four orders of magnitude as a result of the log normal

aperture distribution of the fracture. Five levels of shadings: space, dash line, solid line, thicker solid line and thickest solid line are used to represent the ascending values of the flow rates.

It is apparent from Figure 2 that although flow occurs in the entire plane of the fracture, the majority of flow takes place in a few selected pathways. With both geometrical configurations of boundary conditions (pressure difference from left to right and pressure difference from top to bottom), preferred paths of large flow rates are present, though the flow pattern is quite different for the two flow directions. These preferred flow paths are what we call channels, along which the apertures are variable. Thus these channels are preferred paths in the sense of stream-tubes in the hydraulic potential theory, due to the strong variation of the aperture and hence permeability value. The channeling effect described here occurs in addition to the physical or structural large-permeability channels in the fractured medium, such as those observed near the intersection of orthogonal fractures (Abelin et al., 1988).

The pattern of large flow rate channels (Figure 2a) observed for the constant pressure boundary conditions applied to the left and right boundaries is quite different from that (Figure 2b) observed for the constant pressure boundary conditions applied to the top and bottom boundaries of the same fracture. Similar results are obtained for the fractures in Figures 1a and 1c. Furthermore, the ratio of effective permeabilities for the flow in the two orthogonal directions are respectively 0.8, 2.2 and 2.8 for the fractures in Figures 1a, 1b, and 1c, with the larger permeability for flow in the direction of the larger correlation length in cases 1b and 1c. This implies that the anisotropy ratio of hydraulic conductivity ranges from 1 to 3 in these cases.

If the pattern of flow channeling appears to be quite different for overall flow in orthogonal directions for the same fracture, can we find parameters which are common to flow in both directions and which characterize the fluid and transport in the fracture? To study this, we discretize the two-dimensional system with a square mesh and

calculate tracer transport through the fracture using the particle tracking method, which was first applied to study the dispersion of a heterogeneous porous medium by Smith and Schwartz (1980), and recently applied specifically to a fracture with variable apertures by Moreno et al., (1988). A sufficiently large number of particles, in our case four thousand, are introduced on the high pressure side of the fracture and are allowed to travel through the system with the probability of entering a particular flow section in the fracture proportional to the local flow rate. A sensitivity study of the results as a function of particle number, up to 20,000 particles has been made and showed that 4000 is indeed sufficient. When a particle comes to an intersection with two or three outgoing flow sections, a Monte Carlo method is used to assign the particle to one of the flow directions with probability weighed by their respective flow rates. As each of the particle travels through the fracture, the aperture values along its flow path are recorded to generate the statistics of the aperture values of the flow channels. The parameter values of a log normal distribution fitted to the apertures values are tabulated in Table 1, and the actual aperture density distribution functions are shown in Figure 3. The solid line gives the probability density distribution of apertures over the entire two-dimensional plane of the fracture. The dot-dash line and the short dash line give the aperture density distributions which describe the apertures along the actual flow paths of the particles for the boundary conditions of overall left-right flow and top-bottom flow respectively. All three curves are normalized to unit total integrated probability. Figures 3a, 3b, 3c correspond to the results for the fractures with aperture variation as shown in Figures 1a, 1b, 1c respectively.

It is clear from both Table 1 and the distributions shown in Figure 3 that the tracer particles favor large apertures and avoid small apertures of the two-dimensional fracture. However, they cannot avoid the small apertures altogether and thus there is a finite probability of flow through apertures one or two orders of magnitudes smaller than the large apertures most particles travel through. Note from Table 1 that the

aperture density distributions of the tracer particle flow paths tend to take on a larger mean in log b and a smaller spread (σ) than the distribution for the apertures of the entire two-dimensional fracture. By generating realizations of two-dimensional aperture distribution for different value of σ, we have studied the shifts in log b_o and σ^2 of the permeability distribution function for the particle channels relative to those for the two-dimensional distribution as a function of σ^2. Figure 4 shows the results that the shifts are large for large σ^2 and decreases as the medium becomes more homogeneous.

That the tracer particles sample an aperture distribution function which has a larger mean value than that of the aperture values for the entire two-dimensional fracture follows from the assumption that particles at a flow junction enter the exit branches proportional to their respective flow rates. Some insight to this may be gained by considering two limiting examples. In one limiting case where all the variable apertures in the two-dimensional fracture under the imposed pressure gradient were to be arranged in parallel, then the flow through each branch is proportional to b^3, and the apertures seen by the tracer particles will be given by the two-dimensional fracture aperture distribution n(b) db weighted by b^3. It can be shown by simple algebraic manipulation that the weighted log normal distribution results again in a log normal distribution, that is,

$$n(b)\,db = \frac{1}{\sqrt{2\pi}\,(\sigma \ln 10)\,b} \exp \frac{-(\log b - \log b_o)^2}{2\sigma^2}\,db \tag{1}$$

$$b^m\, n(b)\,db \rightarrow n'(b)\,db \tag{2}$$

where $n'(b)$ is a log normal distribution with a mean

$$\log b_o' = \log b_o + m\sigma^2 \ln 10. \tag{3}$$

For the values m = 3 and σ = 0.34 from Table 1, the shift in the mean is $m\sigma^2 \ln 10 = 0.80$. For the opposite limiting case where all the variable apertures in the two-dimensional fracture under the imposed pressure gradient are arranged in

series, the apertures seen by the tracer particles will be identical to those in the entire two-dimensional fracture resulting in zero shift in the mean. In reality, the apertures in the two-dimensional fracture is neither arranged purely in parallel nor purely in series. Hence the shift in log b_o seen by the tracer particles is found to be in the range of 0.24 to 0.35 from Table 1 from the numerical computations. These values lie between the lower limit of 0.0 and the upper limit of 0.80 as predicted from the idealized series and parallel arrangement of the variable apertures.

Now the parameters in Table 1 also show that the aperture parameters along the channels are almost identical for the two orthogonal flow geometries (left-right and top-bottom flows). The similarity between the aperture density distribution functions for the two orthogonal flow geometries is apparent in Figure 3. This is not obvious a priori, since the channels in the two cases represent rather different flow paths (Figure 2a and 2b). The result is even less obvious when one considers that the anisotropy ratio of the correlation length is a factor of 5 for the case in Figures 1c and 3c. Based on results of numerical experiments using different values of correlation lengths, we conclude that the insensitivity of the aperture values of the flow paths in the two orthogonal directions of overall flow arises from the fact that the correlation length chosen here is 0.2L, where L is the flow region. Hence the scale of heterogeneity is small enough for the particles flowing in orthogonal directions to sample statistically similar values of aperture along the flow paths. In the limit that the scale of heterogeneity is increased to the size of the flow region, the large anisotropy ratio in the aperture correlation length would give rise to a highly stratified medium through which the flow should consist of major conduits of very large apertures in the direction parallel to the large correlation length, but many smaller apertures are sampled in the orthogonal direction. When this happens, the aperture density distribution of the particle flow paths will be dependent on the flow direction with respect to correlation anisotropy.

In an earlier work (Tsang et al., 1988) where we interpreted tracer data in terms of a channel model, we have related the dispersion of the tracer transport to the parameters of the aperture density distribution of the flow channels. Then the above results indicate that as long as the flow region is a few times larger that the spatial correlation length, the dispersion of the medium may be characterized within the channel model. These results are interesting in that their validity holds even for the scale where the flow region is only a few times larger than the aperture correlation length. On this spatial scale, large variability of the flow properties is manifested in the pattern of flow channeling which are very realization and flow direction dependent. Yet the tracer transport may be characterized by an aperture density distribution (of the flow channels), whose parameters are independent of the deterministic flow path patterns or the anisotropy ratio of the spatial correlation.

Applicability of Single Fracture Results to a Two-Dimensional Heterogeneous Porous Medium

The properties observed for the above calculations for a single fracture with variable aperture may have relevance to flow in a heterogeneous two-dimensional porous medium which has been extensively studied by a number of authors using stochastic theory (e.g. Dagan, 1982, 1984; Gelhar and Axness, 1983). The heterogeneity of a porous medium is typically expressed in terms of a permeability probability distribution n(k) where the scale of heterogeneity is expressed in terms of a correlation length in the spatial variation of k. In their survey of 31 regional aquifers, Hoeksema and Kitanidis (1985) show that the hydraulic conductivity and transmissivity are in general well approximated by the log normal distribution. In our single fracture calculations, the stochastic variable is the log normally distributed fracture aperture b which relates to the local permeability by the relation $k = b^2/12$. Then the above results obtained for the fluid flow behavior in a single fracture treated as a two-dimensional heterogeneous

system may be analogous to transport in a highly heterogeneous porous medium (one with a large variance in the permeability density distribution). We may then make the following remarks regarding fluid flow in a strongly heterogeneous two-dimensional porous medium. The heterogeneous medium would give rise to flow channeling, and provided that the largest scale of heterogeneity is not more than a few tenths of the scale of measurement, the least resistive channels for tracer transport are characterized by a permeability distribution which typically takes on a larger mean and a smaller variance than the permeability distribution of the entire two-dimensional medium. The deviation of the parameters of the permeability distribution along the flow channels from those of the whole two-dimensional region increases with the variance of the original permeability distribution (Figure 4). Flow channeling is expected to occur in a strongly heterogeneous medium, which by definition will have a large variance in the permeability distribution.

We should point out here that the tracer travel time calculations of the above single fracture calculations are not immediately translated to the porous medium case, since in most of the current formulations, the porosity of a porous medium is assumed to be constant while the permeability is allowed to take on a wide range of values. In contrast, in the above calculations for the single fracture, the porosity or aperture is also a stochastic variable.

Conclusions

The present note discusses a number of observations made in our investigation of transport through a strongly heterogeneous two-dimensional system:

(1) Heterogeneity due to aperture variability in a single fracture or permeability variability in a porous medium gives rise to flow channeling. One possible consequence is that since tracers traversing through such a medium will predominantly take a number of main paths, the effective rock area for interaction with tracers is

much less than in the case when channeling is absent.

(2) These channels for tracer transport are characterized by a probability distribution function for fracture aperture (or permeability) values. This distribution for the flow channels differs from that for the entire two-dimensional medium; specifically, it has a larger mean and smaller variance. The shifts in the mean and variance increase with the variance of the two-dimensional distribution.

(3) The above conclusions are valid for a range of correlation length anisotropy. We showed that the characteristic permeability distribution along the paths of tracer transport is independent of anisotropy as given by $\lambda_x/\lambda_y = 1, 3, 5$, where λ_x and λ_y are the spatial correlation lengths in the two orthogonal directions. We believe that this condition is true if either λ_x or λ_y is no larger than 1/5 of the transport distance L.

Acknowledgements

Continued discussions with L. Moreno and I. Neretnieks of the Royal Institute of Technology, Stockholm, Sweden are much appreciated. Review and comments from C. Carnahan and J. Wang at Lawrence Berkeley Laboratory are gratefully acknowledged. The work is supported in part by the Office of Civilian Radioactive Waste Management, Office of Geological Repositories, Engineering and Geotechnology Division, through the U. S. Department of Energy Contract DE-AC03-76SF00098.

References

Abelin, H., L. Bergersson, J. Gidlund, L. Moreno, I. Neretnieks, H. Widen and J. Andersson, Results of some large scale in situ tracer experiments in a drift at the Stripa Mine, Proceedings of International Conference on Fluid Flow in Fractured Rocks, Atlanta, Georgia, May 16-18, 1988.

Bourke, P. J., Channeling of flow through fractures in rock, Proceedings of GEOVAL-87, International Symposium, Stockholm, Sweden, April 7-9, 1987.

Brown, D. M., Stochastic analysis of flow and solute transport in a variable-aperture rock fracture, M. S. Thesis, Mass. Instit. of Tech., Cambridge, Mass., 1984.

Brown, S. R., Fluid flow through rock joints: the effect of surface roughness, Jour. Geophys. Res., 92(B2), 1337-1347, 1987.

Dagan G., Stochastic modeling of groundwater flow by unconditional and conditional probabilities. 2. The solute transport., Water Resour. Res., 18, 835-848, 1982.

Dagan G., Solute transport in heterogeneous porous formations, J. Fluid Mechanics, 145, 151-177, 1984.

Gale, J. E., Comparison of coupled fracture deformation and fluid flow models with direct measurements of fracture pore structure and stress-flow properties, Proceedings of 28th U. S. Symposium of Rock Mechanics, Tuscon, Arizona, June 29-July 1, 1213-1222, 1987.

Gelhar, L. W. and C. L., Axness, Three-dimensional stochastic analysis of macro-dispersion in aquifers, Water Resour. Res., 19(1), 161-180, 1983.

Gentier, S., Morphologie et comportment hydromecanique d'une fracture naturelle dans un granite sous contrainte normale, Doctoral Thesis, U. d'Orleans, France, 1986.

Hoeksema, R. J. and P. K. Kitanidis, Analysis of the spatial structure of properties of selected aquifers, Water Resour. Res., 21(4), 563-572, 1985.

Moreno, L., Y. W. Tsang, C. F. Tsang, F. V. Hale and I. Neretnieks, Flow and tracer transport in a single fracture: A Stochastic Model and its relation to some field observation, Water Resour. Res., 24(12), 2033-2048, 1988.

Neuzil, C. E. and J. V. Tracy, Flow through fractures, Water Resour. Res., 17, 191-199, 1981.

Smith, L. and F. W. Schwartz, Mass transport, 1, A stochastic analysis of macroscopic dispersion, Water Resour. Res., 16(2), 303-313, 1980.

Tsang, Y. W. and C.F. Tsang, Channel model of flow through fractured media, Water Resour, Res., 23(3), 467-479, 1987.

Tsang, Y. W., C. F. Tsang, I. Neretnieks, and L. Moreno, Flow and tracer transport in fractured media—A variable aperture channel model and its properties, Water Resour. Res., 24(12), 2049-2060, 1988.

Wang, J. S. Y., T. N. Narasimhan, and C. H. Scholz, Aperture correlation of fractal fracture, J. Geophys. Res., 93(B3), 2216-2224, 1988.

Table 1

Statistics of the aperture density distribution for the two-dimensional fracture and along the particle paths for the left-right and top-bottom flow configurations

			2-D Fracture	Left-Right Flow	Top-Bottom Flow
(a)	$\lambda = 0.2L$	$\log b_o$	1.78	2.05	2.05
	$\frac{\lambda_x}{\lambda_y} = 1$	σ	0.35	0.28	0.27
(b)	$\lambda = 0.2L$	$\log b_o$	1.70	1.99	1.94
	$\frac{\lambda_x}{\lambda_y} = 3$	σ	0.34	0.25	0.26
(c)	$\lambda = 0.2L$	$\log b_o$	1.74	2.09	2.00
	$\frac{\lambda_x}{\lambda_y} = 5$	σ	0.34	0.32	0.34

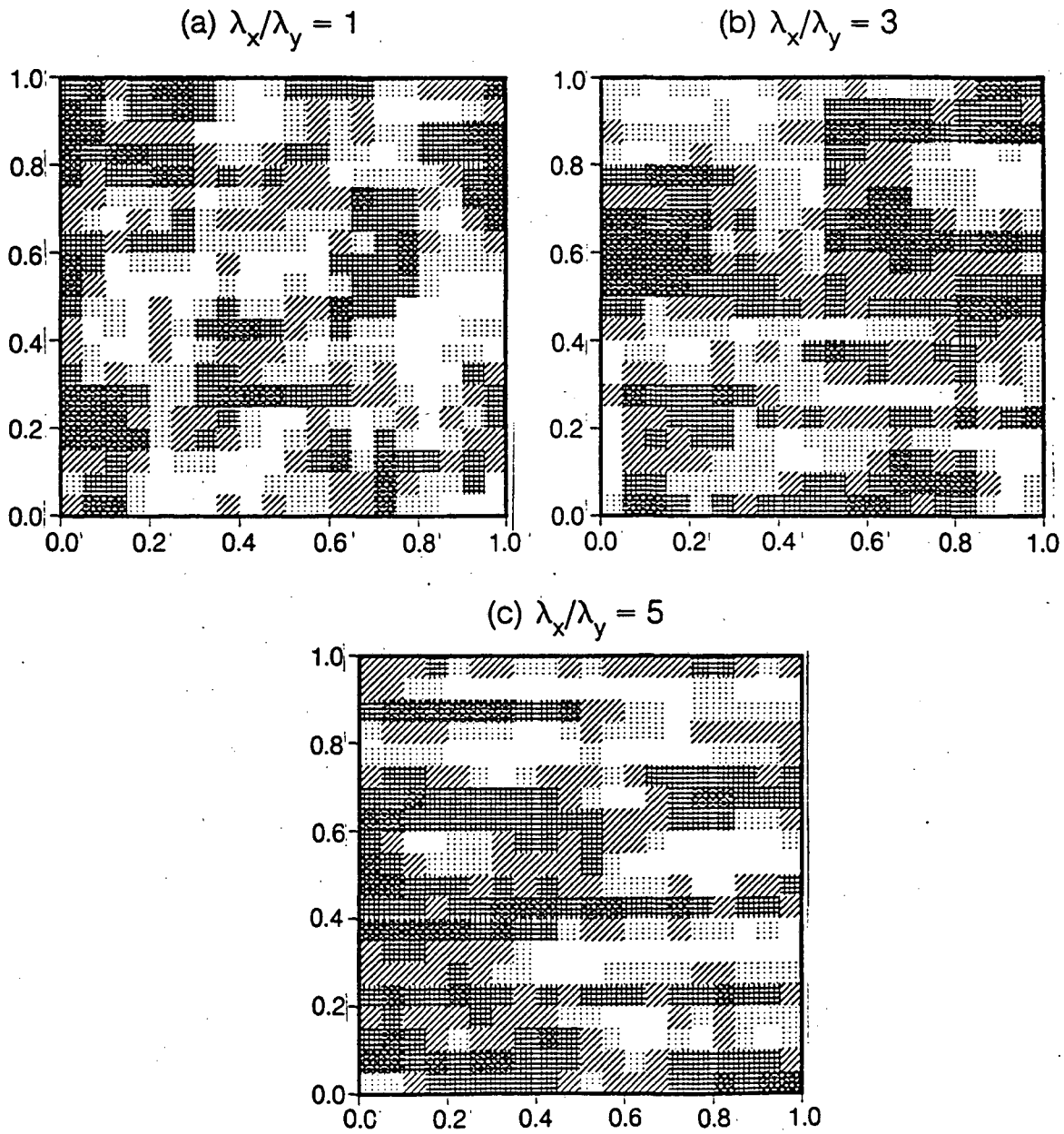

XBL 8811-10568

Figure 1. Statistically generated apertures with spatial correlation length of 0.2L in the plane of a single fracture of linear dimension L. The aperture values are partitioned into five classes with the smallest apertures corresponding to the darkest shading. The three realizations have different anisotropy ratio for the spatial correlation length: (a) λ_x/λ_y=1, (b) λ_x/λ_y=3, and (c) λ_x/λ_y=5.

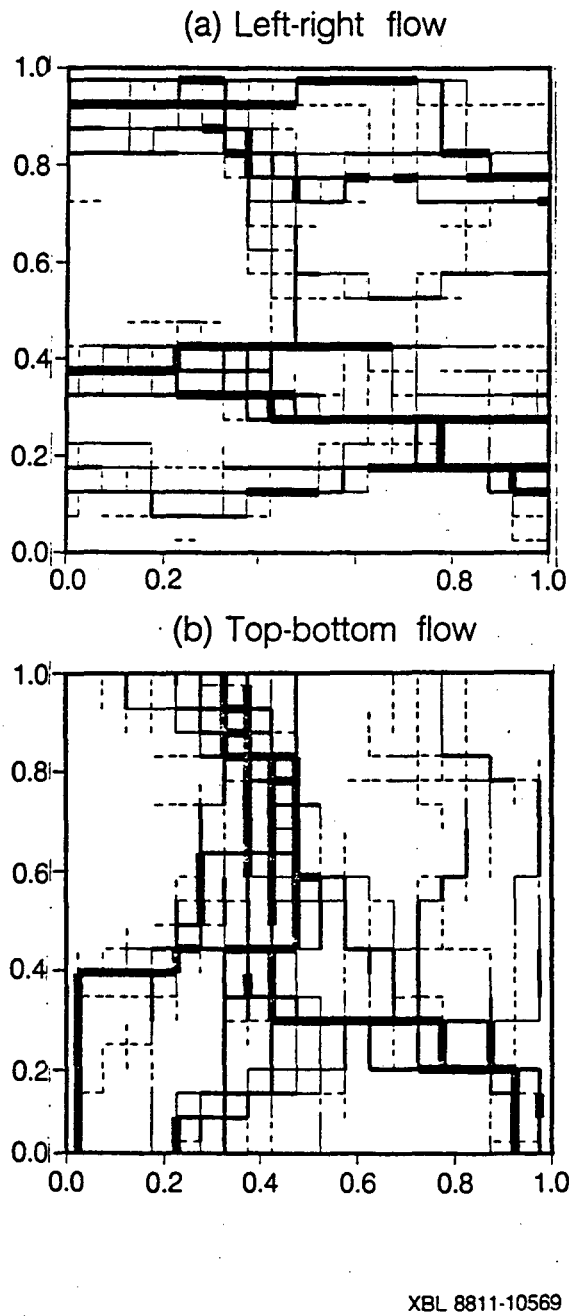

Figure 2. Fluid flow rates for the fracture with aperture variations as shown in Figure 1b. The thickness of the lines is proportional to the flow rates. Pressure difference is applied from (a) left to right, and (b) top to bottom.

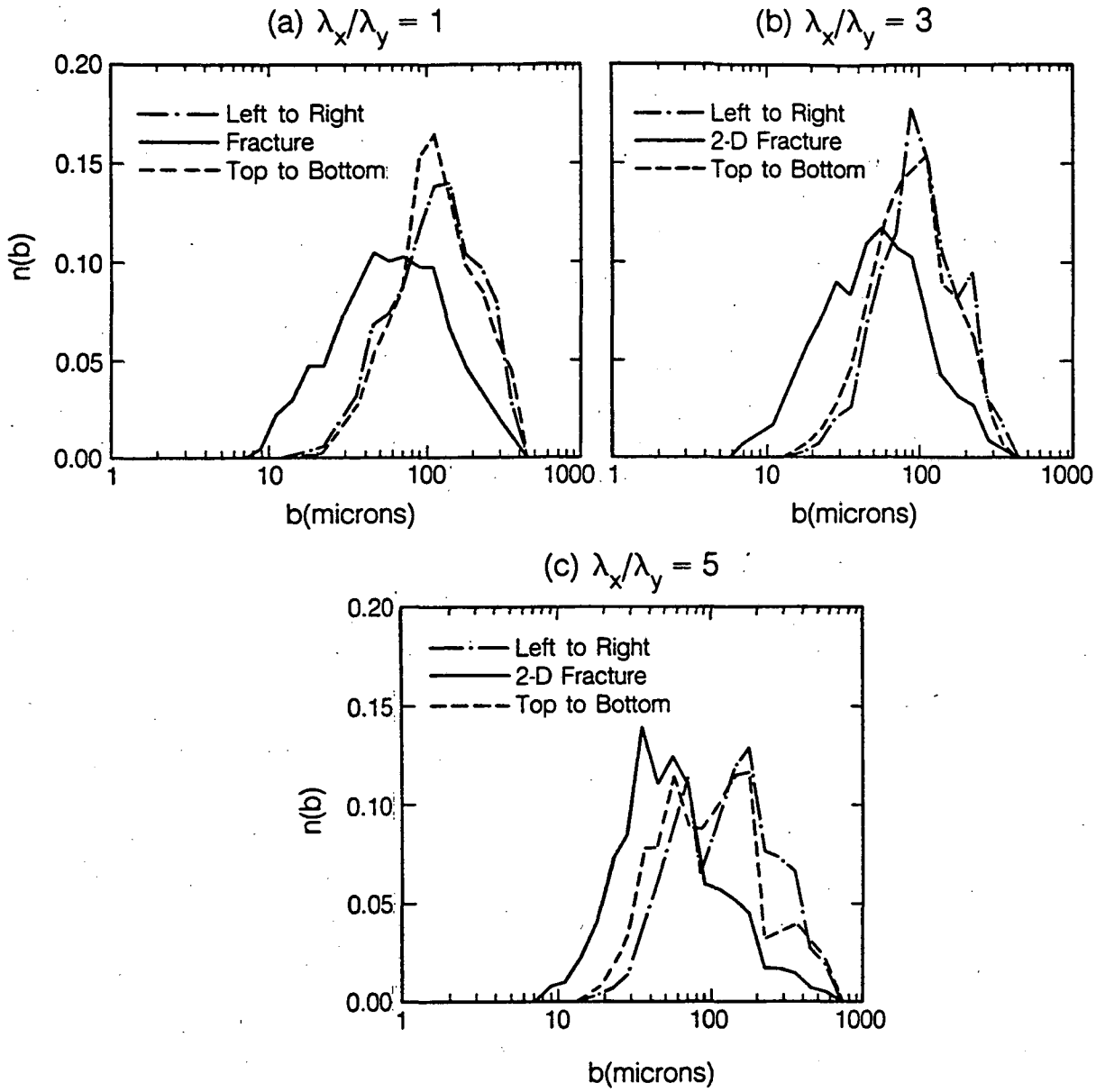

XBL 8811-10570

Figure 3. The aperture probability density distributions for apertures over the 2D fracture, along flow paths with left-right pressure difference, and along flow paths with top-bottom pressure difference for the fractures shown in (a) Figure 1a, (b) Figure 1b, and (c) Figure 1c.

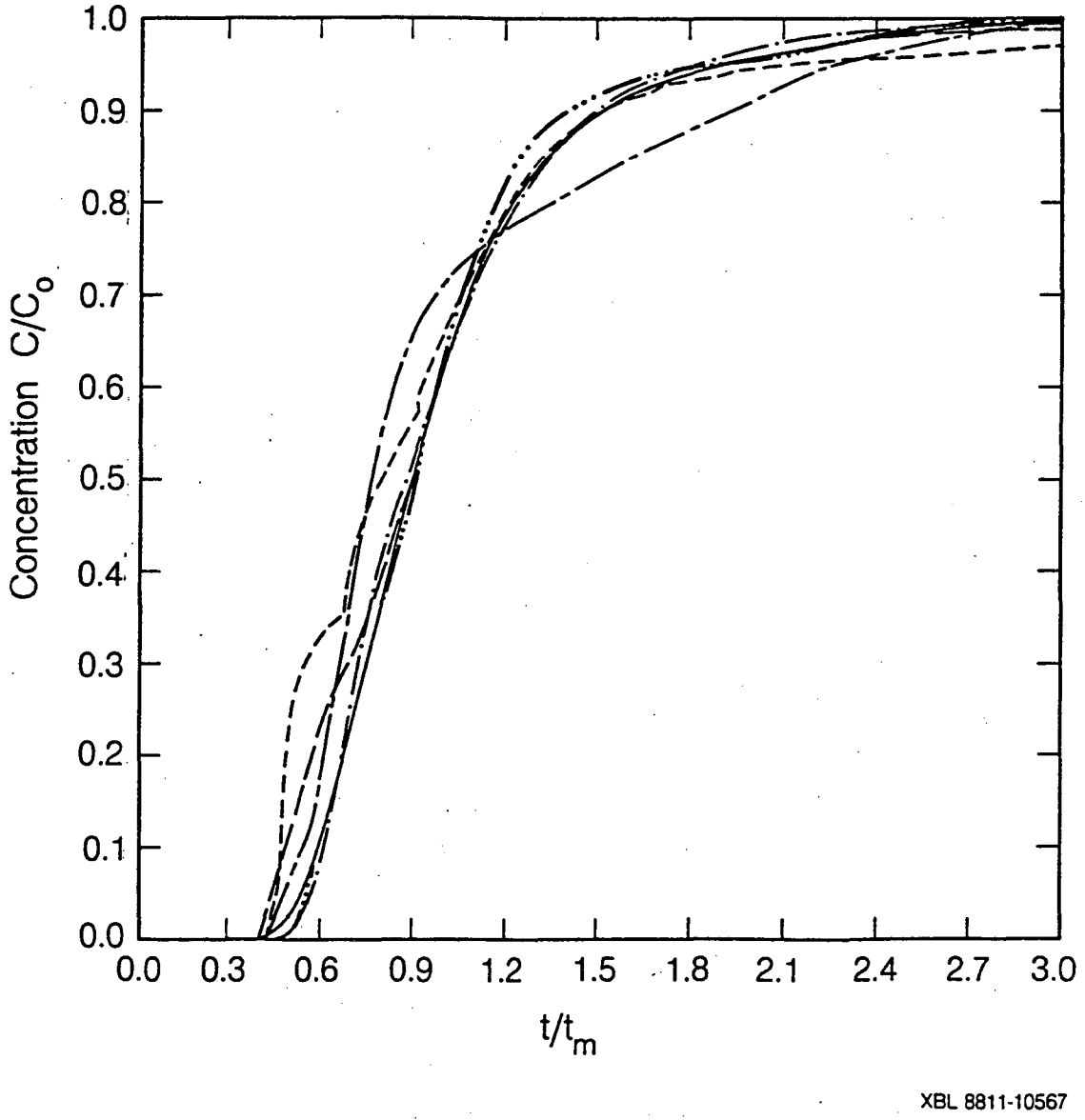

Figure 4. Tracer breakthrough curves for two orthogonal flow directions for each of the three fractures as shown in Figure 1.

Hydrologic Characterization of Faults and Other Potentially Conductive Geologic Features in the Unsaturated Zone

Iraj Javandel and Chao Shan

Abstract

The capability of characterizing near-vertical faults and other potentially highly conductive geologic features in the vicinity of a high-level-waste repository is of great importance in site characterization of underground waste-isolation projects. The possibility of using transient air pressure data at depth (resulting from surface barometric pressure fluctuations) for characterizing these features in the unsaturated zone are investigated. Analytical solutions for calculating the pressure response of such systems are presented. Solutions are given for two types of barometric pressure fluctuations, step function and sinusoidal.

Introduction

The capability of characterizing near-vertical faults and other potentially highly conductive geologic features in the vicinity of a high-level-waste repository is of great importance in underground waste-isolation site characterization projects. The existence of such features near a repository may provide a short travel time flow path from the disturbed zone to the accessible environment.

Measurement of air pressure changes at depth due to atmospheric pressure fluctuations have been used before to estimate the permeability of geologic strata .[1] In those studies the assumption was made that no open borehole, fractures, or other

geologic structures exist that would provide preferred flow paths for air movement. When a conductive fault cuts through layers of geologic materials with lower permeability, points located in the fault zone will experience pressure variations faster and more pronounced than points in the rock mass located at the same elevation. It is desirable to obtain a solution that allows the calculation of pressure response due to the atmospheric pressure variations in a multilayer geologic system with a cross-cutting highly-conductive fault. As a first step, we have developed a series of analytical solutions to calculate the propagation of atmospheric pressure changes in a single-layer system that is intersected by a vertical fault or other planar conductive features. Comparison of pneumatic pressure variations between the fault zone and the surrounding rock mass could provide a means for estimating the permeability of the fault zone.

In this paper we shall present two of these new analytical solutions. These solutions, though limited in application for multilayered geologic systems, could be used for verification of numerical codes that could then be extended to multilayered media.

Mathematical Models

Let us consider a single horizontal geologic layer that is cut by a vertical fault zone with a thickness of $2b'$, as shown in Figure 1. We would like to derive solutions to calculate air pressure changes due to atmospheric pressure fluctuations, as a function of time and position within the system.

The medium is extensive both horizontally and vertically such that mathematically it could be assumed to be infinite in both directions. Since the mid-plane of the fault zone is a symmetry plane, only half of the system will be considered in the analysis. A Cartesian coordinate system is selected such that its origin is at the intersection of the ground surface with the contact plane between the fault and the rock mass. The x-axis is horizontal and perpendicular to the rock-fault zone interface, and the z-axis is oriented vertically downwards.

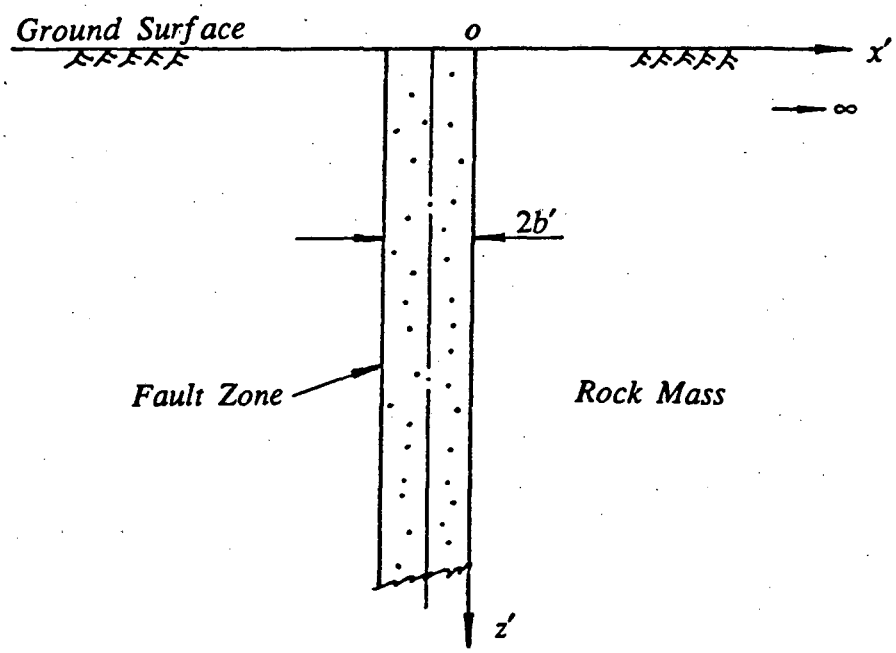

Figure 1. Schematic cross section of the fault zone and surrounding rocks.

The partial differential equations governing the isothermal flow of air in the unsaturated porous media may be written as[1] :

$$\frac{\partial^2\phi'^2}{\partial x'^2} + \frac{\partial^2\phi'^2}{\partial z'^2} = \frac{\mu_a n_a}{k'\bar{p}} \cdot \frac{\partial\phi'^2}{\partial t'} \tag{1}$$

where

$\phi' = \frac{p}{\rho_a g} - z'$ = pneumatic head, L;

$\bar{p}$ = mean pressure of the system, M/LT^2;

μ_a = viscosity of air, M/LT;

n_a = interconnected air-filled porosity at the prevailing moisture content;

k' = air permeability of the medium at the prevailing moisture content, L^2;

t' = time, T.

Assumptions inherent in the development of Equation (1) are as follows:

- the medium is homogeneous and isotropic with a constant moisture content;
- air permeability of the medium is large enough that the Klinkenberg[2] effect is negligible;
- absolute pressure is small enough that the ideal gas laws apply;
- the change in pressure with depth has a negligible effect on air density.

In this study, similar to that of Weeks[1], we have assumed that pneumatic head varies only slightly from its mean value. Under this condition, Equation (1) may be approximated to the following form that is linear with respect to ϕ'.

$$\frac{\partial^2\phi'}{\partial x'^2} + \frac{\partial^2\phi'}{\partial z'^2} = \frac{1}{\alpha'} \cdot \frac{\partial\phi'}{\partial t'} \tag{2}$$

where $\alpha' = \frac{k'\overline{p}}{\mu_a n_a}$ is pneumatic diffusivity.

Furthermore, flow in the fault zone is assumed to be one-dimensional in the vertical direction, while the flux crossing the fault-rock interface is treated as a sink term in the governing equation for the fault zone. The impact of some of the above assumptions will be discussed later in the paper. Based on the above assumptions, the mathematical model for the system under consideration may be written as follows.

In a dimensionless form, the partial differential equations for the intact rock and the fault zone are:

$$\frac{\partial^2\phi_r}{\partial x^2} + \frac{\partial^2\phi_r}{\partial z^2} = \frac{1}{\alpha}\cdot\frac{\partial\phi_r}{\partial t} \tag{3}$$

$$\frac{\partial^2\phi_f}{\partial z^2} + k\left(\frac{\partial\phi_r}{\partial x}\right)_{x=0} = \frac{\partial\phi_f}{\partial t} \tag{4}$$

where the subscripts 'r' and 'f' refer to the intact rock and the fault zone, respectively. Dimensionless terms applied in the formulations are defined as,

$$x = \frac{x'}{b'} \qquad z = \frac{z'}{b'} \qquad k = \frac{k'_r}{k'_f}$$

$$\phi = \frac{\phi' - \phi'_0}{\phi'_b - \phi'_0} \qquad t = \frac{\alpha'_f t'}{b'^2} \qquad \alpha = \frac{\alpha'_r}{\alpha'_f} \tag{5}$$

where ϕ'_0 and ϕ'_b refer to the initial and upper boundary values of the pneumatic head.

As noted above, two types of boundary conditions have been considered for the variation of atmospheric pressure at the ground surface. Type one refers to a step function, and type two to sinusoidal pressure variations.

Except for the boundary conditions at the ground surface, the rest of boundary and initial conditions for both cases are the same, and may be written as,

$$\phi_r(x, z, 0) = \phi_f(z, 0) = 0 \tag{6}$$

$$\phi_r(\infty, z, t) = \text{finite} \tag{7}$$

$$\phi_r(x, \infty, t) = \phi_f(\infty, t) = 0 \tag{8}$$

$$\phi_r(0, z, t) = \phi_f(z, t) \tag{9}$$

Type one boundary condition at the ground surface in non-dimensional form translates to:

$$\phi_r(x, 0, t) = \phi_f(0, t) = 1 \tag{10}$$

For the second type boundary condition, to simplify derivations, one may introduce a new definition for dimensionless pneumatic head as,

$$\phi = \frac{\phi' - \phi'_0}{\phi'_a} \tag{11}$$

where ϕ'_a is the amplitude of pressure head variation, $p_a/\rho_a g$. Now, the second type boundary condition may be written as,

$$\phi_r(x, 0, t) = \phi_f(0, t) = \sin(\omega t) \tag{12}$$

Solutions

Case 1: Step function atmospheric pressure variation.

Using Laplace transformation with respect to t and Fourier sine transformation with respect to z consecutively, Equations (3) and (4) may be reduced to:

$$\frac{d^2 w_r}{dx^2} - \left(\frac{s}{\alpha} + \rho^2\right) w_r = -\frac{\rho}{s} \tag{13}$$

$$w_f = \frac{1}{s+\rho^2}\left[\frac{\rho}{s} + k\left(\frac{dw_r}{dx}\right)_{x=0}\right] \tag{14}$$

where s and ρ are Laplace and Fourier sine transform parameters, respectively.

The initial condition (6) and boundary conditions (8) and (10) have already been used in deriving Equations (13) and (14).

Equation (13) is a nonhomogeneous second order-ordinary differential equation whose solution satisfying boundary condition (7) may be written as:

$$w_r = C_1 e^{-\sqrt{\frac{s}{\alpha}+\rho^2}\,x} + \frac{\rho}{s(\frac{s}{\alpha}+\rho^2)} \tag{15}$$

where,

$$C_1 = (\frac{1}{\alpha}-1)\cdot\frac{\rho}{(\frac{s}{\alpha}+\rho^2)(s+\rho^2+k\sqrt{\frac{s}{\alpha}+\rho^2})} \tag{16}$$

In evaluating constant C_1 boundary condition (9) has been used. Inversion of Equation (15) to the (x, z, t) domain is lengthy and beyond the scope of this paper. The final solution, however, is given by:

$$\phi_r(x,z,t) = \mathrm{erfc}(\frac{z}{2\sqrt{\alpha t}}) + \mathrm{erfc}(\frac{x}{2\sqrt{\alpha t}}) - \mathrm{erfc}(\frac{z}{2\sqrt{\alpha t}})\,\mathrm{erfc}(\frac{x}{2\sqrt{\alpha t}})$$

$$+ \frac{2(1-\alpha)}{\pi}\int_0^\infty [f_1(x,\rho,t)+f_2(x,\rho,t)]\sin(\rho z)d\rho \tag{17}$$

where,

$$f_1(x,\rho,t) = \frac{\rho}{B_1(B_1-B_2)} e^{\frac{x}{\sqrt{\alpha}}B_1+B_1^2 t-\alpha\rho^2 t}\,\mathrm{erfc}(B_1\sqrt{t}+\frac{x}{2\sqrt{\alpha t}}) \tag{18}$$

$$f_2(x,\rho,t) = \frac{-\rho}{B_2(B_1-B_2)} e^{\frac{x}{\sqrt{\alpha}}B_2+B_2^2 t-\alpha\rho^2 t}\,\mathrm{erfc}(B_2\sqrt{t}+\frac{x}{2\sqrt{\alpha t}}) \tag{19}$$

in which B_1 and B_2 are defined as:

$$B_1, B_2 = \frac{1}{2}[\frac{k}{\sqrt{\alpha}} \pm \sqrt{\Delta}] \qquad (\Delta>0) \tag{20}$$

$$B_1, B_2 = \frac{1}{2}[\ \frac{k}{\sqrt{\alpha}} \pm i\sqrt{-\Delta}\ ] \qquad (\Delta<0) \tag{21}$$

with the determinant Δ defined by:

$$\Delta = \frac{k^2}{\alpha} + 4(\alpha-1)\rho^2 \tag{22}$$

The expression for the pneumatic head in the fault zone may be readily obtained from Equation (17) by simply setting x = 0.

Case 2: Sinusoidal atmospheric pressure variation.

The procedure for solving the mathematical model with sinusoidal atmospheric pressure variation is very similar to the one described above and the expression for pneumatic head in the rock mass becomes:

$$\phi_r(x,z,t) = e^{-z\sqrt{\frac{\omega}{2\alpha}}}\sin(\omega t - z\sqrt{\frac{\omega}{2\alpha}}) + \frac{2\alpha\omega}{\pi}\int_0^\infty \frac{ue^{-\alpha u^2 t}\sin(uz)}{\omega^2+\alpha^2u^4}du$$

$$+\omega\int_0^t \mathrm{erfc}(\frac{x}{2\sqrt{\alpha t}})[\,1-\mathrm{erfc}(\frac{z}{2\sqrt{\alpha t}})\,]\cos[\omega(t-\tau)]d\tau$$

$$+\frac{2(1-\alpha)\omega}{\pi}\int_0^\infty \sin(\rho z)d\rho\int_0^t [f_1(x,\rho,\tau)+f_2(x,\rho,\tau)]\cos[\omega(t-\tau)]d\tau \tag{23}$$

Results and Discussion

In this section, we shall first present some of the results obtained from the evaluation of the solutions presented above. A discussion on the impact of various assumptions used in the setup of the mathematical model will then follow.

Figures 2 through 5 present some of the results obtained for case 1, i.e., step function atmospheric pressure variation. Figure 2 shows variation of dimensionless pneumatic head versus dimensionless depth within the fault zone for three values of dimensionless time and for a fixed ratio of rock to fault-zone permeability k=0.02.

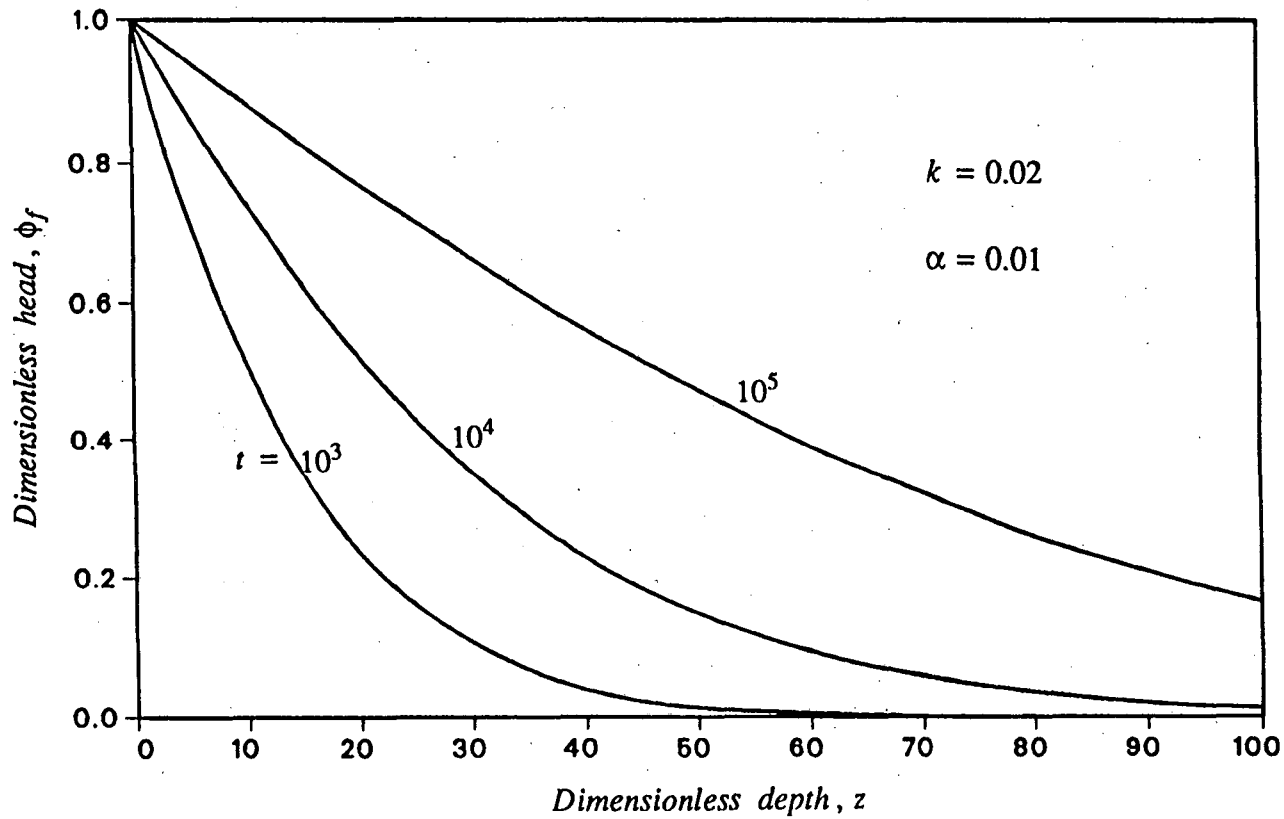

Figure 2. Variation of dimensionless pneumatic head versus dimensionless depth within the fault zone for three values of dimensionless time.

Figure 3 presents the variation of dimensionless pneumatic head with dimensionless distance from the fault-rock interface at a dimensionless depth of 20 and three values of dimensionless time. Corresponding values of pneumatic head in the absence of the fault are also shown. Figure 4 shows a snap shot of pneumatic head changes with distance away from the fault zone-rock contact for different levels of permeability ratio at the dimensionless depth of z = 20. To examine the effect of permeability contrast between the fault zone and the surrounding rocks, we have intentionally kept $\bar{p}/\mu_a n_a$ the same in the two regions.

As is apparent in Figure 4, at a given time, the gradient of pressure variation in the direction perpendicular to the fault increases with the permeability contrast (i.e., decreasing k). The gradient, however, decreases with time as shown in Figure 3. A close look at Figure 4 indicates that the curve for k=0.001 intersects the ones for k=0.01 and 0.1 at small values of x. This means that at that particular time some points in the vicinity of the fault zone may show higher pressure changes for k=0.001 than for larger k values. This can be explained by noting that under two conditions pressure changes at the fault-rock contact (i.e., x=0) are identical: (1) When permeability of the fault zone and the surrounding rock are equal and (2) when the permeability of the surrounding rock is zero. In both cases there is no flow across the contact. Case 1 corresponds to k=1 and case 2 to k=0. When permeability of the surrounding rock is less than that of the fault-zone, since there is flux from the fault toward the rock, at a given depth and time pressure change in the fault zone becomes smaller. That is why ϕ_r at x=0 and for k=0.1 and 0.01 become smaller than for k=1. However, when the rock permeability becomes very small, flux into the rock mass tends to diminish and as a result pressure change in the fault increases again.

Figure 5 presents time variation of pneumatic head within the fault zone and at points away from the fault at the depth corresponding to z=20 and permeability ratio k= 0.01.

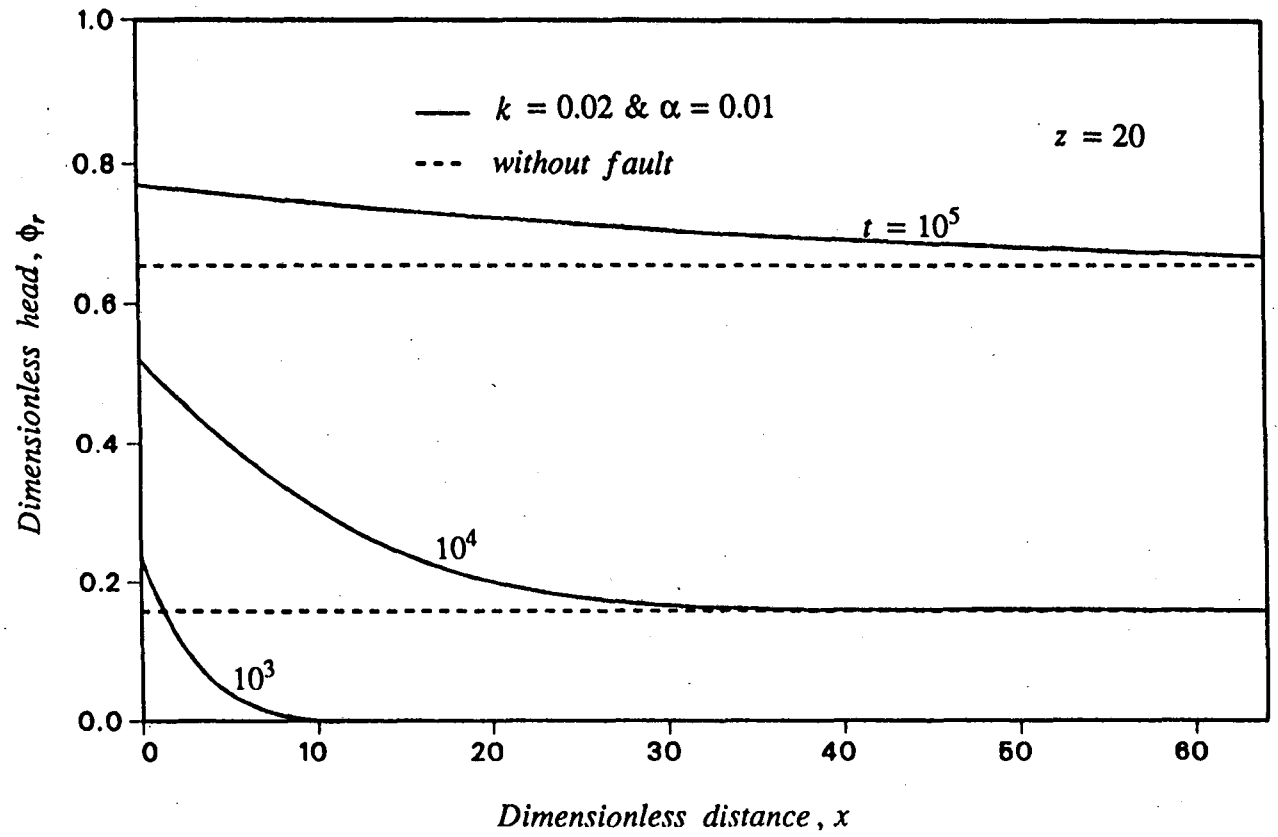

Figure 3. Variation of dimensionless pneumatic head versus dimensionless distance from the fault zone at z=20, for three values of dimensionless time.

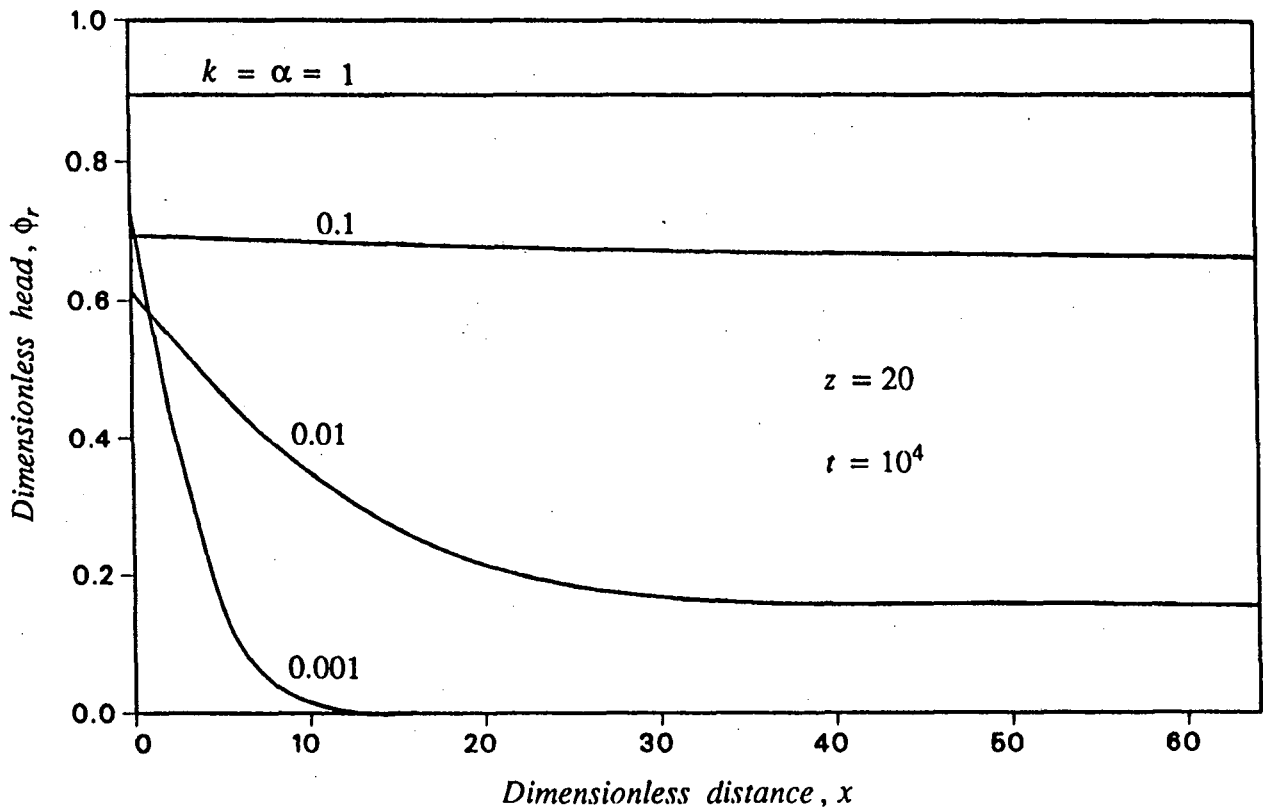

Figure 4. Effect of permeability contrast on dimensionless pneumatic head.

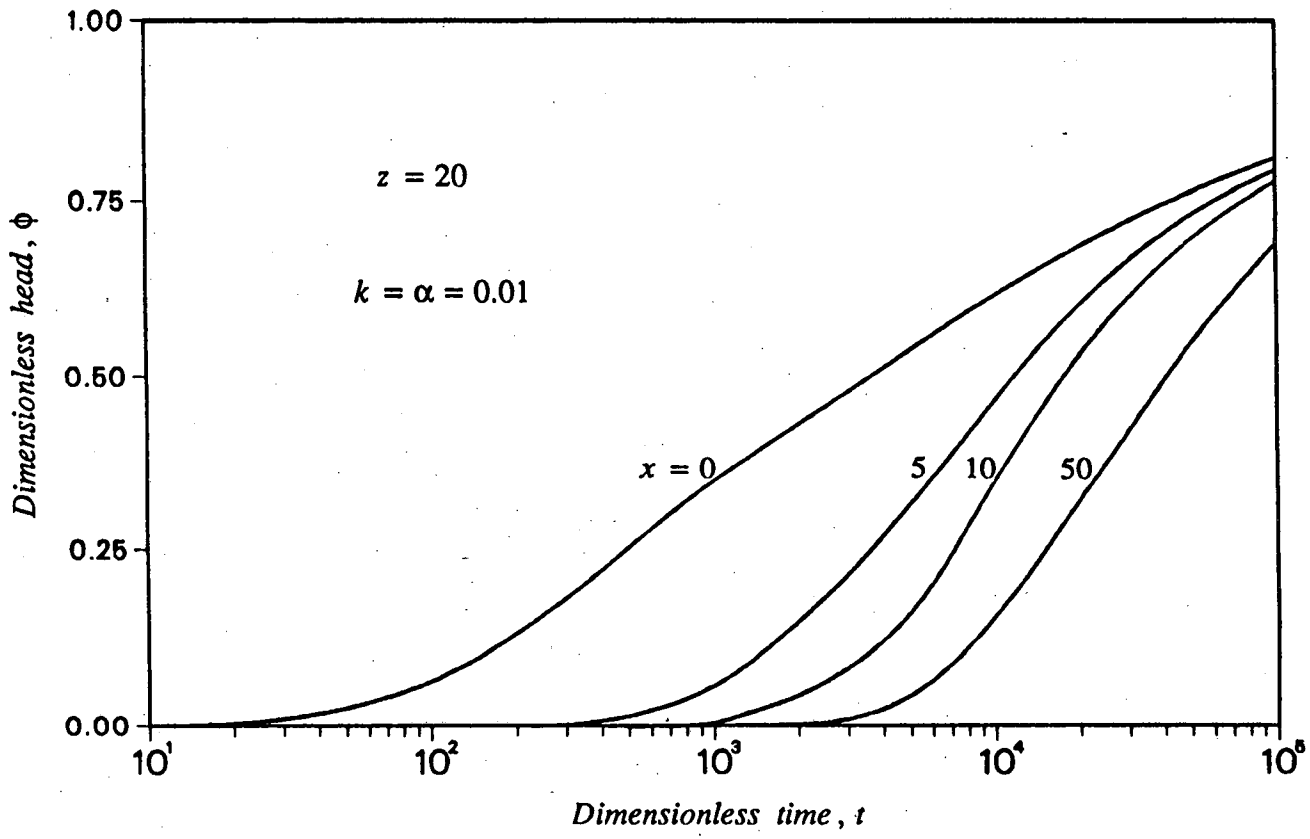

Figure 5. Dimensionless pneumatic head versus dimensionless time within the fault zone and three points within the rock mass, at the same depth, for z=20, and k=α=0.01.

Figures 6 and 7 present results obtained from evaluation of the solution for case 2 (sinusoidal atmospheric pressure variation). Figure 6 shows time variation of pneumatic head in the fault zone at three different depths for a permeability ratio k= 0.02. Figure 7A illustrates time variation of pneumatic head within the fault zone and at other points away from the fault at the same depth, for z=20 and k=0.01. Figure 7B shows results for the same set of parameters except for permeability ratio of 0.005. Note that when the permeability of the rock adjacent to the fault zone is significantly less than that of the fault zone, points located away from the fault will experience a smaller amplitude of pressure changes. The farther the points the smaller are the amplitudes. Furthermore, there is also a phase lag in the observed pressure changes. The farther the point from the fault the larger is the lag in the observed pressure changes. Such phenomenon seems to magnify when the permeability contrast increases (i.e., k decreases).

Examination of Figures 4, 5 and 7 reveals that when the contrast between permeability of the fault zone and surrounding rock is significant, the spatial pressure variations in the vicinity of the fault zone could be large enough to lend itself to be measured by conventional instruments. Therefore, air pressure data from isolated intervals in horizontal or inclined boreholes drilled through a fault zone may be analyzed to obtain the permeability ratio between the fault zone and surrounding rocks.

In the setup of the mathematical model certain assumptions were used. The validity and impact of these assumptions on the solutions will be discussed next.

To substitute Equation (2) for (1) we assumed that pneumatic head varies only slightly from its mean value. According to Weeks[1], pneumatic head changes are generally less than one percent of its mean value and thus the magnitude of error due to this assumption is within half a percent. Another assumption used in our development was that the effect of moisture content variation with time on the air permeability of the medium was insignificant. Although moisture content may change with time, such

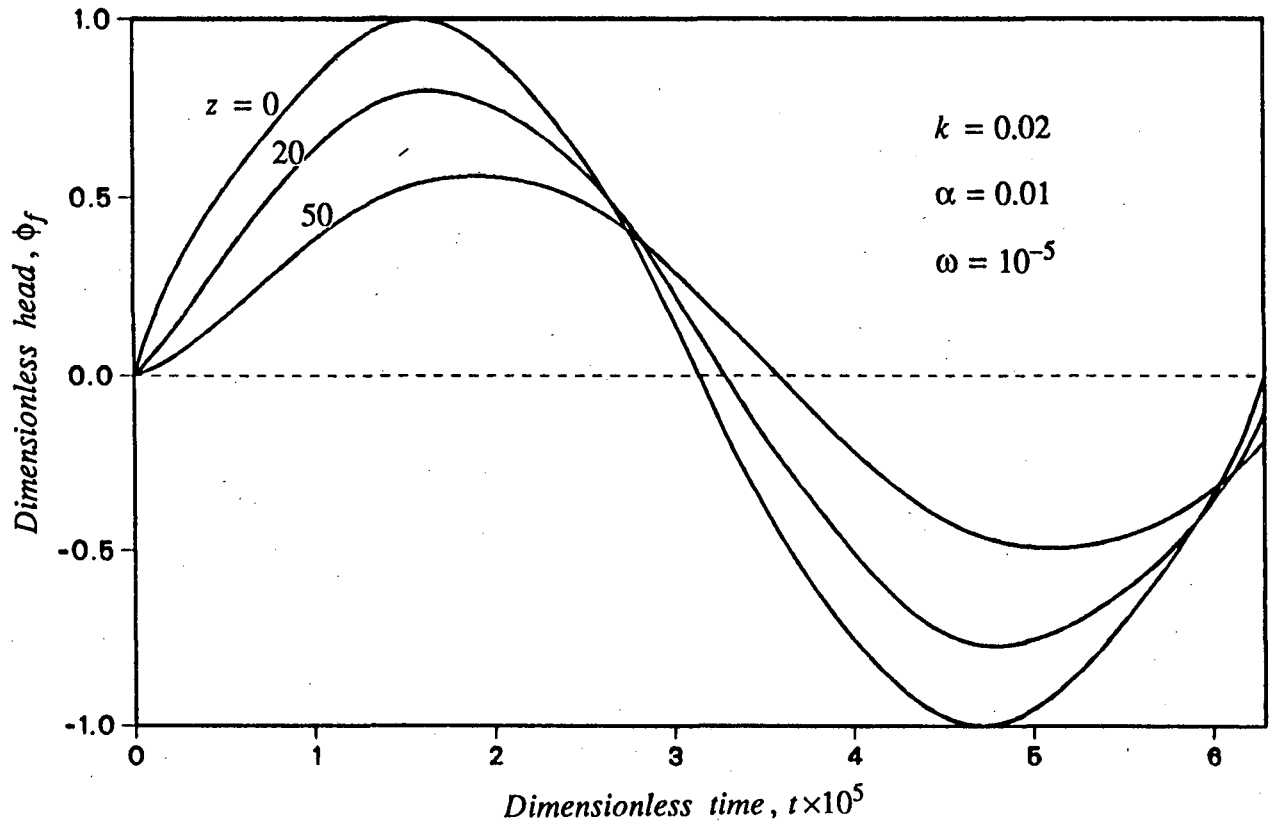

Figure 6. Dimensionless head versus dimensionless time in the fault zone at three different dimensionless depths.

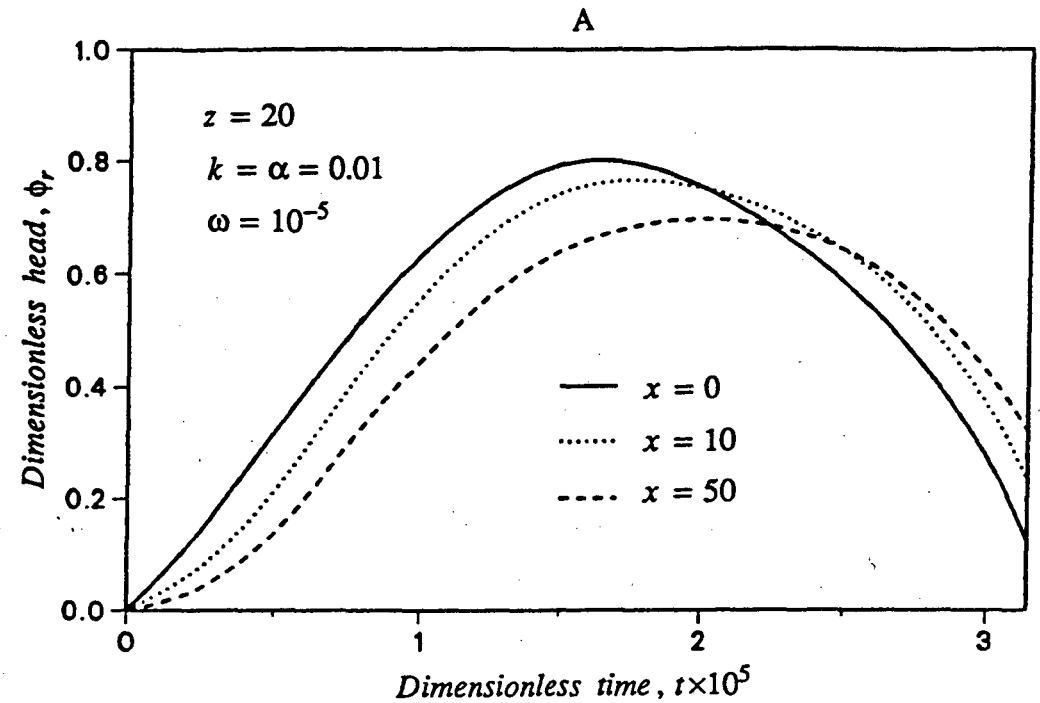

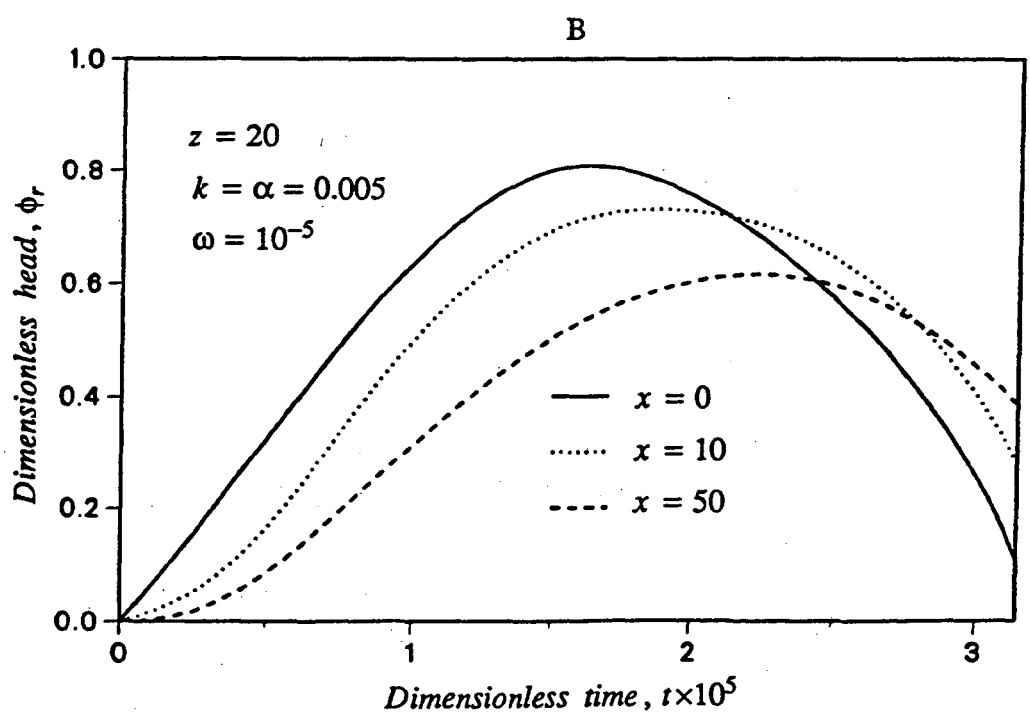

Figure 7. Time variation of pneumatic head within the fault zone and two other points away from the fault at the same depth, for z=20, and (A) k=α=0.01, (B) k=α=0.005.

variations over the short time period needed for completing the test are not expected to be significant. In fact, measurement of pressure at various times, leading to different effective air permeabilities may be used to determine time variation of moisture content.

Furthermore, we assumed that flow in the fault zone is one dimensional, meaning that the equipotentials are essentially horizontal. The impact of this assumption on the accuracy of the solution may be evaluated with the help of numerical simulation. To do that, we first compared the results of our new analytical solutions with those obtained from the simulation of a well established code called TRUMP .[3] Figure 8 shows the comparison of results obtained by using these two approaches for a set of dimensionless parameters indicated in the figure and for both types of boundary conditions. As is clear from this figure, the agreement of two approaches is quite satisfactory. Then, TRUMP was used to simulate a model that allowed 2-D flow in both fault zone and the surrounding rocks. The results of this study revealed that except for very small values of time and small permeability contrasts, the assumption of one dimensional flow in the fault zone is quite reasonable. Figure 9 shows the distribution of pneumatic head in the system at a given depth and two values of time for a very small permeability contrast (k=0.5). It is clear that except for very small values of time and even for small permeability contrasts, equipotentials in the fault zone are essentially horizontal.

Conclusion

A series of new analytical solutions has been developed that predict transient pressure changes in the vicinity of major potentially highly conductive geologic features at depth due to barometric pressure variations at the land surface. Two of these solutions, one using step function and the other sinusoidal barometric pressure changes were presented. The results obtained from the evaluation of these solutions

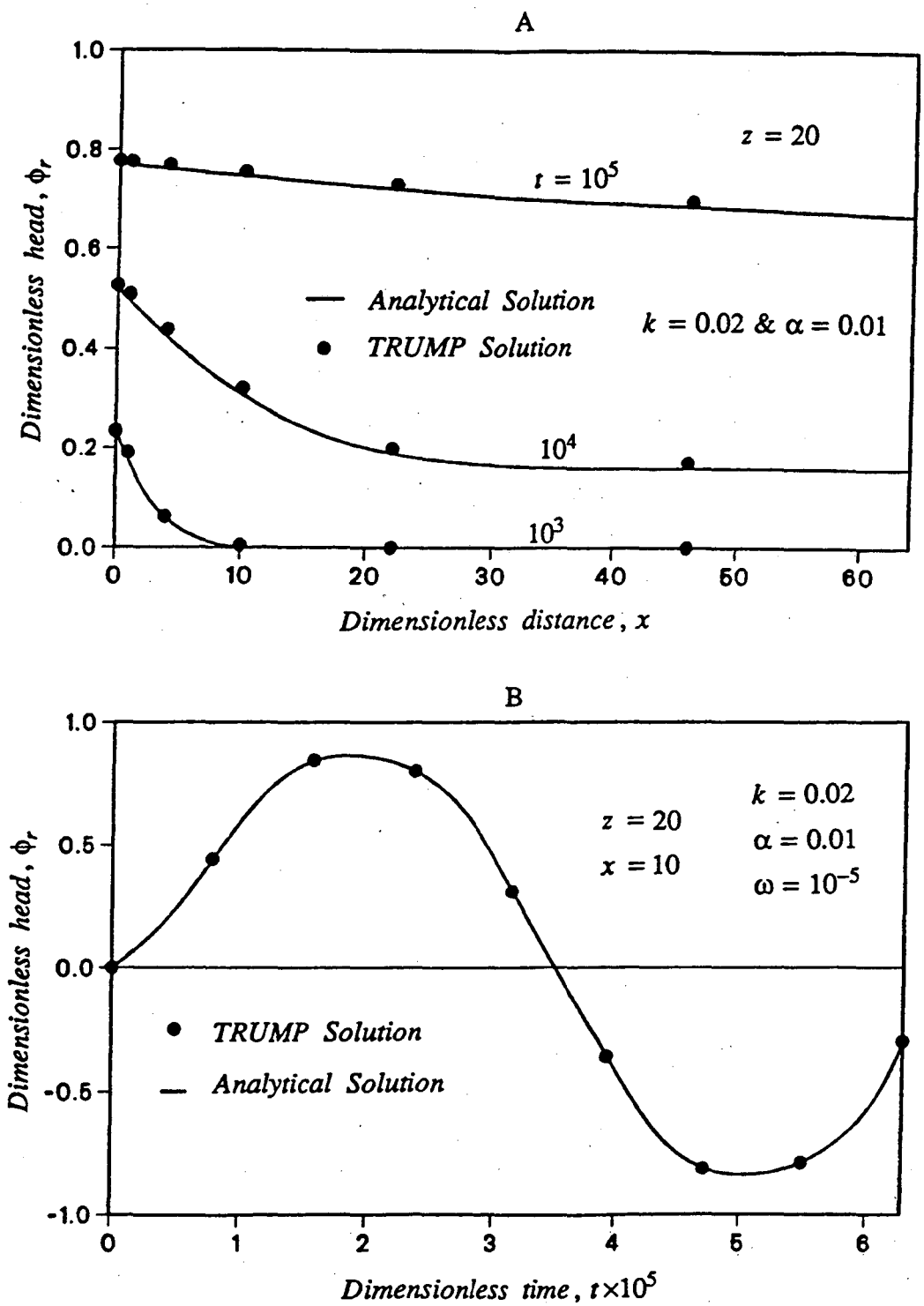

Figure 8. Comparison of present analytical solutions with numerical code *TRUMP*[3], (A) step function solution, and (B) sinusoidal solution.

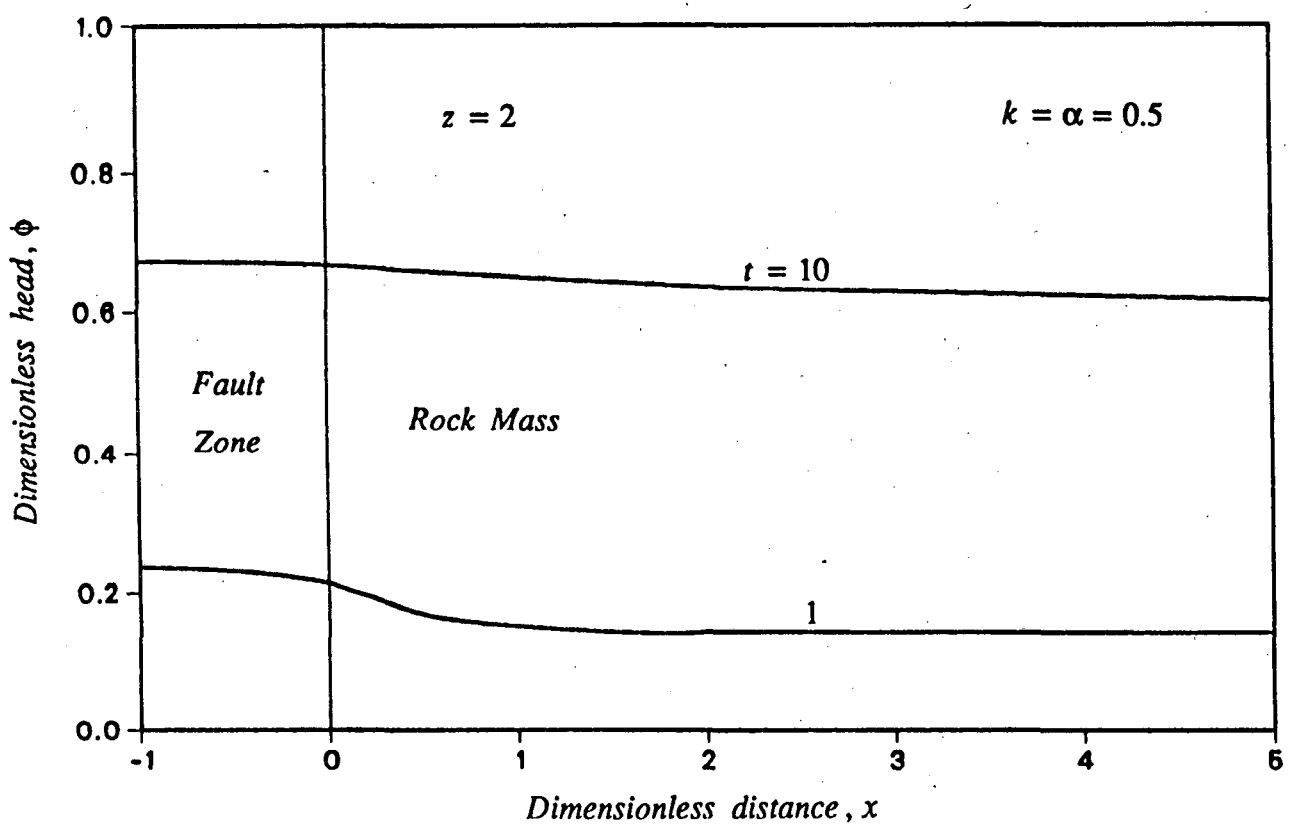

Figure 9. Distribution of pneumatic head in the system at z=2 and two values of time.

suggest that when the permeability of such features is at least an order of magnitude larger than that of the surrounding rocks, measurement of air pressure changes within isolated intervals in a horizontal or inclined borehole drilled through the fault zone may be used to estimate the ratio of permeability between the two media.

Acknowledgments

The authors thank Marcelo Lippmann and Chin Fu Tsang for reviewing this manuscript. This work was sponsored by the Director, Office of Civilian Radioactive Waste Management, Office of Facilities Siting and Development, Siting and Facilities Technology Division of the U.S. Department of Energy Under Contract No. DE-AC03-76SF00098.

References

1. Weeks, E. P., Field Determination of Vertical Permeability to Air in the Unsaturated Zone, *U.S. Geological Survey Professional Paper 1051,* (1978).
2. Klinkenberg, L. J., The Permeability of Porous Media to Liquids and Gases, *Amer Petroleum Inst. Drilling and Production Practice,* (1941).
3. Edwards, A. L., TRUMP: A Computer Program for Transient and Steady State Temperature Distribution in Multidimensional Systems, *UCRL-14754, Lawrence Livermore Laboratory,* (1972).

Mass Transport with Chemical Reactions in a Varying Thermal Field

C. L. Carnahan

Summary

A computer program, THCVP, simulates coupling between advective/diffusive solute transport and chemical reactions, coupling of the reactions to heat transport, and feedback from precipitation/dissolution reactions to fluid flow. A simple simulation of transport of dissolved silicic acid along a gradient of temperature shows how precipitation of quartz at low temperatures can drastically reduce advective transport of all solution components including trace contaminants.

Introduction

The work described here is part of a task to theoretically and numerically analyze effects of varying thermal fields on transport of radionuclides and groundwater components in fracture filling materials in the near field at Yucca Mountain, and to numerically estimate the sensitivity of the effects to magnitudes of controlling parameters.

Computer programs that simulate the movement of reactive chemical species in subsurface waters are important tools for the assessment of performance and, ultimately, safety of nuclear waste repositories. An aspect of geochemical behavior that can have important consequences in performance assessment is the effect of a variable thermal field on (1) the movement of major solution components and dissolved waste radionuclides and (2) the stabilities of minerals exposed to the changing thermohydrochemical environment. Variable thermal fields can arise in the near vicinity of nuclear waste canisters and from mixing of fluids having different temperatures. Such fields imposed on previously stable or

metastable fracture minerals can induce dissolution of existing minerals, transport of dissolved chemical species, and precipitation of new solid phases. Redistribution of materials within fractures by chemical reactions and transport can produce changes of physical properties such as porosity, mass diffusivity, and permeability. Changes of these parameters can affect transport of both radionuclides and major components of subsurface fluids.

Computer programs[1–5] that couple chemical reactions, including precipitation/dissolution, to mass transport processes have not, in general, accounted for the effects of precipitation/dissolution reactions on the transport processes. In particular, changes in the sizes of pores or apertures of fractures caused by precipitation/dissolution reactions accompanying mixing of fluids of different compositions can alter the effective mass diffusivities and permeabilities of porous or fractured materials[6], and these alterations can affect the subsequent movement of dissolved chemicals. Neglect of these alterations not only might produce inaccurate computational results[7], but might also lead to physically unrealizable consequences such as the calculated volume of a precipitate exceeding available pore space.

An examination of calculated permeability changes associated with chemical changes accompanying simulated acidization of sandstone with HCl/HF mixtures has been reported[8]. Calculations of the permeability changes were done separately from the reactive chemical transport simulations; thus, there was not complete coupling between precipitation/dissolution reactions and fluid flow in the simulations.

Reaction-transport feedback in advecting systems with chemical disequilibrium has been described and has been simulated by the computer program REACTRANS to demonstrate the origins of patterned states ("geochemical self-organization") in rocks[9,10]. These calculations did not consider the effects of varying thermal fields.

Basis for the Computer Program THCVP

The reactive chemical transport simulator THCVP is an extension of the simulator

THCC[11,12], and is being used to study effects on mass transport of precipitation/dissolution reactions in the presence of varying thermal fields. The THCVP computer program is a thermodynamically based simulator of multicomponent, reactive chemical transport using the direct method of solution. The program simulates transport of reactive chemical species by advection and hydrodynamic dispersion or mass diffusion in one-dimensional linear or cylindrically symmetric geometry. Chemical reactions are assumed to be in a state of local equilibrium. The reactions simulated are complexation, oxidation-reduction, ionization of water, reversible precipitation of solid phases, and ion exchange. Chemical reactions are described by mass action relations among thermodynamic activities of participating species. The THCVP program has the capability to simulate systems with temporally and spatially variable fields of temperature.

In a system with fluid-filled porosity ϵ_f, N_p reactive solid phases, and nonsorbed aqueous-phase species consisting of N_b basis species (the smallest set of species needed to define the chemical system in the aqueous phase) and N_c complexes, the conservation equation for the mass of a component i is

$$\frac{\partial}{\partial t}\left(\epsilon_f W_i + \sum_{k=1}^{N_p} \nu_{ik} P_k\right) = \nabla \cdot \left[\left(\epsilon_f D_d + aq\right) \nabla W_i - qW_i\right], \quad i = 1, \ldots, N_b, \tag{1}$$

where t is time, D_d is the diffusion coefficient in the fluid phase, a is the dispersivity, q is the volumetric flux of fluid (Darcy flux), P_k is the concentration (referred to unit volume of porous matrix) of a precipitate P_k, and the ν_{ik}'s are the number of moles of basis species B_i per mole of solid P_k. W_i is the total concentration (referred to unit volume of the fluid phase) of component i and is defined by

$$W_i = B_i + \sum_{j=1}^{N_c} \nu_{ij} C_j, \quad i = 1, \ldots, N_b, \tag{2}$$

where B_i, $i = 1, \ldots, N_b$, is the concentration of the basis species B_i containing component i and ν_{ij} is the number of moles of B_i per mole of complex C_j, $j = 1, \ldots, N_c$, having

concentration C_j. C_j is formed by reactions among basis species, thus:

$$\nu_{lj}\mathrm{B}_l^{z_l} + \nu_{mj}\mathrm{B}_m^{z_m} + \ldots = \mathrm{C}_j^{\nu_{lj}z_l + \nu_{mj}z_m + \ldots},$$

where the z_i are signed ionic charges of the basis species. The concentration of complex C_j is given by the mass action relation,

$$C_j = \frac{K_{cj}}{\gamma_j} \prod_{l=1}^{N_b} (\gamma_l B_l)^{\nu_{lj}}, \quad j = 1, \ldots, N_c, \tag{3}$$

where K_{cj} is the temperature-dependent thermodynamic equilibrium constant for formation of complex C_j and the γ's are activity coefficients.

In the numerical formulation of THCVP, equations (2) and (3) are substituted into equation (1). The resulting set of N_b partial differential equations is transcribed into N_b finite-difference equations, using central differencing in space and the Crank-Nicolson method to obtain second-order accuracy in time. The set of unknowns consists of B_i, $i = 1, \ldots, N_b$, and P_k, $k = 1, \ldots, N_p$, at each finite-difference node. Residue equations for the basis species are formed by algebraically summing all terms in the finite-difference forms of the transport equations. The finite-difference analogs of equation (1) provide N_b residue equations at each node; the remaining N_p residue equations are provided by the solubility products for the reactive solids.

A reactive solid P_k dissolves to form its constituent basis species, thus:

$$\mathrm{P}_k = \nu_{lk}\mathrm{B}_l^{z_l} + \nu_{mk}\mathrm{B}_m^{z_m} + \ldots.$$

The activity product, Q_{sk}, for this reaction is given by

$$Q_{sk} = \prod_{l=1}^{N_b} (\gamma_l B_l)^{\nu_{lk}}. \tag{4}$$

If the the basis species formed by dissolution of solid P_k are in chemical equilibrium with the solid, then the activity product, Q_{sk}, is equal to the thermodynamic solubility

product, K_{sk}. Values of K_{sk} at different temperatures are calculated using tabulated thermodynamic functions[13]. Residue equations for the solids are formed by an algorithm that provides a residue equation for each solid at each node and eliminates the need to alter the number of unknowns at nodes where solids have precipitated or dissolved.

The residues ($N_b + N_p$ at each node) are reduced to "zero" (a small positive number fixed by specifying an error tolerance at input) iteratively by computing corrections to current values of the unknowns using the Newton-Raphson method[14]. Elements of the Jacobian matrix required by this method are computed from analytical expressions. The system of equations to be solved for the corrections has block tridiagonal form and is solved by use of a published software routine[15].

Temperature variations during transport and reaction of chemical components are simulated by numerical solution of a heat-transport equation within THCVP. Three kinds of thermal variations can be simulated: (1) mixing of advecting fluids having different temperatures, (2) diffusion of heat from a constant-temperature boundary, and (3) a constant linear gradient of temperature between two boundaries.

Coupling between Chemical Reactions and Porosity

Equation (1) accounts for changes of porosity, ϵ_f, and fluid flow velocity, q, as well as changes of chemical concentrations. The fluid-filled porosity ϵ_f is not a primary unknown because it is determined by the P_k, $k = 1, \ldots, N_p$. In the iterative Newton-Raphson solution scheme, new values of ϵ_f are calculated from values of the P_k's at the end of each iteration. A conservation equation can be written for a unit volume of porous medium:

$$\epsilon_m + \epsilon_p + \epsilon_f = 1, \tag{5}$$

where ϵ_m is the volume fraction of unreactive solid (constant), ϵ_p is the volume fraction of reactive solids, and ϵ_f is the volume fraction of fluid phase. ϵ_p is calculated from the

current concentrations of reactive solids by

$$\epsilon_p = \sum_{k=1}^{N_p} P_k \overline{V}_k, \tag{6}$$

where $\overline{V}_k$ is the molar volume of reactive solid k and is assumed constant. It follows from equation (5) that

$$\Delta\epsilon_f = -\Delta\epsilon_p. \tag{7}$$

To simulate constant porosity in a system with precipitation/dissolution reactions, all $\overline{V}_k$'s are given input values of zero.

Coupling between Porosity and Fluid Flow

The fluid flux, q, is calculated from Darcy's law:

$$q = -K_f(\epsilon_f)\nabla h, \tag{8}$$

where $K_f(\epsilon_f)$ is the local hydraulic conductivity, a function of porosity, and ∇h is the local hydraulic gradient. A number of empirical relations are available to relate local values of K_f to ϵ_f; currently, THCVP uses a relation similar to the Kozeny-Carmen equation:

$$K_f = C_f \frac{\epsilon_f^3}{(1-\epsilon_f)^2}, \tag{9}$$

where C_f is a constant.

The computer program THCVP assumes a constant hydraulic head drop, h_t, across a finite one-dimensional domain divided into $n-1$ segments by n nodes. Associated with the k-th node ($k = 1, \ldots, n$) and adjacent segment is the current value of porosity, $\epsilon_{f,k}$, and the current value of hydraulic conductivity, $K_{f,k}$, from equation (9). Because there are no sources or sinks of fluid flow in the domain, the Darcy flux, q, at any time must be

constant throughout the spatial domain, aside from geometrical factors. Then it can be shown that at any simulated time level, the Darcy flux in linear geometry is given by

$$q = h_t \left(\sum_{k=1}^{n-1} \frac{x_{k+1} - x_k}{K_{f,k}} \right)^{-1}, \tag{10}$$

where $x_{k+1} - x_k$ is the spatial separation between nodes k and $k+1$, and $x_{k+1} > x_k \geq 0$. Here it is assumed that the hydraulic head drops from h_t at node 1 to zero at node n. Values of hydraulic head, h_k, at intermediate nodes are given by

$$h_k = h_t - q \sum_{i=1}^{k-1} \frac{x_{i+1} - x_i}{K_{f,i}}. \tag{11}$$

In radial coordinates, the geometric variations of q and h_k must be accounted for, and equations (10) and (11) become

$$q = h_t \left(x_1 \sum_{k=1}^{n-1} \frac{x_{k+1} - x_k}{K_{f,k}\, x_{k+1}} \right)^{-1}, \tag{12}$$

and

$$h_k = h_t - x_1\, q \sum_{i=1}^{k-1} \frac{x_{i+1} - x_i}{K_{f,i}\, x_{k+1}}, \tag{13}$$

where $x_{k+1} > x_k > 0$.

Example Simulation

A simple chemical reaction, the precipitation of quartz from saturated solution of silicic acid, illustrates the effect of varying temperature on porosity, hydraulic conductivity, and fluid flow. A constant temperature gradient is imposed on a finite spatial domain, the temperature varying from 90 °C at $x = 0$ to 50 °C at $x = 1$ m. The domain has initial porosity, ϵ_f, of 0.05 and is saturated with silicic acid at the local temperature. The

variation with temperature of the equilibrium constant, K_{SP}, for the reaction,

$$SiO_2(\text{quartz}) + 2H_2O(l) = Si(OH)_4(aq)$$

is given by[13]

$$\log K_{SP} = 1.881 - \frac{1560}{T} - 2.028 \times 10^{-3}T, \tag{14}$$

where T is the absolute temperature in kelvins. The molar volume of quartz is 0.0227 dm^3/mole[16]. The constant C_f in equation (9) is taken to be 0.045 m/s, corresponding to a fracture hydraulic conductivity of 10^{-4} m/s[17] at a porosity of 0.12[18]. At the simulated initial porosity of 0.05, the initial hydraulic conductivity is then 6.2×10^{-6} m/s. (The fracture porosity was reduced from 0.12 to 0.05 in these simulations to reduce computing time.) A constant hydraulic head gradient of unity is imposed on the system, the head dropping from 1 m at $x = 0$ to zero at $x = 1$ m. Under the influence of the head gradient, fluid saturated with silicic acid at 90 °C enters the domain at $x = 0$ and is advected in the direction of increasing x. Due to decreasing temperature and the decreasing solubility of silicic acid, quartz is deposited in the region near $x = 0$; the "concentrations" (moles of quartz per dm^3 of matrix) of deposited solid are shown in Fig. 1 as functions of time for nodes located at $x = 0$ and $x = 0.05$ m. Fig. 2 shows values of porosity at the same two nodes. The deposited solid concentration rises to a steady-state value of about 2.2 mole/dm^3 at time 2.7×10^7 s, while the porosity drops to about 0.0004 at this time. Fig. 3 shows the Darcy flux with time, and is plotted semilogarithmically to emphasize the sudden decrease of fluid flow near 2.5×10^7 s and the non-zero steady-state value of about 6.7×10^{-11} m/s, a decrease of about five orders of magnitude from the initial value. Finally, Fig. 4 shows spatial profiles of hydraulic head at various times, indicating the effect of accumulation of solid quartz near the fluid inlet.

Conclusion

The computer program THCVP provides a capability to simulate coupling and feedback among processes of saturated fluid flow, transport of reactive solutes, and chemical reactions under conditions of varying temperature. A simple simulation shows the significant effect on advective fluid flow of mobilization and subsequent precipitation of quartz from silicic acid solution. Reduction of flow by mineralization involving major solution components can result in decreased migration rates of trace contaminants as well as major components.

Acknowledgment

This work was sponsored by the Director, Office of Civilian Radioactive Waste Management, Office of Facilities Siting and Development, Siting and Facilities Technology Division of the U. S. Department of Energy under Contract No. DE-AC03-76SF00098.

References

1. D. B. Grove and W. W. Wood, "Prediction and Field Verification of Subsurface-Water Quality Changes During Artificial Recharge, Lubbock, Texas", *Ground Water, 17*, 250 (1979).
2. C. W. Miller and L. V. Benson, "Simulation of Solute Transport in a Chemically Reactive Heterogeneous System: Model Development and Application", *Water Resour. Res., 19*, 381 (1983).
3. M. P. Walsh, S. L. Bryant, R. S. Schechter, and L. W. Lake, "Precipitation and Dissolution of Solids Attending Flow through Porous Media", *Am. Inst. Chem. Eng. J., 30*, 317 (1984).
4. S. L. Bryant, R. S. Schechter, and L. W. Lake, "Interactions of Precipitation/Dissolution Waves and Ion Exchange in Flow Through Permeable Media", *Am. Inst. Chem. Eng. J., 32*, 751 (1986).
5. C. L. Carnahan, "Simulation of Chemically Reactive Solute Transport under Conditions of Changing Temperature", in C.-F. Tsang, ed., *Coupled Processes Associated with Nuclear Waste Repositories.* Academic Press, Orlando FL (1987), p. 249.
6. P. A. Witherspoon, J. S. Y. Wang, K. Jwai, and J. E. Gale, "Validity of Cubic Law for Fluid Flow in a Deformable Rock Fracture", *Water Resour. Res., 16*, 1016 (1980).

7. F. J. Pearson, Jr., "Research Needs for Coupling Geochemical and Flow Models for Nuclear Waste Isolation", in "Workshop on Fundamental Geochemistry Needs for Nuclear Waste Isolation", *US DOE CONF8406134*, U. S. Dept. of Energy (1985), p. 175.

8. M. P. Walsh, L. W. Lake, and R. S. Schechter, "A Description of Chemical Precipitation Mechanisms and Their Role in Formation Damage During Stimulation by Hydrofluoric Acid", *J. Pet. Tech., September 1982*, 2097.

9. P. Ortoleva, E. Merino, C. Moore, and J. Chadam, "Geochemical Self-Organization I: Reaction-Transport Feedback and Modeling Approach", *Amer. J. Sci., 287*, 979 (1987).

10. P. Ortoleva, J. Chadam, E. Merino, and A. Sen, "Geochemical Self-Organization II: The Reactive-Infiltration Instability", *Amer. J. Sci., 287*, 1008 (1987).

11. C. L. Carnahan, "Simulation of Uranium Transport with Variable Temperature and Oxidation Potential: The Computer Program THCC", in J. K. Bates and W. B. Seefeldt, eds., *Scientific Basis for Nuclear Waste Management X.* Materials Research Society, Pittsburgh PA (1987), p. 713.

12. C. L. Carnahan, "Simulation of Effects of Redox and Precipitation on Diffusion of Uranium Solution Species in Backfill", in M. J. Apted and R. E. Westerman, eds., *Scientific Basis for Nuclear Waste Management XI.* Materials Research Society, Pittsburgh PA (1988), p. 293.

13. S. L. Phillips, F. V. Hale, L. F. Silvester, and M. Siegel, "Thermodynamic Tables for Nuclear Waste Isolation", *LBL-22860 Vol. 1*, Lawrence Berkeley Laboratory (1988).

14. B. Carnahan, H. A. Luther, and J. O. Wilkes, *Applied Numerical Methods.* John Wiley and Sons, New York (1969), p. 319.

15. A. C. Hindmarsh, "Solution of Block-Tridiagonal Systems of Linear Algebraic Equations", *UCID-30150*, Lawrence Livermore National Laboratory (1977).

16. R. A. Robie, P. M. Bethke, and K. M. Beardsley, "Selected X-ray Crystallographic Data, Molar Volumes, and Densities of Minerals and Related Substances", *Bulletin 1248*, U. S. Geological Survey (1967).

17. J. S. Y. Wang and T. N. Narasimhan, "Hydrologic Mechanisms Governing Fluid Flow in a Partially Saturated, Fractured, Porous Medium", *Water Resour. Res., 21*, 1861 (1985).

18. G. A. Cederberg and L. E. Greenwade, "Preliminary Geochemical/Geophysical Model of Yucca Mountain", in M. J. Apted and R. E. Westerman, eds., *Scientific Basis for Nuclear Waste Management XI.* Materials Research Society, Pittsburgh PA (1988), p. 331.

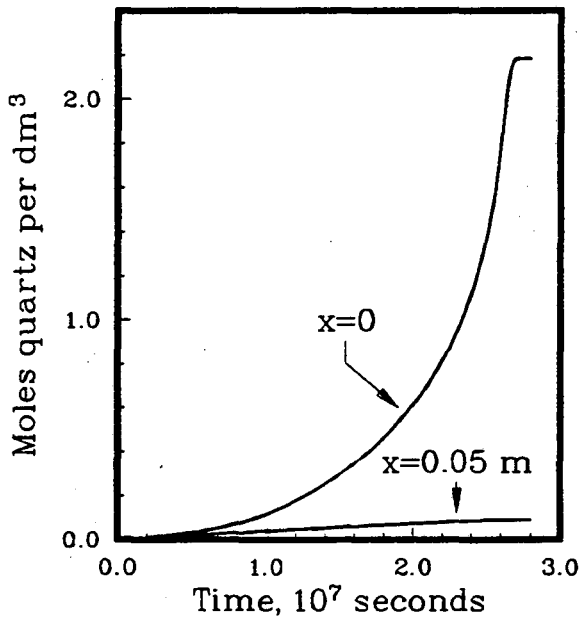

Figure 1. Moles of quartz precipitated per dm^3 of matrix vs. time at x=0 and x=0.05 meter.

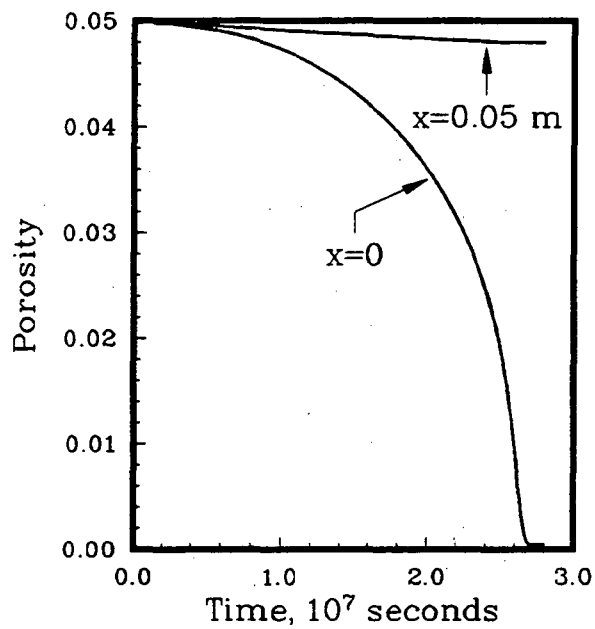

Figure 2. Porosity vs. time at x=0 and x=0.05 meter.

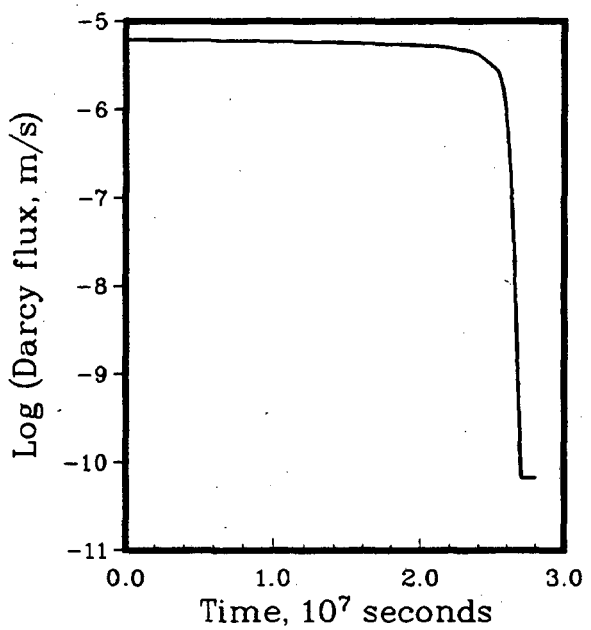

Figure 3. Areal flow rate (Darcy flux) of water vs. time.

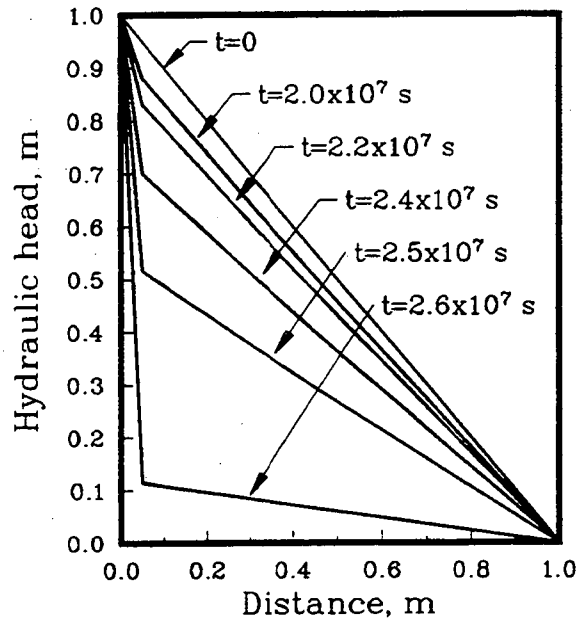

Figure 4. Hydraulic head vs. distance for various simulated times.

Seismic Characterization of Fracture Properties

L. R. Myer, L. J. Pyrak-Nolte, D. Hopkins and N. G. W. Cook

Introduction

A critical component of site characterization and performance assessment involves the demonstration that any fluid flow which might reach the accessible environment is within acceptable limits. Various methods of analyzing flow in fractured rocks have been proposed, but choice of an appropriate method and its application to a specific site probably requires some knowledge of the spacing and length (or density) of fractures, their orientation and their hydraulic conductivity. Some of this information will undoubtedly come from geologic mapping on surface and in excavations, as well as from boreholes, cores and laboratory tests. However, it will be necessary to detect and characterize fractures in the rock mass between these direct observations. The remote detection and characterization of fractures by geophysical methods is, therefore, of considerable interest in connection with geologic repositories.

The purpose of this paper is to show that there is a relationship, both empirical and theoretical, between the measured seismic response, the mechanical stiffness (also referred to as specific stiffness) of fractures and their hydraulic conductivity. Laboratory measurements of the mechanical stiffness, hydraulic conductivity and seismic properties of natural fractures are summarized. A theoretical model for the amplitude and group time delay for compressional and shear waves transmitted across a single fracture is presented. Predictions based on this model are compared with laboratory measurements. Finally, the results for a single fracture are extended to multiple parallel fractures.

Experimental Procedures

Mechanical, hydrologic and seismic tests were performed on three samples (referred to as E30, E32 and E35) of quartz monzonite measuring 52 mm in diameter by 77 mm in height. Each sample contained a single natural fracture orthogonal to the long axis of the core. Apparatus for the experiments is illustrated schematically in Figure 1. Fracture displacement (or closure) measurements were made using Linear Variable Differential Transformers (LVDT's) such that deformations within the fracture were isolated from deformation of the intact rock. Measurements were made at axial stresses up to 85 MPa.

The quadrant flow technique was used to measure the hydraulic conductivities of each of the fractures. In this technique the fracture was assembled and its intersection with the circumference of the specimen was sealed along two diametrically opposed quadrants. Fluid flow then occurred between inlet and outlet ports attached to the two remaining quadrants. A pressure difference of 0.4 MPa was applied and flow measurements were made as the axial stress was increased in steps to a maximum of effective stress of 85 MPa.

Seismic measurements were performed on the specimens using the pulse transmission method. The specimens were uniaxially compressed between transducers containing compressional (P-) and shear (S-) wave piezoelectric elements having a resonant frequency of about 1 MHz. Waveforms were collected for eight axial stress levels from 1.4 MPa to 85 MPa under dry and saturated conditions. Reference signals were obtained under the same conditions for three intact specimens cut from the same core in close proximity to the fractured specimens.

Results of Mechanical, Hydrologic and Seismic Measurements

Results of the displacement measurements on the three fractured specimens are shown in Figure 2. Fracture displacement increased rapidly up to a stress of about 10 MPa and more gradually up to 85 MPa. The nonlinear behavior is similar to what others have observed. Repeated cycling showed that, while displacements were non-linear, they were also elastic. The fracture displacement curves are a direct consequence of the spatial geometry of asperities of contact, their dimensions and height distribution. Measured displacements are not only due to deformation of the asperities, but also to the interaction between asperities and the deformation of the half-spaces defining the fracture. Under low loads there are few asperities of contact and so closure of large numbers of voids results in rapidly increasing displacements. As voids close the contact area must increase leading to increased stiffness and more gradual increase in displacements at higher stresses. Displacement did not reach zero even at 85 MPa, suggesting that numbers of voids must still be open at this stress.

The inverse of the tangent to the displacement vs. stress curves for the fractures is defined as the specific stiffness of the fractures. The specific stiffness of each fracture increased with increasing load. Corresponding to the differences in the amount of displacement for the three samples, fracture E32 exhibited the highest specific stiffness, E30 intermediate and E35 the lowest specific stiffness.

Results of the flow experiments are summarized in Figure 3 which is a plot of the log of fracture displacement (closure) versus log of flow per unit head drop. The quantity d_{max} represents the fracture closure which would result if stress were increased until all voids in the fracture closed. As shown in the figure, flow decreases much more rapidly with closure than would be predicted by the "cubic law" assuming the fracture were modelled by smooth parallel plates. At high stresses it is seen that flow approaches a constant value (for E30 and E32) while the fractures continued to close. The changes in flow rate with fracture closure (increasing stress) are also

related to the changes in void geometry in the fracture. It has been shown that flow through a fracture is dominated by the restrictions which exist along the connected pathways. The geometry of these flow paths is related to the spatial correlation of the apertures of the void spaces and adjacent areas of contact. At high stresses the results from E30 and E32 imply that the principal impediment to fluid flow must be comprised of tubes or orifices with equidimensional cross-sections that do not diminish significantly with increasing stress.

Because of the dependence of both fluid flow and mechanical displacement (closure) on void geometry in a fracture, it seems reasonable to expect a correlation between the stiffness of a fracture and its hydraulic conductivity. A rank correlation was observed in that E32 with the highest specific stiffness had the lowest hydraulic conductivity while E35, with the lowest stiffness, had the highest hydraulic conductivity.

Typical results of the seismic measurements are presented in Figure 4, which shows amplitude spectra of P-wave pulses for intact and fractured specimens at selected stress levels under dry conditions. The spectra were calculated by performing a Fast Fournier Transform on signals which had been tapered to isolate the initial pulse from subsequent reflections.

As seen in Figure 4 increasing stress resulted in increasing spectral amplitudes for both fractured and intact specimens. However, there are important differences between the spectra for the intact and fractured specimens which reflect the effect of the fractures on the transmitted wave. At low stresses, the spectral amplitudes for the fractured specimens were smaller and peaked at a lower frequency than those for the intact specimens at the same stress level. In addition, as stress increased, the difference between the spectra of the intact and fractured specimens diminished; at 85 MPa for specimens E30 and E32, spectra for the fractured specimens were almost identical to those for the intact specimens.

The differences between results for the fractured and intact specimens are due to the specific stiffness of the fractures. If the specific stiffness of a fracture is very high, which can be the case under high normal stress, the fracture deforms very little in response to the dynamic stress of a propagating wave and therefore the wave is barely affected by the presence of the fracture. Thus, as was seen for specimens E30 and E32, the spectra for intact and fractured specimens were similar at high stress levels. At low stress levels, the specific stiffness of a fracture is lower resulting in appreciable deformation in response to the dynamic stresses. The consequence of this deformation is the reduction in amplitude and shift in frequency seen for the fractured specimens at low stress levels. A theory which quantitatively relates the specific stiffness of a fracture to the amplitude and group time delay of a propagating plane wave is outlined in the next section.

Just as the mechanical displacement measurements show the difference in specific stiffness of the three fractures, so do the seismic measurements. As a result of the high specific stiffness of fracture E32, the fractured specimen transmitted energy almost as well as the intact specimen at a stress of 20 MPa. In comparison, a stress of 85 MPa was required on fracture E30 before the specific stiffness was increased sufficiently to erase the effect of the fracture on the transmitted wave. The least stiff fracture E35 still affected the transmitted wave even at 85 MPa.

Comparison of the seismic and fluid flow results on these three specimens shows there is also a rank correlation between the hydraulic conductivity of fractures and their affect on seismic wave propagation; that is, the fracture which caused the greatest apparent attenuation of the transmitted seismic wave also had the highest hydraulic conductivity while the fracture with the lowest conductivity affected the transmitted wave least. Apparently the reason for this correlation is that the apparent attenuation of the transmitted wave is related to the specific stiffness of the fracture and both specific stiffness and hydraulic conductivity are dependent upon the geometry of the

fracture voids.

The laboratory seismic measurements also revealed a correlation between the amplitude of the wave transmitted across a fracture and its saturation. The results indicated that amplitudes of the transmitted P-wave will, in general, be higher under saturated conditions than under dry conditions. The reason is again related to the specific stiffness of the fracture under saturated and dry conditions. As a P-wave propagates across a saturated fracture the dynamic load will be distributed between the water in the voids and the solid asperities of contact. Thus, compared to dry conditions, the deformation of the fracture would be less, leading to a higher specific stiffness and less apparent attenuation of the P-wave. The degree to which a saturated fracture will be stiffened depends on the area and aperture of the voids. These experiments have addressed only the two extreme conditions, completely dry and completely saturated. Under partially saturated conditions it is expected that, in addition to fracture stiffness, loss mechanisms, such as pumping, would affect the amplitude of the transmitted wave.

Finally, the laboratory measurements revealed that, for all three fractures, at low to intermediate stress, more S-wave energy was transmitted under saturated than dry conditions. Because of the negligible shear stiffness of water these results can not be explained by changes in the specific stiffness of the fracture. We hypothesize, as will be explained in more detail below, that the increase in shear wave transmission is caused by viscous coupling between the two fracture surfaces.

Summary of Seismic Theory

The fracture displacement experimentally measured on the three fractures represented, on average, the deformation which occurred in the specimen in excess of that which occurred in the intact rock. Since it was localized in the plane of the fracture, it can be shown that the fracture displacement constitutes a discontinuity in the

displacement field produced in the specimen by the applied stresses.

To analytically predict the seismic response of a single fracture under dry conditions it is modelled mathematically as a displacement discontinuity, the magnitude of which is inversely proportional to the specific stiffnesses of the fracture. The general solution of the wave equation for arbitrary angles of incidence and materials of different seismic impedance above and below the fracture has been given by others.

For seismic waves normal to a fracture in an elastic isotropic medium, the magnitudes of the reflection coefficient ($R(\omega)$) and transmission coefficient ($T(\omega)$) are given by:

$$|R(\omega)| = \left[\frac{\omega^2}{4(\kappa/z)^2+\omega^2}\right]^{1/2} ; \left[\frac{4(\kappa/z)^2}{4(\kappa/z)^2+\omega^2}\right]^{1/2}, \tag{1}$$

where

ω = circular frequency

z = ρc_p for P-waves or ρc_s for shear waves

c_p = $\sqrt{\lambda+2\mu/\rho}$

c_s = $\sqrt{\mu/\rho}$

λ = Lame's constant

μ = shear modulus

ρ = density

κ = specific normal stiffness for P-waves or specific shear stiffness for S-waves

The magnitude of both the reflection and transmission coefficients are functions of the frequency of the incident wave as well as the ratio of the specific stiffness of the fracture to the seismic impedance of the adjacent rock. For an infinite value of specific stiffness, $|T|\rightarrow 1$, so energy is transmitted as if no fractures were present. For a zero value of specific stiffness, $|R|\rightarrow 1$, so, in this limit, the fracture acts as a free surface.

>From the phase of $T(\omega)$ a group time delay, t_g, can be found, which, for the same conditions as in Eq. (1), is given by:

$$t_{gT} = \frac{2(\kappa/z)}{4(\kappa/z)^2 + \omega^2}, \tag{2}$$

where subscript T refers to transmission. Thus, the theory predicts that a single fracture will slow a wave propagating across it, and the amount it is slowed will depend upon the frequency of the wave and the ratio of its specific stiffness to seismic impedance.

To model shear wave propagation across a saturated fracture, the effect of apparent viscous coupling is accounted for by introducing a velocity discontinuity in addition to a displacement discontinuity. Resulting values of $|R(\omega)|$ and $|T(\omega)|$ for normal incidence are:

$$|R(\omega)| = \left[\frac{\omega^2}{4(\kappa/z)^2 + (\omega/z)^2 (2\eta + z)^2}\right]^{1/2}, \tag{3}$$

$$|T(\omega)| = \left[\frac{4(\kappa/z)^2 + (\omega/z)^2 \eta^2}{4(\kappa/z)^2 + (\omega/z)^2 (2\eta + z)^2}\right]^{1/2},$$

where η = specific viscosity, i.e., the viscosity of the fluid in the fracture divided by the separation between the fracture surfaces. The corresponding group time delay is given by:

$$t_{gT} = \frac{8\gamma^3 - 4\gamma\xi\omega^2 (2\xi + 1)}{[4\gamma^2 + \xi\omega^2 (2\xi + 1)]^2 + (2\omega\gamma)^2}, \tag{4}$$

where $\gamma = \kappa/z$ and $\xi = \eta/z$.

The effect of adding viscosity to a fracture with finite stiffness is to reduce the energy transmitted at low frequencies and increase the energy transmitted at high frequencies. In the absence of stiffness, Eq. (4) shows that the group time delay for shear waves is zero at all frequencies.

An example of a quantitative comparison between theory and experimental results is shown in Figure 5a,b. To obtain the predicted spectra, the experimentally observed spectra for the companion intact rock specimen were multipled by theoretical values of $|T(\omega)|$ given by Eq. (1) for P-waves under dry conditions, and Eq. (2) for S-wave under saturated conditions. Values of specific stiffness and specific viscosity were determined by trial and error to give the "best fit." Good agreement is obtained between observed and predicted results. In Figure 5a the predicted curves based on values of κ, alone, simulate both the increasing spectral amplitudes as the specific stiffness of the fracture increases with stress and the shift toward higher frequencies of the maximum spectral amplitudes. For the S-wave under saturated conditions (Fig. 5b) there was little shift in the frequency of the maximum spectral amplitudes as stress was increased due to the effect of viscous coupling.

Extension to Multiple Fractures

The model for a single fracture has been extended to calculate the anisotropy in group velocities and amplitudes of seismic waves transmitted at oblique angles across multiple parallel fractures. It is assumed that multiple reflections do not contaminate the first arriving pulse and that the specific stiffness of one fracture, and hence its affect on wave propagation, is not a function of the proximity of other fractures.

The validity of the latter assumption was evaluated from measurements in which the spacing between two idealized fractures was varied. The idealized fractures were created by compressing rows of thin, parallel strips (1.0 mm wide by 0.03 mm thick) of lead between steel surfaces as shown in the insert of Figure 6. The effect of the idealized fractures on the amplitude of the transmitted P-wave (wavelength of about 23 mm) can be seen from a comparison of the amplitude spectrum of the transmitted wave with that from a solid steel specimen with a welded joint. The tests were conducted with a strip spacing (2R) of 3.0 mm. The configuration of the idealized

fractures permitted direct calculation of their specific stiffness. Using Eq. (1), the spectrum from the welded joint tests, and the calculated specific stiffness, the predicted spectrum was generated assuming no interaction between fractures. As can be seen there was essentially no affect of interaction until the spacing between the fractures (2.36 mm) was on the order of the spacing between the strips. At this close spacing the deformations of the voids and asperities in one fracture were affected by the presence of voids and asperities in the other fracture.

These experiments show that as long as fractures are not so close as to interact mechanically under an imposed seismic stress, then, to a first order, they can be treated independently in calculating their effect on the propagating wave. Under these circumstances, the magnitude of the transmission coefficient for a wave propagating across a set of parallel fractures is $|T|^N$, where $|T|$ is the value for a single fracture and N is the number of fractures.

The total group time delay under these conditions is given by the sum of the individual group time delays over the length of the travel path. The total group travel time is composed of the travel time through the intact rock between fractures plus the group time delay. For seismic waves normally incident upon a set of plane parallel fractures the effective group velocity, V_{eff}, is given by:

$$V_{eff} = \frac{V\,[1 + (\omega(2\kappa/z))^2]}{1 + (\omega/(2\kappa/z))^2 + (NVZ/2LK)} \tag{5}$$

where V is the intact rock group velocity and L/N is fracture spacing. These relationships, in addition to those for transmitted wave amplitudes, provide a means for using amplitude and velocity data to estimate mechanical stiffness of fractures occurring in the field.

Conclusions

Laboratory measurements of mechanical stiffness, hydraulic conductivity, and seismic amplitudes carried out on the same three natural fractures have demonstrated that a correlation exists between each of these physical properties. Fundamentally all three responses, mechanical, hydrologic and seismic, could be explained based on the spatial distribution of voids and asperities in the fractures and the changes in this distribution due to an applied stress. It was observed that the properties of all three fractures could be ranked according to their mechanical stiffness. Thus the stiffest fracture exhibited the smallest hydraulic conductivity and resulted in the least reduction of seismic amplitudes. The least stiff fracture exhibited the greatest hydraulic conductivity and greatest reduction in seismic amplitudes. The fracture of intermediate stiffness was also intermediate in hydraulic conductivity and seismic response.

By treating a fracture as a displacement discontinuity, quantitative relationships have been developed between the group time delay and amplitudes of the reflected and transmitted waves, the mechanical stiffness of single fractures and the seismic impedance of the intact rock. For saturated conditions additional relationships have been developed between the group time delay and amplitudes of shear waves and the specific viscosity of the fractures. The displacement discontinuity theory has been extended to predict an effective group velocity and amplitudes of waves propagating through multiple parallel fractures. It has been shown that to a first order, fractures can be treated independently until their spacing becomes comparable to the spacing between asperities in the fractures.

Based on laboratory results, the displacement discontinuity theory appears to predict the effects of fractures on the transmission of seismic waves well. The frequency-dependence of the group time delay and of the coefficients of reflection and transmission should enable the specific stiffness and specific viscosity of single fractures and multiple parallel fractures to be determined. It may be further possible to

identify hydraulically conductive features and those which may be saturated.

REFERENCES

Bandis, S. C., Lumsden, A. C. and Barton, N. R., 1983, Fundamentals of Rock Joint Deformation, *International Journal of Rock Mechanics and Mining Science Geomechanics Abstracts,* 20(6), pp. 249-268.

Brown, S. R. and Scholz, C. H., 1985, Closure of Random Elastic Surfaces in Contact, *Journal of Geophysical Research,* 90(B7), pp. 5531-5545.

Hopkins, D. L., Cook, N. G. W. and Myer, L. R., 1987, Fracture Stiffness and Aperture as a Function of Applied Stress and Contact Geometry, Proceedings of 26th U.S. Symposium on Rock Mechanics, pp. 673-680.

Myer, L. R., Hopkins, D. and Cook, N. G. W., 1985, Effects of Contact Area of an Interface on Acoustic Wave Transmission, Proceedings of 26th U.S. Symposium on Rock Mechanics, pp. 549-556.

Pyrak-Nolte, L. J., 1988, Seismic Visibility of Fractures, Ph D. Dissertation, Department of Materials Science and Mineral Engineering, University of California, Berkeley, California.

Pyrak-Nolte, L. J., Cook, N. G. W. and Myer, L. R., 1990, Stratified Percolation Model for Saturated and Unsaturated Flow through Natural Fractures, Proceedings of First Annual International High-Level Radioactive Waste Management Conference, American Nuclear Society.

Pyrak-Nolte, L. J., Myer, L. R. and Cook, N. G. W., 1990, Anisotropy in Seismic Velocities and Amplitudes from Multiple Parallel Fractures, accepted for publication in *Journal of Geophysical Research.*

Pyrak-Nolte, L. J., Myer, L. R., Cook, N. G. W. and Witherspoon, P. A., 1987, Hydraulic and Mechanical Properties of Natural Fractures in Low Permeability Rock, Proceedings of 6th International Congress of Rock Mechanics, Montreal, Vol. I, pp. 225-232.

Pyrak-Nolte, L. J., Cook, N. G. W. and Nolte, D., 1988, Fluid Percolation through Single Fractures, *Geophysical Research Letters,* 15(11), pp. 1247-1250.

Schoenberg, M., 1980, Elastic Wave Behavior Across Linear Slip Interfaces, *Journal of the Acoustical Society of America,* 68(5), pp. 1516-1521.

Swan, L., 1983, Determination of Stiffness and Other Joint Properties from Roughness Measurements, *Rock Mechanics and Rock Engineering, 16(1),* pp. 19-38.

Tsang, Y. W. and Tsang, C. F., 1987, Channel Model of Flow through Fractured Media, *Water Resources,* 23, p. 467.

Yang, G., Cook, N. G. W. and Myer, L. R., 1989, Network Modelling of Flow in Natural Fractures, Proceedings of the 30th U.S. Symposium on Rock Mechanics, pp. 57-64.

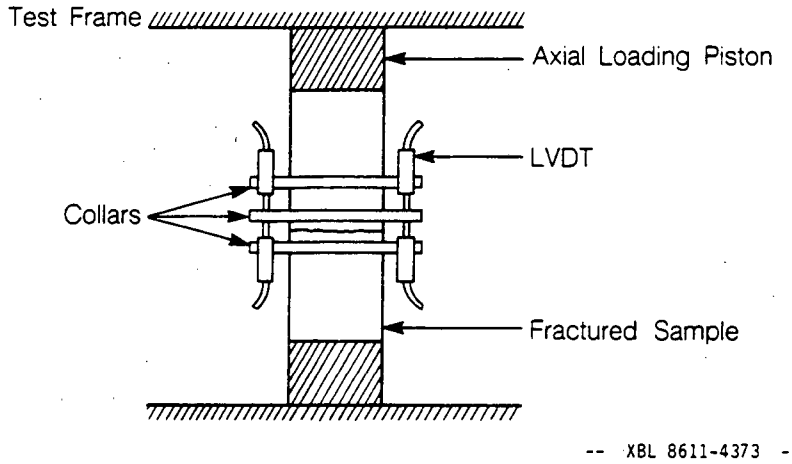

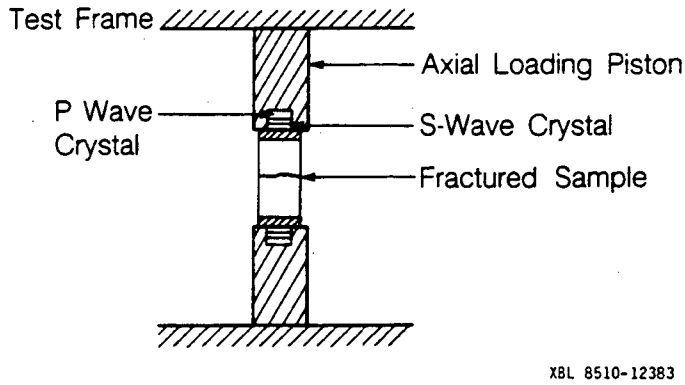

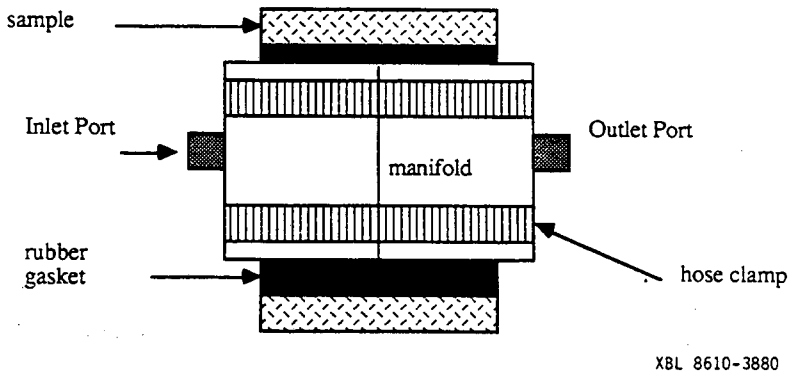

Figure 1. Apparatus for laboratory measurements; top, mechanical displacement; middle, fluid flow; and bottom, seismic measurements.

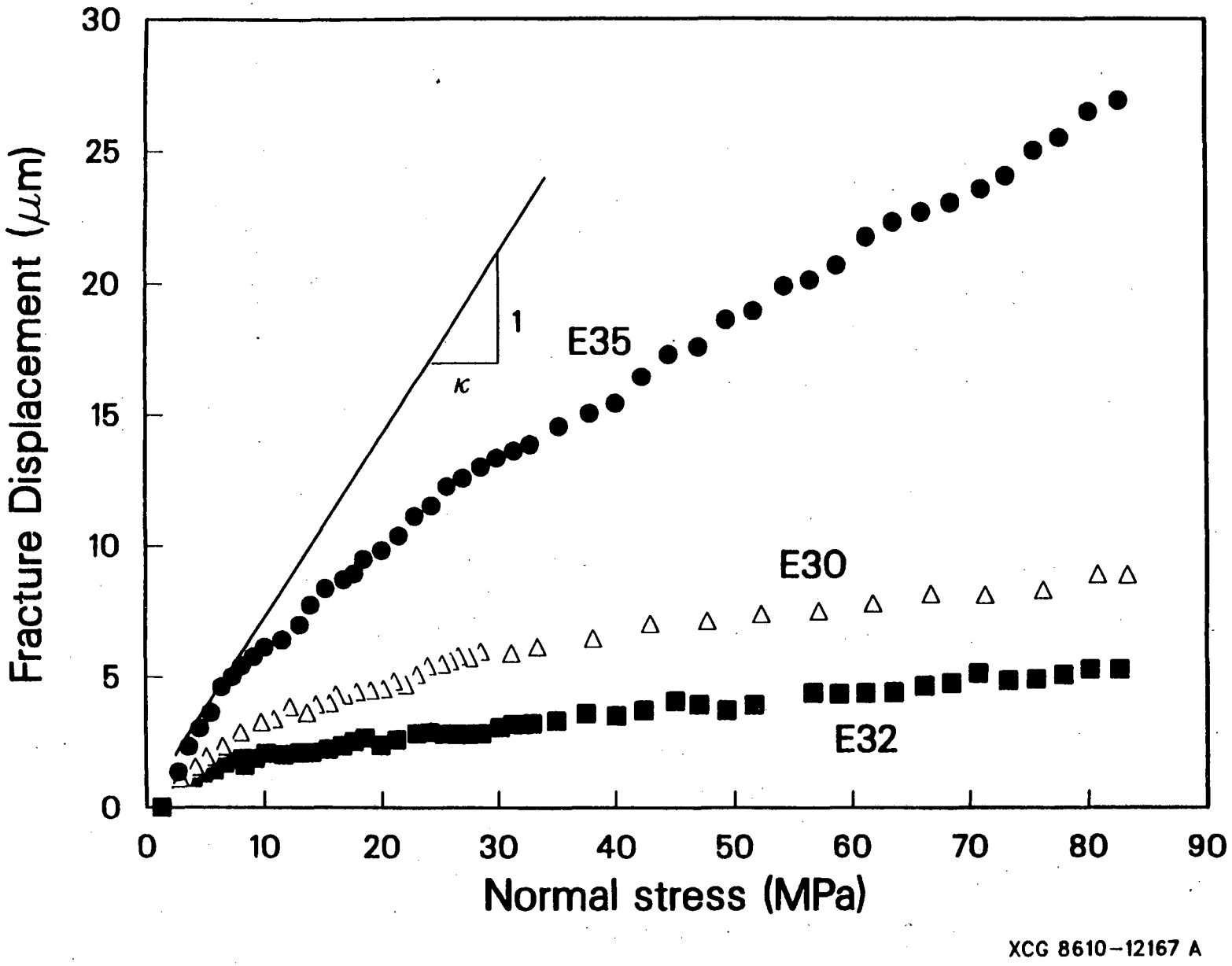

Figure 2. Fracture displacements as a function of applied normal stress for three fractures.

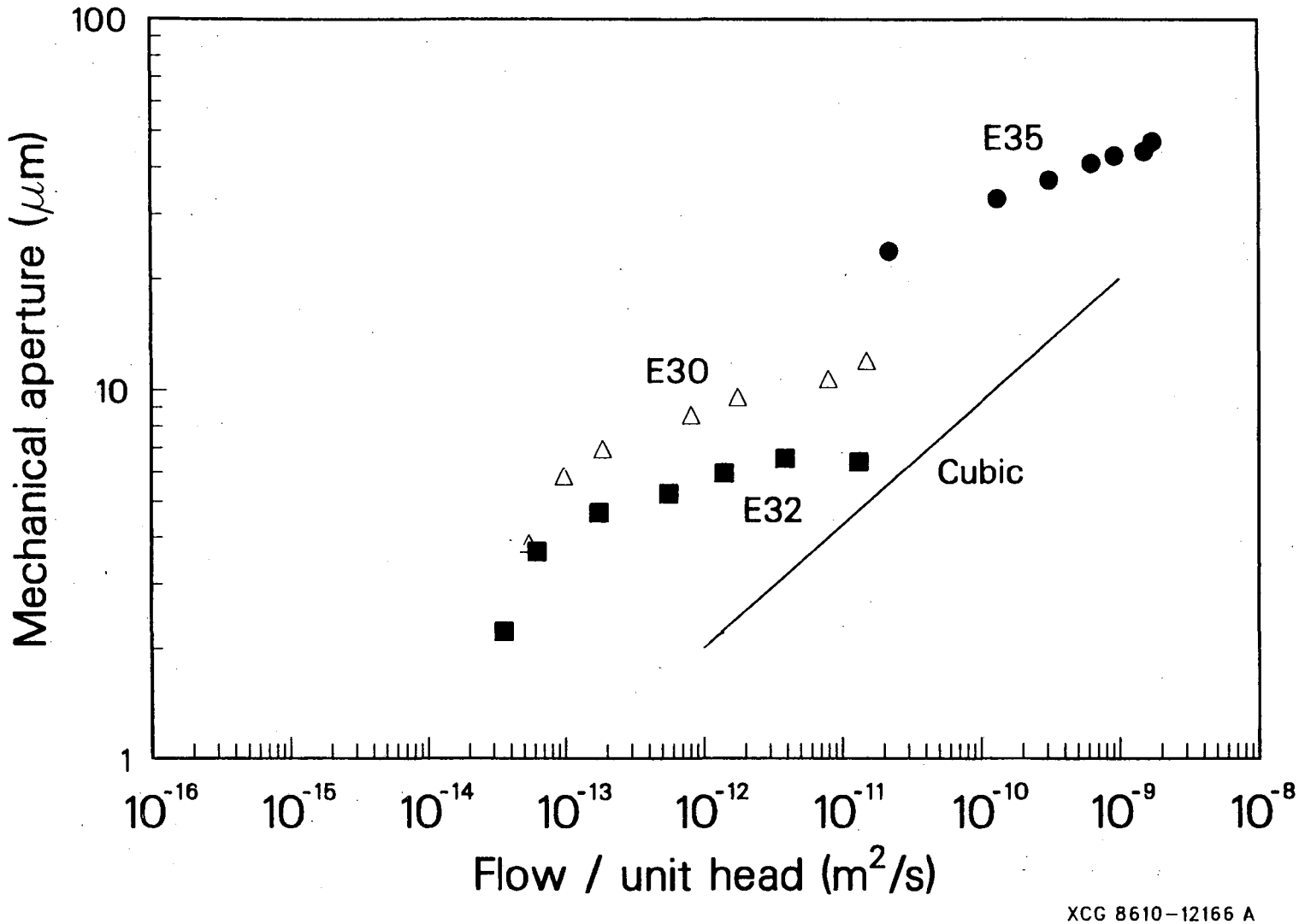

Figure 3. Fracture displacement versus flow per unit head drop for three fractures.

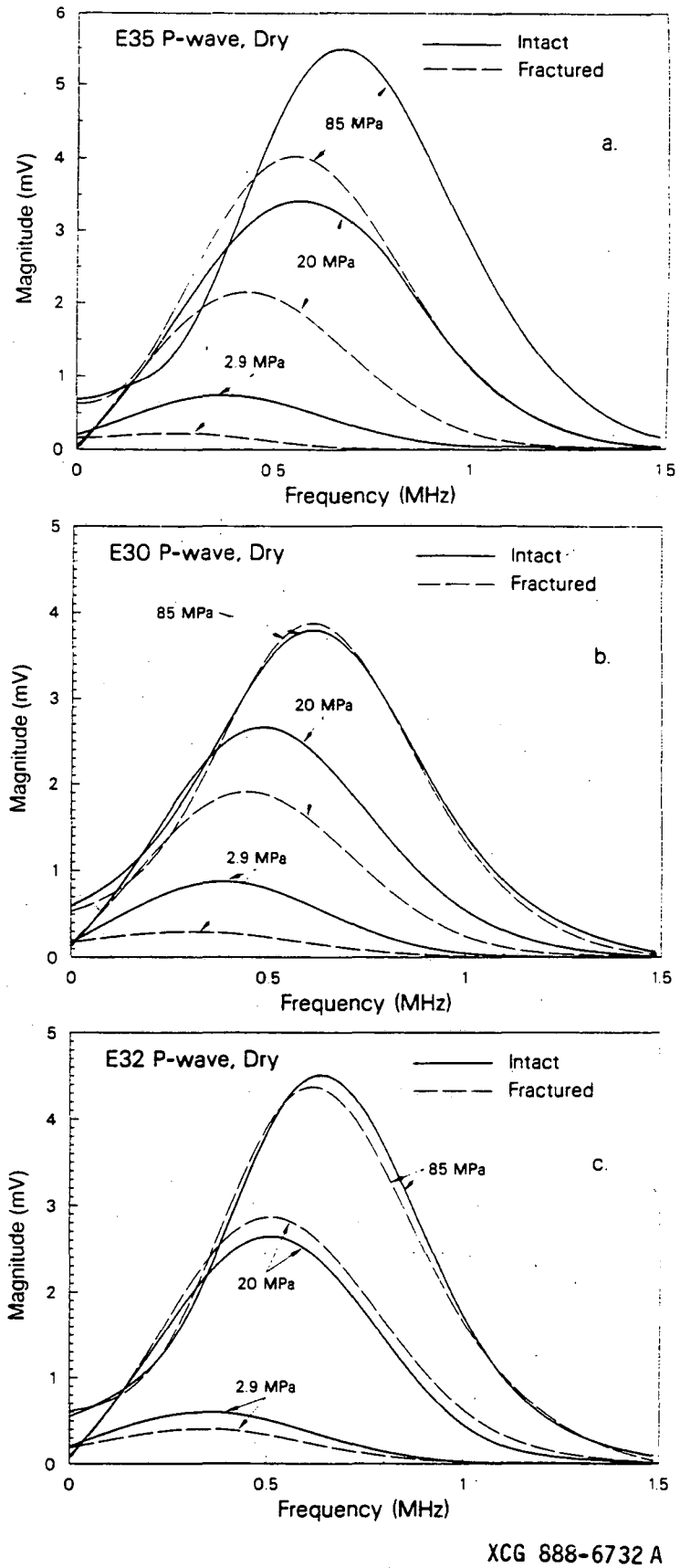

Figure 4. Comparison of P-wave spectra obtained from intact specimens with those obtained from fractured specimens.

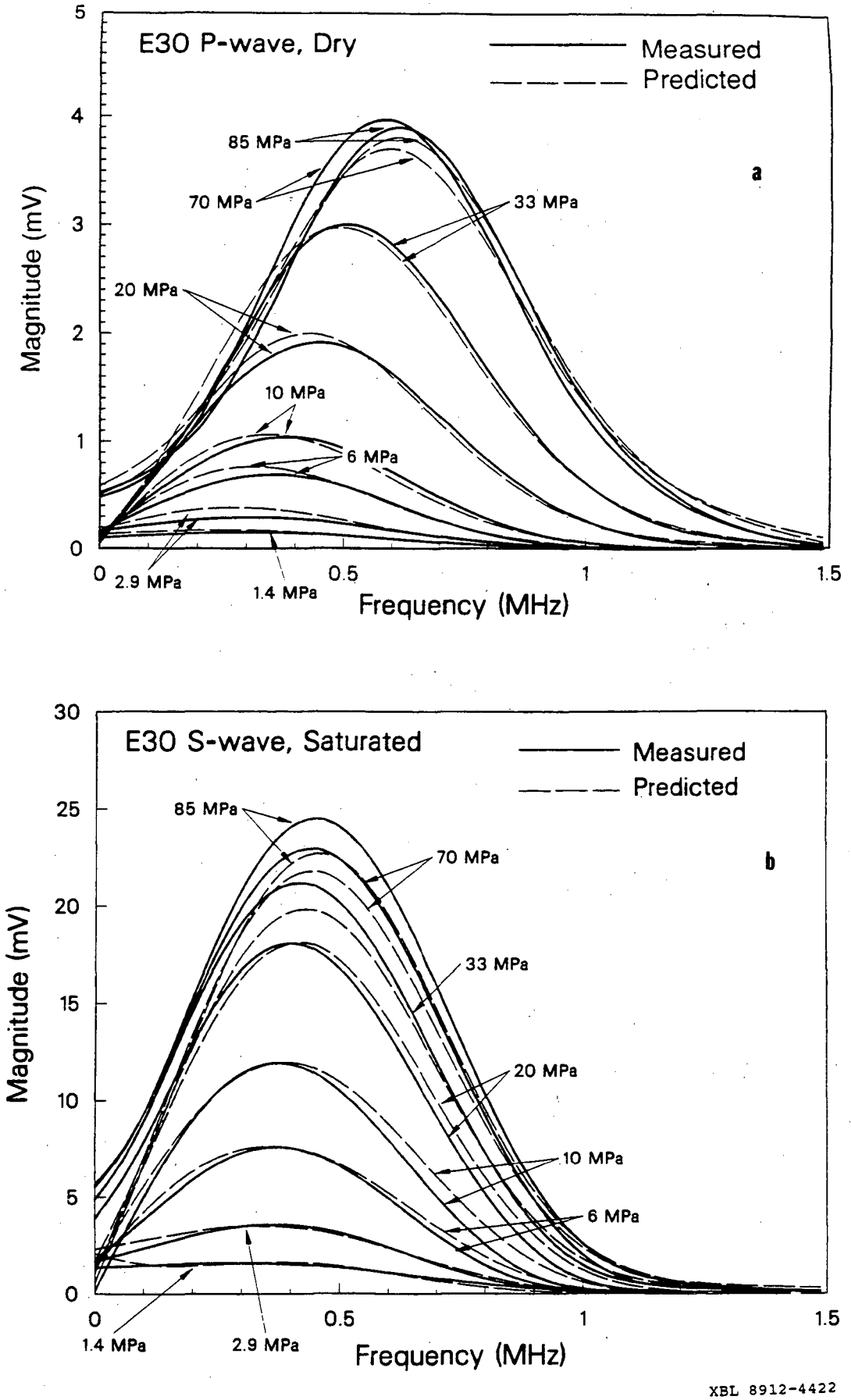

Figure 5. Comparison of measured spectra for fractured specimens with predicted spectra; (a) P-waves dry conditions, fit using only specific stiffness; (b) S-waves, saturated conditions, fit using specific stiffness and specific viscosity.

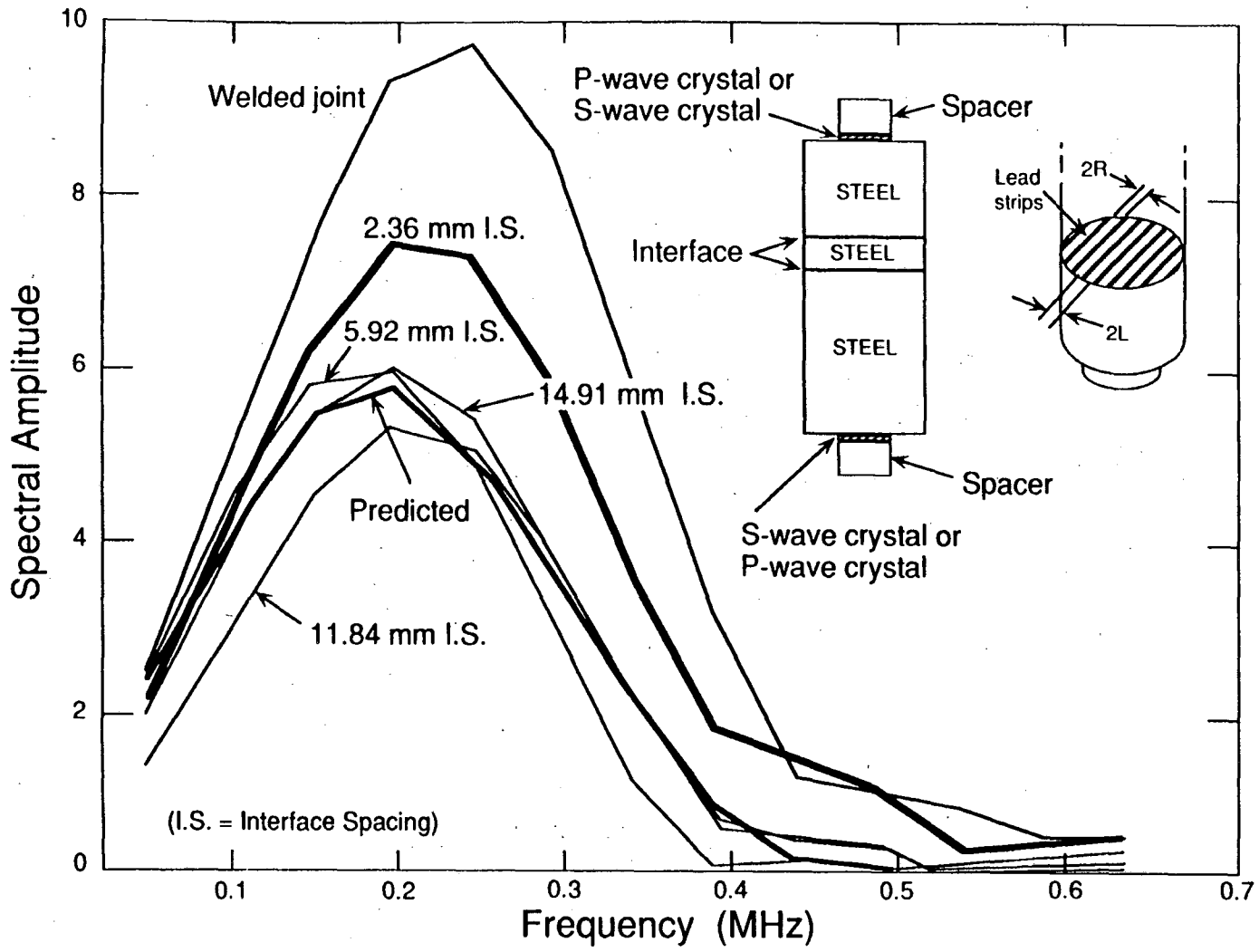

Figure 6. Amplitude spectra for P-wave pulses propagated across idealized fractures with different spacings, compared with spectrum for welded joint test and a predicted spectrum.

Application of Geophysical Methods for Fracture Characterization

K. H. Lee, E. L. Majer, H. F. Morrison and T. V. McEvilly

Introduction

One of the most crucial needs in the design and implementation of an underground waste isolation facility is a reliable method for the detection and characterization of fractures in zones away from boreholes or subsurface workings. Geophysical methods may represent a solution to this problem. If fractures represent anomalies in the elastic properties or conductive properties of the rocks, then the seismic and electrical techniques may be useful in detecting and characterizing fracture properties.

Seismic Methods

For years seismologists have known that fractures have an effect on the propagation of seismic waves. The problem has been in quantifying the effect so that useful parameters can be obtained. In the case of nuclear waste isolation, and in particular Yucca Mountain, the parameters of interest are not only the presence of fractures, but such features as length, width, orientation, density, spacing, aperture, and the degree to which the fractures are connected, and the manner of the connections.

Several years of research has been carried out to develop modeling capabilities for representing the seismic response of the repository volume at Yucca Mountain. The initial focus of this research was in the development of a model to predict how seismic waves travel through a fracture network. Whereas several numerical techniques are available for predicting fluid flow through fracture networks, the corresponding computational tools for determining how a seismic wave is affected as it is transmitted through a network of randomly located and oriented finite fractures was not available at the onset of this study. The development of such a seismic modeling tool has been a

high priority for this project.

Seismic velocity anisotropy has been found in many geological regimes (e.g. Robertson and Corrigan, 1983, Daley et al, 1988, Li, et al, 1987). In particular, zones of fracturing are often modeled as equivalent media with anisotropic propagation of seismic waves (Crampin, 1978 Hudson, 1981). Often, this effective anisotropy can not be overlooked when interpreting data, especially if shear-waves are utilized. The interpretation of data in fractured material, such as the reservoir rock in the Geysers geothermal field, would be improved by an anisotropic inversion scheme. However, the solution of an inverse problem is greatly complicated by assuming anisotropic media. Instead of two elastic parameters, lamda and μ, for isotropic media, an anisotropic material has, in general, 21 elastic parameters which are necessary for calculation of seismic wave velocities and direction of propagation. Study of fractured material, such as that present in the Geysers Geothermal field, has recently focused on anisotropic effects. The need for inversion of data recorded in known anisotropic material and recovery of the elastic constants controlling wave propagation is the motivation for the work presented here.

Inversion Theory

In recent years different approaches have been attempted for anisotropic inversion (Crampin et al., 1980, Hirahara and Ishikawa, 1984), mostly these attempts use P-waves only and, like our work, they utilize only the travel times. In this paper, the travel times of both P- and S-waves are used in a first-order perturbation method using ray theory which is valid for weakly anisotropic materials (Jech and Psencik, 1989). The perturbation of the total travel time for each wave type is obtained from perturbations of the elastic parameters along the raypath in the unperturbed medium. The unperturbed medium, which is the staring model for the inversion, can be isotropic or anisotropic with hexagonal symmetry, since these are the media in which the raypath can be computed. In addition, the starting model can be homogeneous or layered.

Calculating the travel time perturbations from elastic parameters falls into two separate cases, called degenerate and non-degenerate. The degenerate case is when two quasi-shear-waves have the same phase velocity (this is always true in the isotropic material) and the non-degenerate case is for different quasi-shear phase velocities.

Looking at the forward problem of calculating travel time from perturbations of elastic parameters, we find that for the non-degenerate case the correction Δt to the travel time t for a perturbation Δa_{ijkl} in the density normalized elastic parameter a_{ijkl} is given by

$$\Delta t = -\frac{1}{2}\int_{t_0}^{t} \Delta a_{ijkl}\, p_i p_l\, g_j^{(m)} g_k^{(m)}\, dt$$

where p_i is the slowness vector and $g_j^{(m)}$ is the eigenvector of the matrix $a_{ijkl}\, p_i p_l$ (Jech, and Psencik, 1989). The travel time is integrated along some parametrization of the raypath. (Note that the Einstein summation convention is used in these equations.) For the degenerate case we define the quantity $B_{mn} = \Delta a_{ijkl} p_i p_l g_j^{(m)} g_k^{(n)}$ and then the perturbation in travel time is

$$\Delta t_I = -\frac{1}{4}\int_{t_0}^{t}((B_{I1} + B_{22}) +/- [(B_{I1} - B_{22})^2 + 4\, B_{12}^2]^{\frac{1}{2}})\, dt \qquad I=1,2\,.$$

The inversion, based on the forward problem, seeks perturbations of the elastic parameters, along with the angles of rotation which define the axis of symmetry of the anisotropic material, which minimize the quantity ϕ in the least squares sense for

$$\phi = \sum_{i=1}^{N}(\Delta t_{io} - \Delta t_{ip})^2\,.$$

The implementation of the inversion used here allows for the solution to be constrained to be a homogeneous or layered model. The elastic parameters can vary independently with depth and any anisotropy symmetry can be considered. For a model with hexagonal anisotropy, the results of the inversion are the elastic constants a_{11} , a_{33}, a_{55}, a_{66} ,a_{13} and the orientation angle for the anisotropy axis of symmetry.b

The inversion was tested with a numerically generated data set consisting of travel time measurements for the qP, qS1, and qS2 arrivals. This data was generated from an anisotropic ray tracing code (Gajewski and Psencik,1987), and it is derived

from a model used in Shearer and Chapman, 1989, which is actually more anisotropic than the assumptions of the inversion allow. Fig 1a and 1b show the results of the inversion for this theoretical model. The solution is not exact, however the resulting anisotropic solution does approach the velocities of the original model. While other numerical examples with weak anisotropy had exactly correct solutions, this example shows that even when the initial assumption of weak anisotropy is violated, the inversion will approach the correct solution. To find a better solution to the Shearer and Chapman model, as well as other, more anisotropic models, an iterative inversion scheme would be needed. This one-step inversion using a first order linearization remains useful for weakly anisotropic materials.

Inversion of VSP Data

A Vertical seismic profile (VSP) recorded within the Geysers geothermal area provided a useful test of the inversion on field data. The 9-component VSP utilizing P- and S-wave vibrator sources and 3-component receivers was recorded such that the shear sources were parallel and perpendicular to dominant direction of fracturing in the reservoir rock (as best determined from other geological and geophysical information). The source offset was 518 m with receiver depths from 305 to 1555 m. Evidence of anisotropy was clearly seen as a travel time difference between the orthogonally oriented shear sources (Majer et al, 1988). In fact, the observed travel time difference indicated that the anisotropy may be stronger than allowed by the inversion assumptions, however we were hopeful that a solution would at least approach the correct elastic constants.

Attempts were made to invert the travel time data using various starting models. These models included the following:

1) a homogeneous media with hexagonal anisotropy with a horizontal axis of symmetry;

2) a homogeneous, isotropic material;

3) a 100m layer over a half-space, with the resulting model being an isotropic layer over an anisotropic half-space with constant vertical gradient of elastic parameters

(different gradients for each parameter).

All these models used an axis of symmetry for the anisotropic material which approximately aligned with the best known orientation for the Geysers. The best solution was able to match the travel times for all three wave types very well. Other solutions also matched the travel times however they had unrealistic values for some of the elastic parameters.

A similar set of models were attempted in which the anisotropy was allowed to have an axis of symmetry approximately perpendicular to the best known orientation. Unfortunately, the best results from this test were nearly as good as the test with the "correct" orientation of the axis. Further numerical examples demonstrated that the field data from the Geysers was not adequate for a unique inversion. More source points would be necessary for a better constrained solution. However, the Geysers data still has a "best" solution using constraints on the orientation of the axis of symmetry. This solution is shown in fig 2a and 2b; it is described in example 3 above with an orientation angle of 16.3° and velocities in the isotropic layer of 1.05 km/s for P and 0.7 km/s for S.

The resulting models were quite diverse, in fact, some did not correspond to the local geology and others gave elastic constants which did not correspond with the physics of wave propagation in cracked media (i.e. these elastic constants could not come from aligned cracks, or they did not correspond to physically realizable material). Despite these problems, many of these models give an excellent fit to the observed travel times. This demonstrates that while the travel time data from the Geyser's VSP clearly shows the anisotropy, it is insufficient for anisotropic inversion. One drawback is the narrow range of angles which the rays for the Geysers VSP cross the investigated region. The numerical experiments with the Shearer and Chapman model show that for the 100 to 700 m depths recorded, source offsets of 250, 500 and 750 m would provide a data set that consistently could be inverted (Fig 3). A more thorough VSP at the Geysers would have provided the opportunity for a unique anisotropic inversion.

Electrical Methods

A practical problem that occurs in the nuclear waste repository is the detection of any major fracture zone that lies close to but is missed by the boreholes. These holes provide the opportunity to use subsurface electromagnetic (em) techniques for detecting and characterizing any nearby fractures.

A number of techniques have been used to address the fracture detection problem and each has its own advantages and limitations. To date, however, most of the work centered on the use of conventional geophysical borehole logs to detect and characterize fractures intersected by drillholes. Because most holes are drilled close to vertical, conventional logging techniques are mainly sensitive to flat-dipping structures. In order to detect the possible presence of a major, more generally oriented, fracture zone not intersected by a borehole, other types of techniques need to be studied. Among these is the cross-hole em technique. The technique is particularly useful since an open but water-filled fracture zone in otherwise resistive rock has a much lower resistivity (Green and Mair, 1983). Deadrick et al. (1982) and Ramirez et al. (1983) used cross-hole em geotomography in mapping fractures. Lytle et al. (1979) also used cross-hole em probing to locate high-contrast anomalies, and Chang et al. (1984) developed down-hole VHF radar apparatus with directional source and receiver antennas in the borehole.

Primarily because of the high attenuation at radar frequencies, lower frequencies may be more suitable for fracture detection between widely spaced holes or where the host rock is more conductive than a low permeability granite. In this paper we consider downhole dipole sources. The position of the source can be either fixed or moving depending upon the desired type of source-receiver geometry. The fracture zone is represented by a thin rectangular conductor with finite dimensions, embedded in a host rock with much lower electrical conductivity. The source can be either a grounded vertical electric dipole or a vertical magnetic dipole.

The approach used to calculate the frequency domain magnetic field responses is based on the algorithm for conductive thin sheet developed by Weidelt (1981). The

following is a brief summary of the algorithm.

From the Maxwell's equations

$$\nabla \times \mathbf{E} = -\, i\omega\mu\mathbf{H} \tag{6}$$

$$\nabla \times \mathbf{H} = (\sigma + i\omega\varepsilon)\mathbf{E} + \mathbf{J} \tag{7}$$

the following equation for the electric field is obtained by using the thin sheet approximation (Price, 1949)

$$\mathbf{E}_s(\mathbf{r}_0) = \mathbf{E}_{ns}(\mathbf{r}_0) - i\omega\mu_0 \int_S \tau(\mathbf{r}) g_s(\mathbf{r}_0/\mathbf{r}) \cdot \mathbf{E}_s(\mathbf{r}) ds \tag{8}$$

Here the integration is carried out on the sheet surface s. $\mathbf{E}_s$ is the total tangential electric field on the sheet, and $\mathbf{E}_{ns}$ is the incident tangential electric field on the sheet. $g_s(\mathbf{r}_0/\mathbf{r})$ is the Green's dyadic function relating the tangential current distribution on the sheet at $\mathbf{r}$ to the tangential electric field at $\mathbf{r}_0$. The conductance τ is the product of the conductivity and the thickness of the sheet, and can be a variable over the sheet.

Both the incident field and the Green's dyadic function are related to the dipole fields in the layered medium, and are easy to evaluate. After these are calculated, the integral equation is then solved for $\mathbf{E}_s$, which in turn is used to calculate the magnetic field everywhere using

$$\mathbf{H}(\mathbf{r}_0) = \mathbf{H}_n(\mathbf{r}_0) + \int_S \tau\,(\mathbf{r})\mathbf{E}_s(\mathbf{r}) \cdot \nabla_0 \times g(\mathbf{r}_0/\mathbf{r}) ds \tag{9}$$

Here $\mathbf{H}_n$ is the incident magnetic field and the product $\tau\mathbf{E}_s$ is called the scattering current. The function $\nabla_0 \times g$ is now considered the Green's tensor for the magnetic field. Some typical numerical results have been obtained to demonstrate the properties of the anomalous magnetic fields due to different type of sources, frequencies, and source-receiver geometries. The model used is typically a rectangular sheet of 150 m by 100 m in size. The sheet is vertically oriented and has a conductance of 1 S while the host rock has a conductivity of 10 mS/m. Because the sheet conductor is placed far below the surface, the observed response will be basically the same as that for a conductor in a homogeneous whole space. It should be pointed out, however, that the

code can handle the more general realistic problem of a target close to the ground surface or to a layered interface.

For the case when the grounded electric dipole source is used, the cross-hole moving source in one hole with the magnetic field receiver in another hole show better resolution of the fracture than the cross-hole fixed source configuration. The moving source-receiver configuration also allows for easier data interpretation because the primary field is constant, as long as the target is located well below the surface of the earth. With the same amount of dipole moment, the grounded electric dipole source (moment = current × dipole length) results much stronger anomalous fields than its vertical magnetic dipole (moment = number of turns × current × area) counterpart. Nevertheless the relative values of these are about the same for either source. It is difficult to employ a large moment vertical magnetic dipole source since the diameter is small for most boreholes, and the number of turns of the coil is limited. On the other hand, the anomalous field generated by a grounded electric dipole can be easily made detectable by simply employing longer dipoles.

The inductive coupling between the source field and the target largely depends on the relative geometry. When the target is horizontal the maximum coupling occurs if a vertical magnetic dipole is used. On the other hand if the target is vertical with zero strike angle, maximum coupling can be achieved if a vertical electric dipole is used. Therefore, it is necessary to use both type of sources if an accurate interpretation for the fracture distribution between holes is desired.

References

Chang, H-T, Suhler, S. A. and Owen, T. E., 1984, Evaluation of borehole electromagnetic and seismic detection of fractures: Sandia National Laboratories, Report SAND 84-7109, 75 p.

Crampin S., Evaluation of anisotropy by shear-wave splitting, *Geophysics, v50,* n1, p142-152, 1985.

Crampin S., Seismic-wave propagation through a cracked solid: polarization as a possible dilatancy diagnostic, *Geophys. J. Roy. Astr. Soc.,* 53, 1978.

Crampin S., R. McGonigle, D. Bamford, Estimating crack parameters from observations of P-wave velocity anisotropy, *Geophysics* ,45, 1980.

Daley T. M., T.V. McEvilly and E.L. Majer, Analysis of P- and S-Wave VSP Data from the Salton Sea Geothermal Field, *J. Geophys. Res.,* 93, 1988.

Deadrick, F. J., Ramirez, A. L. and Lytle, R. J., 1982, In-situ fracture mapping using geotomography and brine tracers: IEEE Transaction on Nuclear Science, v. NS-29, n. 1.

Gajewski, D. and I. Psencik, Computation of high-frequency seismic wavefields in 3-D laterally inhomogeneous anisotropic media, *Geophys. J. Roy. Astr. Soc.,* 91, 1987.

Green, A. G. and Mair, J. A., 1983, Sub-horizontal fracture in a granitic pluton: Their detection and implications for radioactive waste disposal: Geophysics, v. 48, p. 1428-1449.

Hirahara, K., Y. Ishikawa, Travel-time inversion for three-dimensional P-wave velocity anisotropy, *J. Phys. Earth.,* 32, 1984.

Hudson, J.A., Wave speeds and attenuation of elastic waves in material containing cracks, *Geophys. J. Roy. Astr. Soc., 64, 1981.*

Jech, J. and I. Psencik, First order perturbation method for anisotropic media, *Geophys. J. Int.,* p310, 1989.

Li, Y.-G., P.C. Leary and T.L. Henyey, Stress orientation inferred from shear wave splitting in basement rock at Cajon Pass, *Geoph. Res. Let.,* 15, 1988.

Lytle, R. J., Laine, E. F., Lager, D. L. and Davis, D. T., 1979, Cross-borehole electromagnetic probing to locate high-contrast anomalies: Geophysics, v. 44, n. 10.

Majer, E. L., McEvilly T. V., Eastwood F., and Myer L., Fracture detection using P- and S-wave VSPs at the geysers geothermal Field, *Geophysics,* 53, 1988.

Oristaglio M.L., A Guide to the current uses of vertical seismic profiles, *Geophysics, v50,* n12, p2473, 1985.

Price, A. T., 1949, The induction of electric currents in nonuniform thin sheets and shells: Q. J. Mech. Appl. Math., v. 2, p. 283-310.

Ramirez, A. L. and Lytle, R. J., 1983, Alternate geophysical tomography: IGRASS, v. 2, Paper FA 2-9.

Robertson, J.D. and D. Corrigan, Radiation patterns of a shear-wave vibrator in near-surface shale, *Geophysics,* 48, 1983.

Shearer, P. M. and C. H. Chapman, Ray tracing in azimuthally anisotropic media - I. Results for models of aligned cracks in the upper crust, *Geophy. J. Roy. Astr. Soc.,* 96, 1989.

Weidelt, P., 1981, Report on dipole induction by a thin plate in a conductive half-space with an overburden: Federal Institute for Earth Science and Raw Materials, Hannover, FRG.

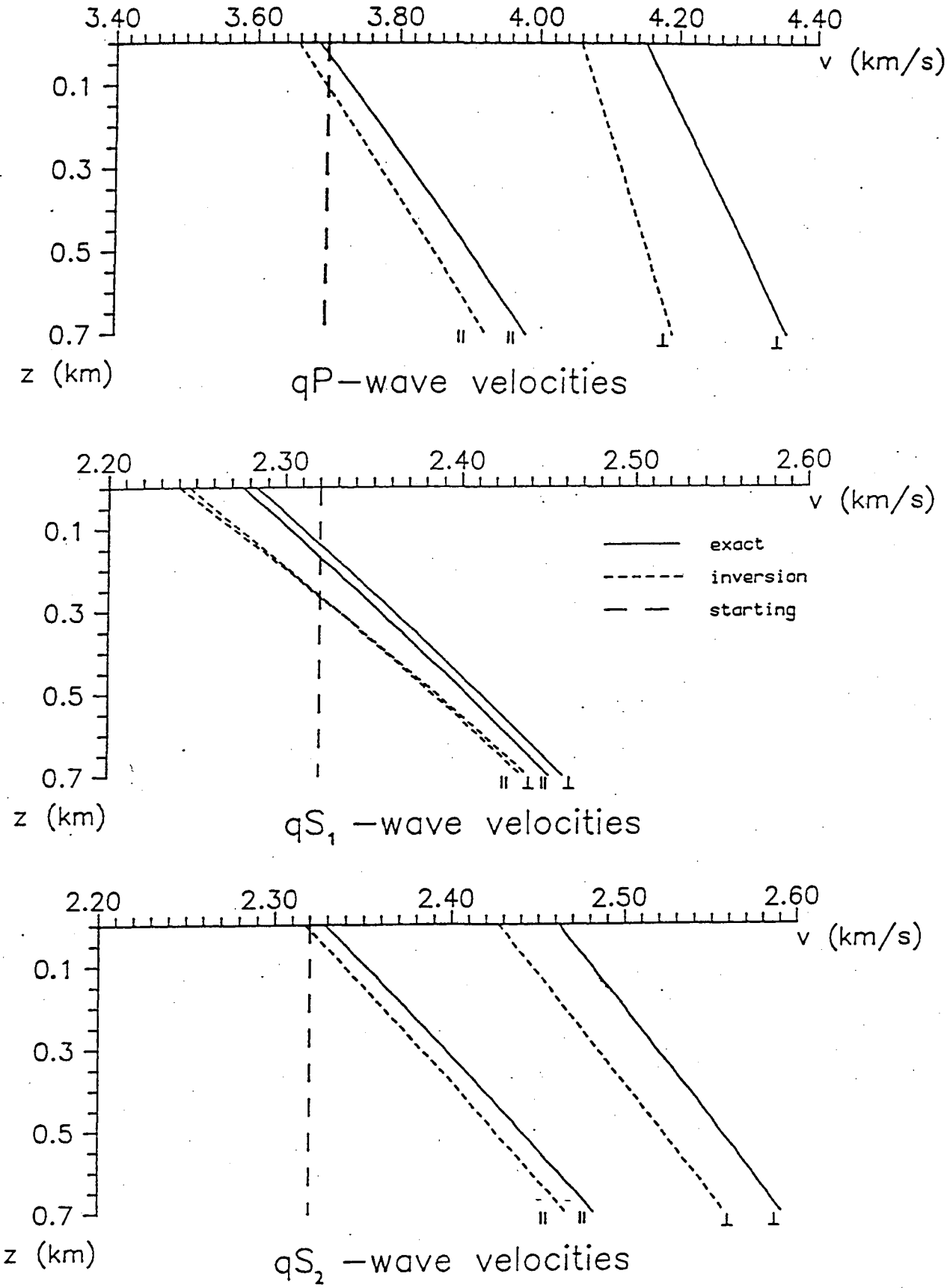

Fig. 1a. Inversion result for theoretical model. Each graph is a plot of velocity vs depth for each of the three wave types - qP, qS1 and qS2, from top to bottom. The large dashed line is the starting model, the small dashed line is the inversion result, and the solid line is the exact solution. Each plot has the velocity at two azimuths, parallel and perpendicular to the axis of symmetry of the anisotropy.

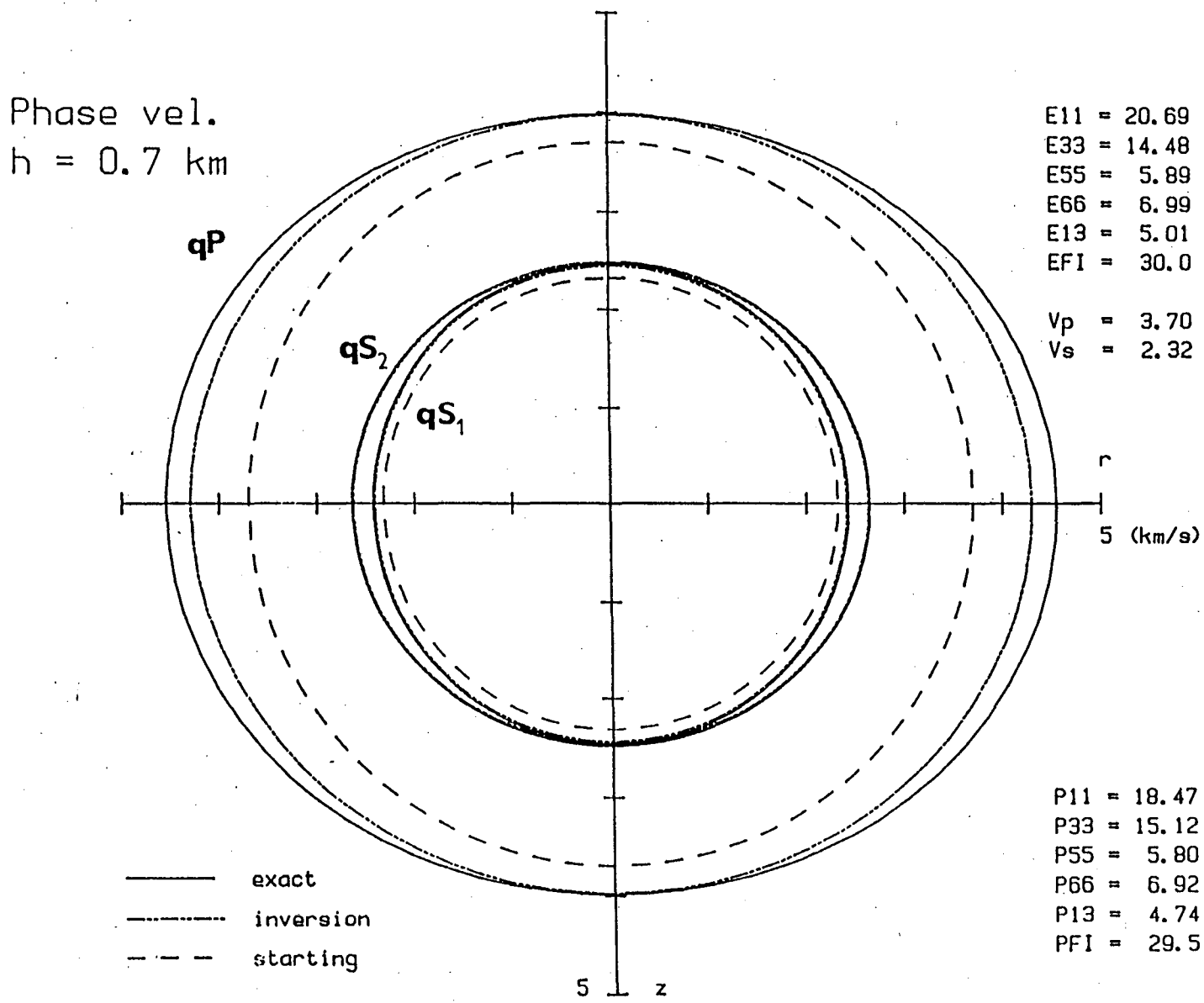

Fig. 1b. Inversion result for theoretical model. Phase velocity for each wave type is plotted as a function of azimuth at one depth (700 m). E_{ij} are the exact elastic constants and P_{ij} are the perturbed elastic constants. EFI is the orientation angle and Vp and Vs are the velocities of the starting model. The solid, large dashed and small dashed line are the exact, starting and inverted models respectively.

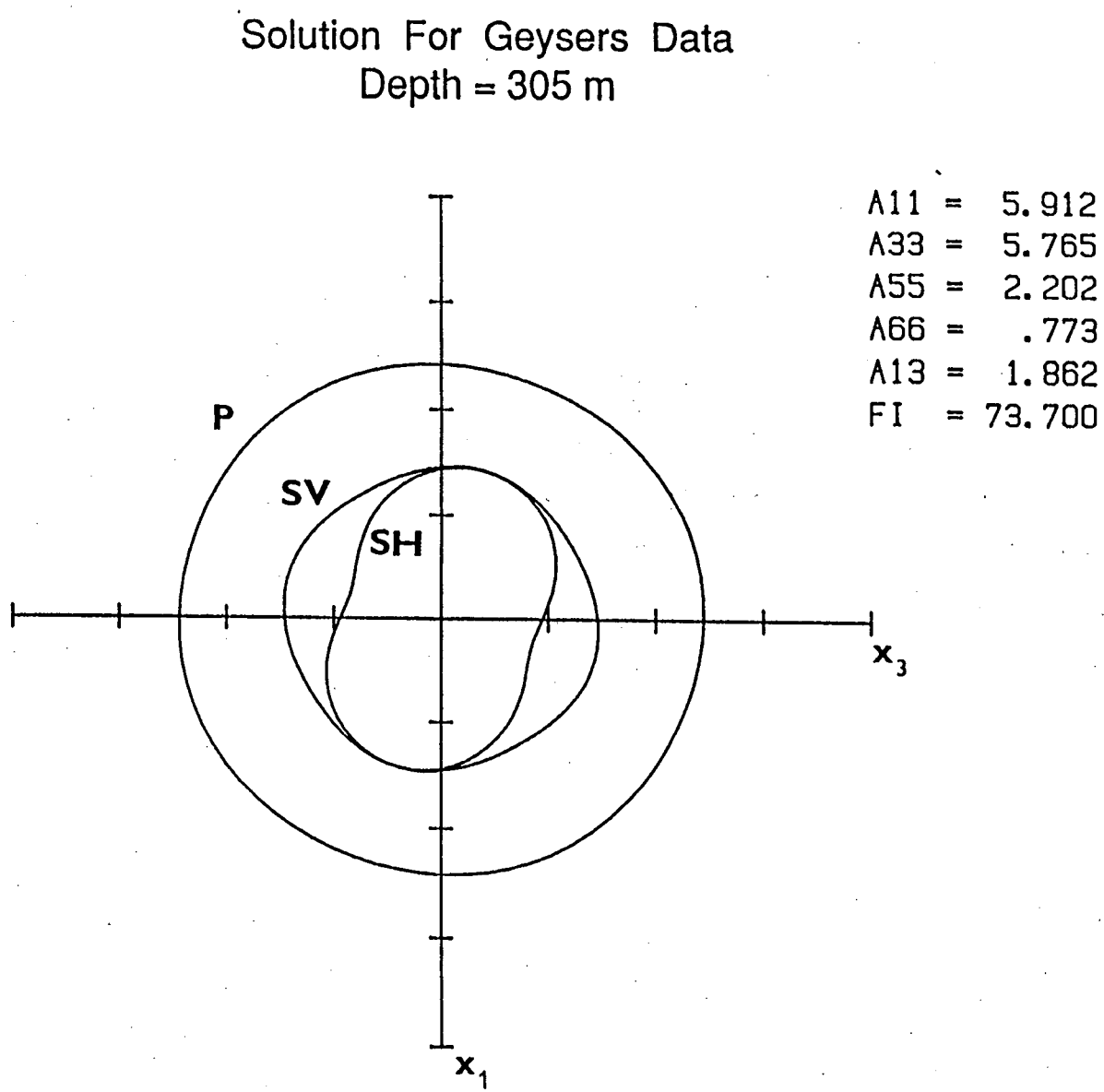

Fig. 2a. Inversion result for Geysers data at 305 m. A_{ij} are the inverted elastic parameters for the anisotropic half-space. The section is perpendicular to the VSP, seen in the direction from the source towards the receiver. The axis of symmetry of the resulting hexagonal medium is situated in a plane perpendicular to the profile.

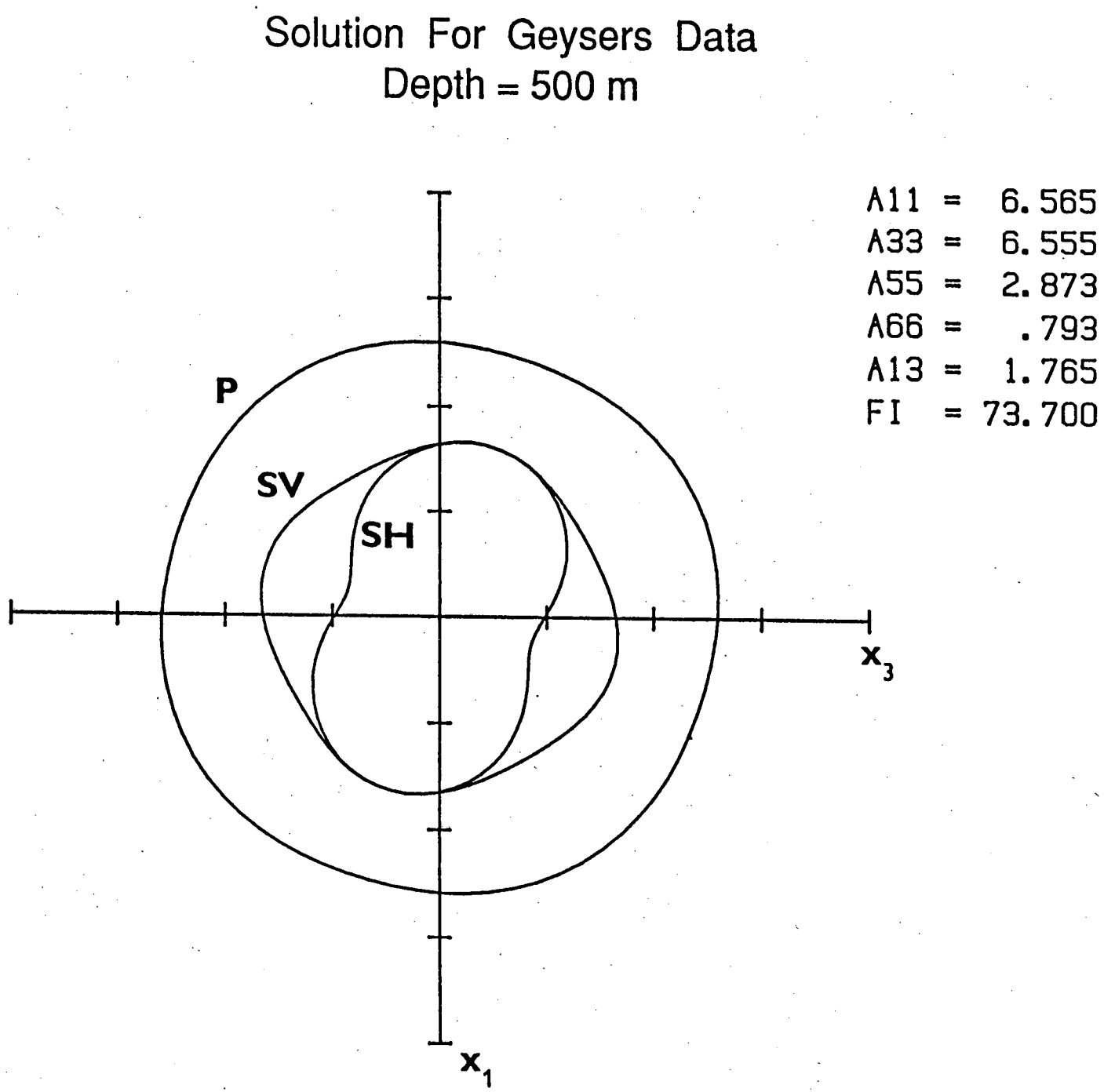

Fig. 2b. Same as Fig 2a, but for 500 m.

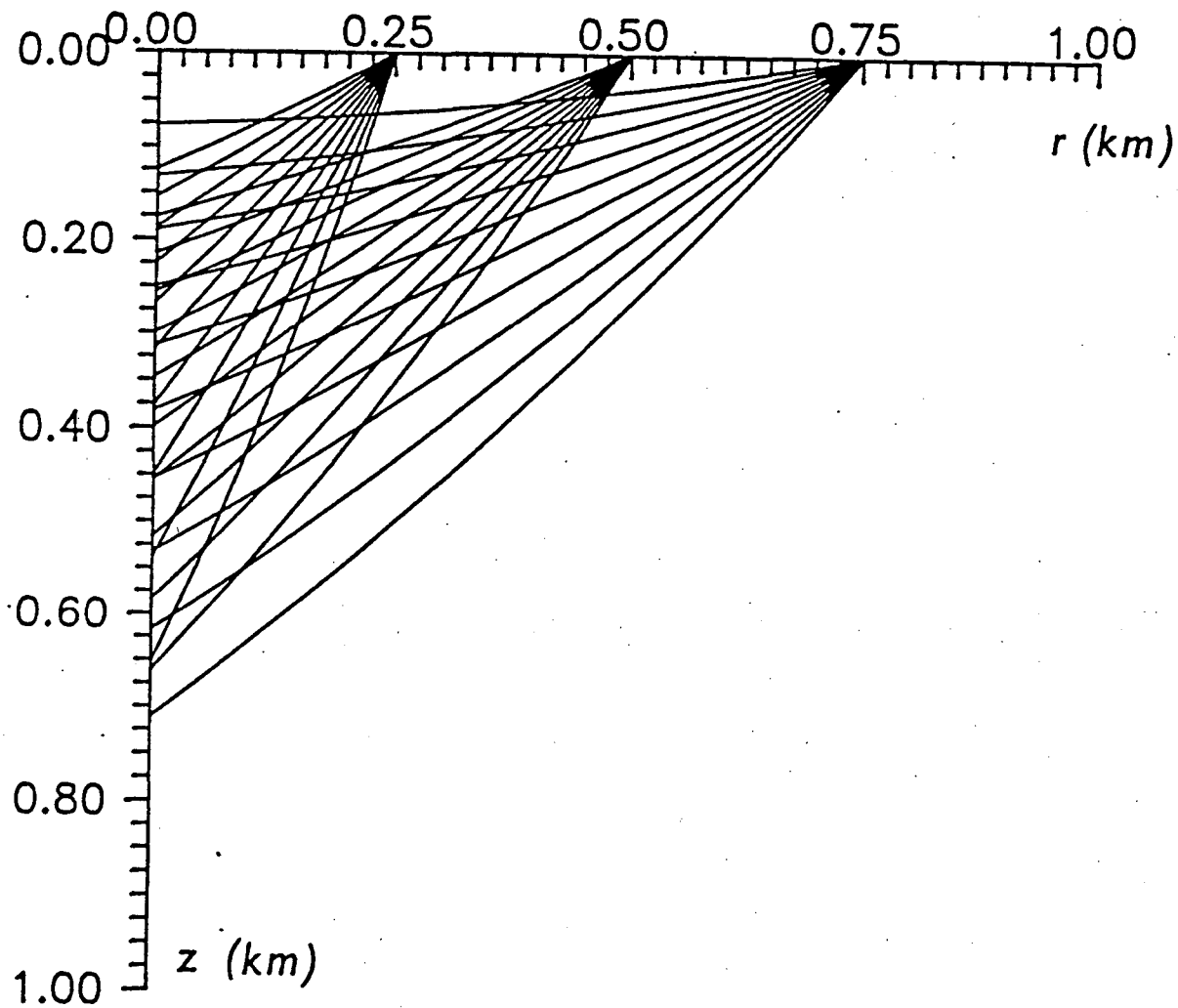

Fig. 3. Geometry of VSP source locations which should provide a unique solution for an anisotropic inversion of the Geysers data. The data set used for inversion had only the 500 m offset. The rays are drawn for the P-wave using for the Shearer and Chapman model.

A Mechanical Model for Repeated Slip Events Along Normal Faults in the Basin and Range: Applications to Yucca Mountain, Nevada

John M. Kemeny

A mechanical model has been developed to calculate the effects of repeated slip events along pre-existing normal faults in the Basin and Range. Depending on the boundary conditions and material properties of the ground, these slip events can result in aseismic and/or seismic events. It is known that slip along pre-existing normal faults are responsible for great earthquakes in the Basin and Range, such as the magnitude 7.5 earthquake at Hebgen Lake, Montana on August 18, 1959, and the magnitude 7.3 earthquake at Borah Peak, Idaho on October 28, 1983. The mechanical model consists of a two dimensional linear elastic plate containing an edge crack at an angle β from horizontal. The plate is loaded by gravity forces and tectonic extension. Friction along the crack surface is also taken in to account. A normal faulting slip event is modelled as the propagation of the crack from its initial position towards the free surface. The model calculates the aseismic and seismic deformation due to the propagation of slip along the normal fault, and the moment and energy release associated with seismic motion. Also, the model calculates regional stress changes associated with a slip event, from which changes in the level of the water table are estimated. The model is calibrated by modelling the magnitude 7.5 Hebgen Lake, Montana earthquake of August 18, 1959. The model is then used to predict the effects of a slip event on normal faults in the vicinity of Yucca Mountain, Nevada, which is the proposed site for underground nuclear waste storage. Assuming that slip initiates from a shallow, low angle detachment fault near Yucca Mountain, an unstable normal faulting event with a seismic moment of 3×10^{24} dyne-cm (approximate magnitude 5.6) and a stress drop of 110 bars is predicted. Based on this stress drop, a rise in the water table is predicted. If only the effects of the squeezing of pores are considered, then the predicted rise in the water table is approximately 0.75 meters. However, if the effects of the stress drop on a saturated fault is considered, a rise in the water level along the fault of over 90 meters is estimated. Based on a uniform extension rate in the Basin and Range of 9 mm/year, and assuming that this extension is distributed evenly over the Basin and Range, the model predicts a recurrence interval for slip along normal faults in the vicinity of Yucca Mountain of 29,300 years.

Introduction

The Basin and Range province occupies the whole of Nevada and parts of Oregon, Idaho, Wyoming, Utah, California, Montana, and Arizona. The Basin and Range is an extensional regime, cut by widely spaced (20 - 30 km) and relatively steeply dipping normal faults that penetrate down to the brittle-ductile transition at a depth of 10 - 20 km (e.g., Smith and Bruhn, 1984). It is well known that these normal faults are responsible for large earthquakes in the Basin and Range, such as the magnitude 7.5 earthquake at Hebgen Lake, Montana on August 18, 1959 (Nolan, 1964; Doser, 1985), and the magnitude 7.3 earthquake at Borah Peak, Idaho on October 28, 1983 (Doser and Smith, 1985; Stein and Barrientos, 1985). The Basin and Range is also cut in places by shallow, low dipping (less than 30°), detachment faults. These faults have in some circumstances undergone translational displacements in excess of tens of kilometers (Davis and Lister, 1988), yet because of the lack of normal faulting earthquakes on fault planes dipping at less than 30°, it must be assumed that deformation along detachment faults in the Basin and Range occurs aseismically (England and Jackson, 1987). There are a number of brittle structural features associated with the shallow detachment faults, such as steeply dipping normal faults above the detachment faults that terminate at the detachment surface, and listric normal faults that merge into the detachment surface. Whether these structural features deform seismically or aseismically is not well understood at the present time.

Yucca Mountain, located in southwestern Nevada, is a possible site for the underground storage of nuclear waste. Yucca Mountain is cut by a series of steeply dipping normal faults. The most important of these are the Solitario Canyon and Bow Ridge faults on the western and eastern flanks of Yucca Mountain, respectively, and the Ghost Dance fault, which goes directly through the proposed repository site (see Figure 1). In addition to these normal faults, there is evidence in the region southwest of Yucca Mountain to support the existence of a shallow detachment fault at a depth between two and four km below Yucca Mountain (Scott, 1986; DOE, 1988a). Thus the steeply dipping normal faults that

cut Yucca Mountain may terminate at or merge with this shallow detachment fault, or the normal faults may pass through the detachment fault and extend to much greater depths, as depicted in Figure 2.

It is important to determine the consequences of fault motion on normal and detachment faults in the region surrounding Yucca Mountain. In addition to ground shaking and fault offsets, the stress regime in the ground can be significantly altered due to motion along these faults. Two kinds of stress changes can occur due to fault motion in the Basin and Range. The first is a redistribution of stress away from areas that have slipped towards unslipped areas. In this case the average stress in the region remains unchanged. The second is a regional change in stress, and in this case the average stress in the region changes. Regional stress changes occur due to the fact that the driving force for motion along faults in the Basin and Range is from viscous motion below the brittle-ductile transition (e.g., Hamilton, 1987). For short-time events such as seismicity, this viscous coupling responds like a fixed-displacement boundary condition. Since the far field displacements are fixed, the energy used up by the earthquake causes elastic stresses built up in the Lithoshpere to drop. For strike-slip faulting, calculations of the drop in tectonic stress due to faulting have been made (Andrews, 1978; Turcotte et al., 1979; Kemeny, 1988). In an extensional regime such as the Basin and Range, a drop in tectonic stress due to faulting results in an increase in compressive stress in the elastic Lithosphere. This is illustrated in Figure 3. After the earthquake, the stresses in the Lithosphere slowly rebuild due to the continuing viscous motion at depth, resulting in another earthquake at a future time when the stresses have built up to their previous level, and completing the earthquake cycle.

These changes in stress in the ground can induce pore pressure changes and groundwater flow. The local stress changes induce flow from regions of high pore pressure towards regions of low pore pressure. For the case of strike-slip faulting, this has been analyzed by Li et al. (1987), and the results of this analysis are supported by field data

on pore pressure changes during creep events by Johnson et al. (1973) and others. The regional stress changes could, by being large scale, cause regional changes in pore pressure. As illustrated in Figure 3, regional stress changes due to faulting in the Basin and Range should result in an increase in compressive stress in the ground. One effect of this increase in compression is to reduce the pore volume of the rock, which increases pore pressure and could induce regional water level changes. An increase in compression can also squeeze fluids out of cracks and fault zones, and towards the ground surface, as analyzed by Sibson (1981, 1982). This has important implications at Yucca Mountain, since at the present time the water table is approximately 250 meters below the proposed level for the repository.

In this paper a model for the mechanics of repeated slip events on pre-existing normal faults in the Basin and Range is presented. In this model, the propagation of slip along a single, planar, normal fault is explicitly considered. The propagation of slip can initiate either from an aseismically deforming detachment fault, or from aseismic slip below the brittle-ductile transition. These calculations are based on quasi-static fracture mechanics, and are extensions of work conducted on strike-slip faulting by Kemeny (1986, 1988). An important element of this model is that based on realistic boundary conditions for the Basin and Range, both kinds of stress changes due to faulting as described above are predicted. In particular, as driving forces for slip along faults, we consider the combined effects of gravity and far field displacements imposed by viscous coupling below the brittle-ductile transition. During a slip event, the gravity forces must remain constant, but the forces that are pulling apart the Basin and Range will change, resulting in stress changes over large regional areas.

The model calculates both aseismic and seismic deformation due to the propagation of slip along the normal fault, and the moment and energy release associated with seismic motion. Also, the analysis gives regional stress changes associated with seismic and aseismic deformation, and from these stress changes, estimates of changes in the level of

the water table are made. The model is calibrated by modelling the magnitude 7.5 Hebgen Lake, Montana earthquake of August 18, 1959. The model is then used to predict the effects of a slip event on normal faults in the vicinity of Yucca Mountain, Nevada, which is the proposed site for underground nuclear waste storage. Assuming that slip initiates from a shallow, low angle detachment fault near Yucca Mountain, an unstable event with a seismic moment of 3×10^{24} dyne-cm and a stress drop of 110 bars is predicted. Based on this stress drop, a rise in the water table is predicted. If only the effects of the squeezing of pores are considered, then the predicted rise in the water table is less than one meter. However, if the effects of the stress drop on a saturated fault is considered, a rise in the water level along the fault of over 90 meters is estimated. A simple calculation of the recurrence rate for slip events is also made. Based on a uniform extension rate in the Basin and Range of 9 mm/year, and assuming that this extension is distributed evenly over the Basin and Range, the model predicts a recurrence interval for slip along normal faults in the vicinity of Yucca Mountain of 29,300 years.

The analyses presented in this paper assume that the processes of mechanical deformation and pore pressure changes are uncoupled. In the future, more complex models could be developed that couple the elastic deformations, pore pressure changes, and flow. This has been analyzed for other geologic situations by Rice and Cleary (1976), Li et al. (1987), Detournay and Cheng (1988), and others.

Mechanical Model

Consider the simple model for faulting in the Basin and Range as shown in Figure 4. The model consists of a two dimensional (plane strain) linear elastic plate of width b and thickness t containing a single edge crack of initial length l_o at an angle β from horizontal. The top surface of the model represents the ground surface. The bottom surface of the model represents either the lower limit of brittle behavior (brittle-ductile transition), or a detachment fault surface (assumed horizontal). In both cases the movement along the

bottom surface of the model is assumed to occur aseismically. The normal fault is represented by the angle crack, and a slip event along the normal fault is modelled as the propagation of the crack from its initial position towards the top of the plate. Modelling the propagation of slip along a pre-existing fault plane as the in-plane propagation of a crack has been considered previously for the case of strike-slip faulting by Kemeny (1986), Li and Rice (1987), Martel and Pollard (1989), and others. Since the edge crack is at the lower surface of the model, this model assumes that rupture nucleates deep in the ground and ruptures upward, which agrees with observations in the Basin and Range (e.g., Sibson, 1982).

Tectonic extension is modelled by considering an imposed extensional displacement, D, at a distance *d* from the normal fault. For simplicity, we assume that the applied displacements are uniform with depth, which agrees with several models for strain accumulation in the Basin and Range (England and Jackson, 1987; Lin and Parmentier, 1988). Because the plate is assumed to be elastic, there is a linear relationship between the far field applied displacement and the far field stress, σ, which depends on the elastic properties of the ground, the dimensions of the body, and the length of the edge crack. Since the far field displacements are fixed, the propagation of the crack will result in a decrease in σ.

The other important driving force in the model is gravity. We assume the vertical stress due to gravity as that due to the weight of the overburden material. Thus the vertical stress due to gravity will increase linearly with depth, given by $\sigma_v = \rho gh$, where ρ is the ground density, g is the gravitational acceleration, and h is the depth below the ground surface. Gravity also imparts a horizontal stress, due to an elastic effect from the vertical stress, and also due to non-elastic deformation such as compaction and slip along joints and faults. Based on Zoback and Zoback (1980) and others, the horizontal stress in the direction perpendicular to normal faulting in the Basin and Range is the minimum principal stress, which is a result of the regional extension in that direction. For our purposes, we are

interested in the value of the horizontal stress if the tectonic extension were turned off (since we model the tectonic extension separately). Under the assumption of vertical loading with lateral constraint, the horizontal stress due to gravity alone would be $\nu/(1-\nu)$ times the vertical stress at any depth, where ν is Poisson's ratio (Jaeger and Cook, 1979). More realistic assumptions about ground deformation give a horizontal stress closer to 1 times the vertical stress at any depth (e.g., McGarr, 1988). For the Basin and Range, a good approximation for the component of horizontal stress perpendicular to normal faulting due to gravity alone may be the value of the horizontal stress in the direction of the normal faults, which is still less than the vertical stress (Zoback and Zoback, 1980), but greater than that due to the Poisson's ratio effect alone. We have left the horizontal stress as a variable, as a constant F times the vertical stress at any given depth. For the Basin and Range, it is expected that F will range from 0.6 to 1.0.

Aseismic and seismic deformation along the normal fault occur by the propagation of the crack towards the free surface. We make the assumption that the crack will grow in the plane of the fault, which is consistent with the macroscopic response for the propagation of slip along a pre-existing fault plane. It does ignore, on a smaller scale, the extensile features that can form near a deforming slip surface. At first glance, it appears that this problem will involve crack growth due to both opening (mode I stress intensity factor, K_I) and shearing (model II stress intensity factor, K_{II}). However, it tuns out that because of the gravity forces, and assuming reasonable properties, the crack begins to propagate in shear while the crack is still closed under compressive normal stresses ($K_I = 0$). This is not an assumption, and in the analysis, a check is made as to whether the crack opens up ($K_I > 0$) before crack propagation in shear occurs. Only in the case of unrealistic material parameters is is possible for the crack to open before it starts to propagate in shear. Thus the model considers slip that is driven solely by the mode II stress intensity factor, K_{II}, and this will result in a slip event that is 'pure double couple'. Also, it is assumed that the closed crack is subject to frictional constraints. Thus the assumption is made that the crack

face is under a non-uniform frictional stress τ^f, where at any point along the crack surface $\tau^f = \mu_f \sigma_n$, where μ_f is the linear coefficient of friction and σ_n is the normal stress at that point.

A closed form solution for K_{II} has been estimated for the model with an arbitrary angle β, based on the stress intensity factor solution for an edge crack in a finite plate (Tada et al., 1973). The derivation is given in the Appendix A. This solution includes the effects of tectonic extension, gravity, and friction, and is given by:

$$K_{II} = \left[\sigma + \rho g b\,(1.12 - 0.68\chi)(1 - F) + \sigma_n \mu_f\right] \sin\beta\cos\beta \sqrt{\pi l}\; Y_{II}(\chi) \qquad (1)$$

where

$$\sigma_n = \left[\sigma - \rho g b\,(1.12 - 0.68\chi)\left(\frac{1}{\tan^2\beta} + F\right)\right]\sin^2\beta$$

$$Y_{II}(\chi) = \frac{1.12 - 0.56\chi + 0.085\chi^2 + 0.180\chi^3}{\sqrt{1-\chi}}$$

and

$$\chi = \frac{l\sin\beta}{b}$$

Here we use the sign convention that tension is positive. Initially, for small σ, K_{II} may be negative, and this indicates that the crack faces are locked due to frictional forces. As σ is increased, the frictional forces decrease and the driving forces along the crack increase, resulting in slip along the crack faces for $K_{II} > 0$. Also, $\sigma_n > 0$ indicates that the crack faces are under tension and the assumption that the crack surfaces are closed and under frictional forces is no longer valid.

Following rate-independent linear elastic fracture mechanics (e.g., Lawn and Wilshaw, 1975), it is assumed that the crack will grow when the energy release rate, G, becomes

equal to some critical value referred to as G_c. G_c represents the energy required for the breakdown processes at the crack tip and is a material property, while G is related to the stress intensity factors and is a function of crack geometry and the applied stresses and strains. Under pure mode II loading, G is related to K_{II} by (plane strain):

$$G = \frac{K_{II}^2 (1 - \nu^2)}{E} \tag{2}$$

where E is Young's modulus and ν is Poisson's ratio. G_c is one of the most important parameters in the model. G_c has been found to be very scale dependent, and also to vary with normal stress (Wong, 1982, 1986; Kemeny and Cook, 1987). We estimate a value for G_c for normal faulting in the Basin and Range by modelling known earthquakes and comparing the measured source parameters with calculated ones (and assuming G_c is constant with changes in crack length).

Together, equations (1) and (2) control the stress at the onset of crack growth, and the change in stress as the crack continues to propagate towards the ground surface. Since the stresses due to gravity remain constant as the crack propagates, the only stress that changes is the far field tectonic stress, σ. The value of σ at which cracking will occur for a crack of length l, referred to as σ^*, is calculated from equations (1) and (2) under the restriction that $G = G_c$, and gives:

$$\sigma^* = \frac{\sqrt{\frac{G_c E}{(1 - \nu^2)\pi l}} \frac{1}{\sin\beta\cos\beta Y_{II}} - \rho g b(1.12 - 0.68\frac{l\sin\beta}{b})\left[1 - F - \mu_f(\cos^2\beta + F\sin^2\beta)\right]}{1 + \mu_f \sin^2\beta} \tag{3}$$

In addition to a change in stress, a change in crack length is associated with a change in the double-couple component of the seismic moment, M_o. For the two dimensional crack

representing the normal fault in this model, the seismic moment is defined as (Aki and Richards, 1980):

$$M_o = l \mu \bar{\delta} t \tag{4}$$

where $\bar{\delta}$ is the average relative shear displacement of the crack surfaces, and μ is the elastic shear modulus. $\bar{\delta}$ can be calculated for the model in Figure 4 by integrating the energy release rate, G, over the length of the crack and utilizing equations (1) and (2), as described in Appendix B. Then, using equation (4), this gives the following closed form solution for M_o:

$$M_o = b^2\pi t(1-\nu)\cos^2\beta(1 + \sin^2\beta\mu_f)\Big[\sigma(1 + \sin^2\beta\mu_f)I_1(\chi) + \rho g b(1 - F - \sin^2\beta\mu_f)(\frac{1}{\tan^2\beta} + F)(1.12I_1(\chi) - 0.68I_2(\chi))\Big] \tag{5}$$

where

$$I_1(\chi) = -0.67\ln(1-\chi) - 0.638 + 0.906(1-\chi) - 0.638(1-\chi)^2 + 0.502(1-\chi)^3 - 0.226(1-\chi)^4 + 0.131(1-\chi)^5 - 0.042(1-\chi)^6 + 0.0046(1-\chi)^7$$

$$I_2(\chi) = -0.67\ln(1-\chi) - 1.004 + 1.576(1-\chi) - 1.093(1-\chi)^2 + 0.927(1-\chi)^3 - 0.603(1-\chi)^4 + 0.312(1-\chi)^5 - 0.152(1-\chi)^6 + 0.041(1-\chi)^7 - 0.004(1-\chi)^8$$

and

$$\chi = \frac{l\sin\beta}{b}$$

In seismology, a seismic moment is usually associated only with unstable fault movement. However, we note that the moment as defined in equation (5) is a calculatable quantity for both seismic and aseismic fault motion.

The final equation that is needed describes the unloading of the surrounding ground due to the propagation of slip along the normal fault. This drop in stress is due to the fact that the far field boundary conditions are imposed displacements rather than stresses. In our analysis, the particular quantity of interest is the drop in far field stress due to a unit increase in moment caused by the propagation of slip, $\partial\sigma/\partial M_o$ and referred to as the unloading factor. A large unloading factor represents 'stiff' ground conditions and can result in stable fault slip (like displacement controlled boundary conditions in laboratory tests). The unloading factor for the model in Figure 4 is calculated in Appendix C, and is given by:

$$\frac{\partial\sigma}{\partial M_o} = -\frac{(1+\nu)}{2\,d\,\sin\beta\cos\beta\,b\,t} \tag{6}$$

Equations (1) through (6) are sufficient to model slip along a normal fault in the Basin and Range. In the next section we model a documented earthquake to estimate some of the important parameters such as the shear fracture energy, and the horizontal stress in the absence of tectonic extension. These parameters are then used to look at faulting at Yucca Mountain.

Example of Hebgen Lake Earthquake

Both for the purposes of demonstrating the usefulness of the model, and estimating some of the unknown parameters, the results developed in the previous section are used to model an actual Basin and Range seismic event. A sequence of large earthquakes occurred in the Hebgen Lake, Montana region beginning on August 18, 1959. The largest earthquake in

the sequence, with $M_S = 7.5$, represents the largest earthquake to have occurred in the region in historic time (Doser, 1985). This earthquake is also one of the best documented Basin and Range earthquakes (e.g., Nolan, 1964). Inversion of the body wave amplitudes have revealed a moment tensor for the largest earthquake that is 84-88% double couple (Doser, 1985), which agrees with the pure double couple assumptions in our model. Short period body wave data indicates that the rupture began on a fault dipping approximately 60° near the base of the seismogenic zone (approximately 15 km depth), propagating upwards along a fault with a dip of approximately 50^0. Surface fault scarps indicate a fault width of approximately 19.6 km. Based on these results, we have assumed a plate thickness b of 15 km, width t of 19.6 km, and the normal fault with angle β of 60°. Other parameters that are fairly well constrained are the elastic properties of the ground, $E = 5 \times 10^{10}$ Pa and $\nu = 0.25$, and an average ground density $\rho g = 20{,}000$ Pa/m. Two of the parameters, d and l_o, cannot be accurately determined. d is the distance from the fault to the location where far field displacements are applied. The importance of this parameter is in its relation to the unloading factor (equation 6). d should be set to a value such that the applied displacements are outside the disturbance due to the propagation of the crack. The region of disturbance for an edge crack in a plate has a radius approximately equal to the length of the crack (Pollard and Segall ,1987, and others). Based on this, we have set $d = 15$ km. This is also consistent with the spacing between large normal faults in the Basin and Range. l_o is the initial length of the crack, and its value will influence the stress at which cracking will initiate (equation 3). Equation (3) shows that if l_0/b is small, the initiation of crack growth is controlled by G_c/l_0. The initial crack length, l_o, has been set to 10% of the plate width for the Hebgen Lake model (0.45 km), and for future analyses with different plate thicknesses, both G_c and l_o will be fixed so that G_c/l_0 remains constant.

The three important physical parameters that are not well constrained are the shear fracture energy, G_c, the coefficient of friction, μ_f, and the constant relating the horizontal in-situ stress perpendicular to the fault, F. We have made several runs with the model

varying these three parameters, starting with realistic values determined from other studies. For instance, for the shear fracture energy, G_c, we start with the value of 10^6 Joules/m^2 that is appropriate for strike slip faulting along the San Andreas (Wong, 1982). For the initial values for the coefficient of friction, μ_f and horizontal stress factor, F, we have chosen $\mu_f = 0.6$, and $F = 0.75$.

Approximately 30 runs were made varying the above three parameters within reasonable ranges, and comparing the model results with field data from the Hebgen Lake earthquake. The results of the model with $G_c = 5 \times 10^6$ J/m^2, $\mu_f = 0.6$, and $F = 0.6$ (and the remaining parameter values as given above) are presented in Figure 5. Figure 5 is a plot of the tectonic stress, σ, vs. the seismic moment, M_o. This figure describes the motion of the normal fault as the tectonic extension increases, giving both the aseismic and seismic deformation, and giving the seismic source parameters for unstable motion of the normal fault. The best way to understand the results in Figure 5 is to imagine going through an earthquake cycle, starting with only the gravity stresses and zero tectonic extension ($\sigma = 0$), and looking at the effects of increasing σ. Initially, with $\sigma = 0$, the surfaces of the crack are locked due to the high friction from the gravity forces. As σ is increased, the frictional forces are reduced, and the driving shear force along the crack is increased. The first effect of this is to unlock the crack faces at some value of σ (calculated from equation 1 with $K_{II} = 0$). Figure 5 shows that this occurs at a σ of 44 bars (point A in the figure). This is the initial frictional constraint, but as we will see, the friction changes as the slip event progresses.

Up to this point there has been no seismic moment since the crack faces were locked. Now, for a further increase in σ, there will be a linear increase in M_o, as given by equation (5) and shown in Figure 5. The deformation remains stable during this stage of deformation. This linear relation between σ and M_o is due to the fact that the crack is not propagating, and continues until the stress σ is increased to a point where the crack begins to propagate. The crack starts to propagate at $\sigma = 145$ bars, calculated from equation (3)

with $l = l_o$ and is shown as point B in Figure 5. As the crack propagates, the restriction that $G = G_c$ is maintained as the crack propagates results in a non-linear relationship between σ and M_o, as shown by the nonlinear curve following point B (referred to as the nonlinear stress-moment curve). This nonlinear curve is calculated from the simultaneous solution of equations (3) and (5) as the crack length increases from its initial value of l_o towards the ground surface.

Whether the crack propagates in a stable or unstable manner depends on the relationship between this nonlinear curve and the unloading of the surrounding ground. Equation (6) describes a linear relationship between the increase in moment, and the decrease in the far field driving stress, due to an incremental change in the length of the crack. For the parameter values used to model the Hebgen Lake earthquake, Figure 5 shows that the crack will initially unload faster than the surrounding ground (nonlinear curve is steeper at point B). Thus excess energy is being supplied to the crack by the surrounding ground, resulting in unstable crack growth. In this case, the crack continues to propagate in an unstable manner all the way to the ground surface, and the stress drops back to a new frictional level of approximately 20 bars. In other instances, depending on the relationship between the nonlinear stress-moment curve and the unloading factor, stable crack growth can be predicted, or initially stable crack growth that becomes unstable at some value of crack length.

Figure 5 gives the predicted source parameters for this unstable event. The predicted stress drop and moment are the changes in stress and moment that occur from the initiation of crack growth until the crack reaches the ground surface (from point B to point C in Figure 5). As shown in Figure 5, the predicted stress drop and moment are 125 bars and 4.6×10^{26} dyne-cm, respectively, which match reasonably well with the calculated moment of 1×10^{27} dyne-cm and an estimated stress drop of 110 bars made by Doser (1985).

The stress drop that the model predicts represents a drop in the far field tectonic extension in the region surrounding the crack. It is worthwhile to compare this with the stress drop calculated from the equation:

$$\Delta\sigma = \frac{8\ M_0}{3\ \pi\ t^2\ b} \tag{7}$$

which was used in Doser (1985) to estimate the stress drop for the Hebgen Lake earthquake. Equation (7) is actually not a measure of stress drop, but rather an estimate of the stress at which the rupture initiates, which correlates with point A in Figure 5 (calculated using equation 3). The agreement between the 'stress drop' measured by equation (7), and the actual drop in the far field stress as shown in Figure 5, is due to the fact that for a large normal faulting earthquake, the total far field stress is extinguished in the ground surrounding the normal fault. This is not the case, for instance, in moderate earthquakes along strike slip faults, where the drop in the far field stress may be only a percentage of the total available stress. In these cases the two estimates of stress drop will differ, as determined for slip of the Parkfield asperity by Kemeny (1988).

The strain energy change from the beginning of crack growth until the crack reaches the ground surface consists of two parts. The strain energy needed for the crack to grow is equal to G_c x the new crack surface area. This is equal to the area inside the nonlinear curve divided by 2μ and shown in Figure 5. Because the crack growth was unstable, there is excess energy available for seismic release, and this energy is proportional to the difference between the nonlinear curve and the linear unloading slope, also shown in Figure 5. Thus the nonlinear stress-moment curve divides these two parts of the total energy change. For the Hebgen Lake model in Figure 5, the nonlinear stress-moment curve reaches a maximum and turns around back toward the origin. This characteristic of the nonlinear stress-moment curve shows a very important aspect of the energy available

for seismic release as the crack propagates from its initial position towards the ground surface. At the beginning of the slip event, almost all of the available energy is taken up in the growth of the crack, with little excess energy available for seismic release. As the crack grows and approaches the ground surface, the crack interacts with the free surface. Because of the interaction effect, it takes much less energy to meet the $G = G_c$ criterion as the crack extends, only a very small amount of energy is required for the growth of the crack, and a large amount is available for seismic release. A similar effect is found for a rupturing asperity, which is important for strike slip and subduction type earthquakes (e.g., Kanamori, 1986).

Fault Segmentation

It is generally found that faults due not rupture over their whole lengths at once. This is well known for strike-slip faults such as the San Andreas fault. Fault segmentation refers to the individual segments that rupture along an earthquake fault. There are many reasons why fault segmentation might occur (irregularities in fault geometry, fault properties, and stress conditions), but this is an area where there are still many unknowns. Along the San Andreas in California, the two major segments where great earthquakes occur are separated by a 200 mile long creeping segment. Schwartz and Coppersmith (1986) present data on fault segmentation for normal faulting in the Basin and Range. Their data show a correlation between the length of the individual fault segments and the depth to which faulting occurs. Their data indicate that the length of the fault segments is on the order of the depth of faulting, and at most two times the depth of faulting. In the model presented in this paper, the length of the rupture segments is varied using the thickness of the plate t. For the Hebgen Lake model, the depth of faulting, b, was 15 km and the thickness t was 19.6 km, giving a t/b ratio of 1.3. In the next section, an analysis of faulting at Yucca Mountain is presented. In the analysis of faulting at Yucca Mountain, when the depth of faulting is varied, the thickness t will be varied to maintain t/b at 1.3.

Faulting at Yucca Mountain

The purpose of modelling a known earthquake was to get some idea of the three important unknown parameters, F, G_c, and μ_f, for slip events along normal faults in the Basin and Range. Using the properties determined from the Hebgen Lake analysis, we will try to predict the effects of a slip event at Yucca Mountain. One of the major unknowns at Yucca Mountain is whether or not a detachment fault exists at some depth below the surface. Yucca Mountain is cut by a series of steeply dipping normal faults. Whether or not these normal faults terminate at a shallow detachment surface or propagate to great depths is unresolved at the present time (see Figure 2). If these normal faults are associated with a shallow detachment surface at a depth of 2 - 4 km, then the possible moment, stress drop, and energy release could be significantly less than if the normal faults extend to depths of 10 km or more and are linked to movement at these depths. This is analyzed quantitatively by using the model in Figure 4, and using a fault depth, *b*, of only 3 km. As discussed in the previous section, the thickness *t* is taken to be 3.9 km, maintaining the *t/b* ratio identical to the Hebgen Lake analysis. Also, the distance *b* to where far field displacements are applied is modified to 3 km so that *b/d* is identical to the Hebgen Lake model. The remaining parameters for the Yucca Mountain model are identical to the parameters used for the Hebgen Lake model. The results of this are presented in Figure 6.

The results for faulting at Yucca Mountain in Figure 6 are presented in the same manner as the results for the Hebgen Lake in Figure 5. Starting from the body at rest with $\sigma = 0$ and increasing σ, the crack faces are unlocked at a value of σ equal to about 9 bars (point A in Figure 6). This is followed by linear stress-moment behavior up to the stress level of 114 bars where the crack begins to propagate (point B in Figure 6). Like the Hebgen Lake analysis, crack growth is unstable, and the instability (point B to point C) results in a moment of about 3×10^{24} dyne-cm and a drop in the far field stress of approximately 110 bars. The stress drop is slightly smaller, and this is due to the reduced friction effects at the

shallower depths. The seismic moment is related to the earthquake magnitude, and based on the empirical relationship given in Kanamori and Anderson (1975), a moment of 3 x 10^{24} represents and earthquake of magnitude 5.6. Thus the predicted slip event at Yucca Mountain is of a much smaller magnitude than the Hebgen Lake earthquake, but with a similar stress drop. The effects of the stress drop will be felt over a smaller area, and from the standpoint of water level changes, the changes should be of smaller magnitude. Da Costa (1964) found that for the Hebgen Lake, 1959 earthquake, groundwater level changes measuring several feet were measured near the epicenter. Changes of a smaller magnitude should be expected due to unstable fault motion on the normal faults at Yucca Mountain. Estimations of this are made in the next section.

The results in Figure 6 assumes that a shallow event occurs due to the presence of a detachment fault. If the detachment fault does not exist, or if it is older and dormant, then a deep-seated event is predicted. If a slip event at Yucca Mountain initiated at a depth of 15 km, our analysis would predict an event similar to the Hebgen Lake earthquake.

Water Level Changes due to Faulting

In both the models of faulting at Hebgen Lake and Yucca Mountain, a slip event results in an increase in horizontal compressive stress by values of about 110 bars. This will result in a squeezing of the rock, which could cause changes in the level of the water table. If the changes in the ground stress were due merely to a redistribution of stress, then the areas affected would be small, and the resulting changes in water levels would probably be low. However, our analysis indicates that based on the boundary conditions in the Basin and Range, the stress changes could be occurring over large areas, and the effects on the water table could be significant. For the Hebgen Lake earthquake, changes in regional stress over a region 30km x 19.6km x 15km is predicted. For a shallow event at Yucca Mountain initiated at a detachment fault, changes in regional stress over a region 6km x 3.9km x 3km is predicted. In order to estimate a value for the change in the level of the water table, all

the different mechanisms that contribute to these changes need to be determined. On the smallest level (micron to mm), an increase in compressive stress will cause a squeezing of pores and microcracks. On a larger scale (mm to m), the change in compressive stress will effect joints and small faults, and on the largest level (m to km), the changes in stress will effect large faults and shear zones. A simple model to take into account the above-mentioned effects considers the effects of changes in effective stress on changes in the fluid volume of spherical pores and penny shaped cracks. The formula for a penny shaped crack is especially useful, since by changing the radius of the crack, the effects of microcracks, joints, and faults can be considered. The change in volume, ΔV_p, of a spherical pore of volume V_p in an elastic solid of volume V, due to a change in effective hydrostatic stress, Δp, is given by (Walsh, 1965):

$$\Delta V_p = -\frac{9}{2}\frac{\Delta p}{E}\frac{V_p\,(1 - \nu)}{1 - \frac{V_p}{V}} \tag{8}$$

where E is Young's modulus and ν is Poisson's ratio.

The change in volume, ΔV_c, of a penny shaped crack of radius c, due to a change in effective hydrostatic stress, Δp, is given by:

$$\Delta V_c = -\frac{16}{9}\frac{\Delta P}{E} c^3 (1 - \nu^2) \tag{9}$$

As an example of the importance of equations (8) and (9), consider a 1 km^3 block of saturated rock subjected to an increase in hydrostatic compressive stress of 110 bars, and assume a Young's modulus of 5×10^{10} Pa, Poisson's ratio of 0.25, and a porosity of 25%. Using equation (8), the application of 110 bars pressure results in closing of the pores by .10%. Assuming that all the porosity is connected and fully saturated with fluid, this would result in 250,000 m^3 of fluid that must be displaced out of the block. If we assume that all of this fluid were to be displaced upward and not outward or downward,

then this represents an increase in the water level of 0.25 m. For the Hebgen Lake earthquake where the region of influence is over a depth of 15 km, this represents an increase in the water table of 3.75 m, and for a shallow faulting event at Yucca Mountain that influences the rock to a depth of 3 km, this represents an increase of the water table of 0.75 m. The predicted value for the Hebgen Lake earthquake agrees with Da Costa (1964). Thus it appears that following an earthquake, the squeezing of pores alone not enough to cause a significant water level change.

The effect of regional stress changes on faults could is potentially more serious. Consider a penny-shaped fault of radius 1 km that is saturated and subjected to 110 bars of compressive stress. Using E and ν as above and equation (9), this results in 370,000 m^3 of fluid that is displaced from the fault. It is likely that this fluid will flow up along the fault, since the fault is probably more permeable than the surrounding ground (this is especially likely for the fault that results in the slip event). Assuming a fault zone 10 m wide and 1 km in length with a porosity of 40%, the fluid would be able to rise in the fault zone 92 m. Thus even for this small fault of only 1 km radius, the possible rise in fluid level is significant. Factors that could result in even greater rises in the fault would be a fault with a larger radius (for instance 5 km radius instead of 1) or fluids from pore squeezing getting into the fault zones. Factors that would decrease the effect would be draining of the fluid into the surrounding rock as it rises along the fault zone. A major factor that would decrease the significance of the effect is the fact that an open crack of radius 1 km filled with fluid is not very realistic of actual faults in the field. If we consider instead the fault to be made up of 10^6 cracks each of radius 1 m, then the area of total fault surface is the same, but only one thousandth the volume of fluid (370 m^3) is displaced, and the predicted rise along the fault zone under the same conditions discussed above is less than a tenth of a meter (0.092m).

Discussion

Up to this point, only the effects of a single slip event on a normal fault in the Basin and Range has been considered. This by itself is an important problem, and it was shown that the consequences of this slip include an unstable event of measurable magnitude, a drop in the tectonic stress, and a rise in the level of the water table. Additional problems that can be considered include the recurrence interval for repeated events on a single fault, and how the overall extension in the Basin and Range is shared by neighboring faults. Based on Minster and Jordan (1987), the Basin and Range is extending at an average rate of approximately 9 mm/year. If assumptions are made about how faults reheal after a slip event, and how the extension rate of 9 mm/yr is distributed in the Basin and Range, then predictions of recurrence intervals for slip events can be made.

The simplest model for restrengthening assumes that the fault regains its strength (crack length reset to l_0) immediately following a slip event. The recurrence interval is then the time that it takes for the stress to build up to the critical stress for cracking of the crack of length l_0 to occur (point A to point B in Figure 6). Assuming that the extension in the Basin and Range is evenly distributed, the 6 km wide Yucca Mountain model is extending at a rate of approximately 0.045 mm/yr. Based on the elastic properties for the Yucca Mountain ground given previously, an extension of 1.32 meters is required to build the tectonic stress in the Lithosphere up to the level where cracking will initiate. This gives a recurrence interval for repeated slip events on normal faults at Yucca Mountain of 29,300 years. A major drawback with this calculation is that this same recurrence interval is calculated for repeated slip events along all normal faults in the Basin and Range. This follows from the assumption that the extension is equally distributed in the Basin and Range. Field strain measurements or trenching along faults is necessary to determine the actual distribution of strain buildup in the Basin and Range.

Conclusions

A mechanical model has been developed to calculate the effects of repeated slip events along pre-existing normal faults in the Basin and Range. Depending on the boundary conditions and material properties of the ground, these slip events can result in aseismic and/or seismic events. It is known that slip along pre-existing normal faults are responsible for great earthquakes in the Basin and Range, such as the magnitude 7.5 earthquake at Hebgen Lake, Montana on August 18, 1959, and the magnitude 7.3 earthquake at Borah Peak, Idaho on October 28, 1983. The mechanical model consists of a two dimensional linear elastic plate containing an edge crack at an angle β from horizontal. The plate is loaded by gravity forces and tectonic extension. Friction along the crack surface is also considered. A normal faulting slip event is modelled as the propagation of the crack from its initial position towards the free surface. The model calculates the aseismic and seismic deformation due to the propagation of slip along the normal fault, and the moment and energy release associated with seismic motion. Also, the model calculates regional stress changes associated with a slip event, from which changes in the level of the water table are estimated. The model is calibrated by modelling the magnitude 7.5 Hebgen Lake, Montana earthquake of August 18, 1959. The model is then used to predict the effects of a slip event on normal faults in the vicinity of Yucca Mountain, Nevada, which is the proposed site for underground nuclear waste storage. Assuming that slip initiates from a shallow, low angle detachment fault near Yucca Mountain, an unstable event with a seismic moment of 3×10^{24} dyne-cm and a stress drop of 110 bars is predicted. Based on this stress drop, a rise in the water table is predicted. If only the effects of the squeezing of pores are considered, then the predicted rise in the water table is approximately 0.75 meters. However, if the effects of the stress drop on a saturated fault is considered, a rise in the water level along the fault of over 90 meters is estimated. Based on a uniform extension rate in the Basin and Range of 9 mm/year, and assuming that this extension is distributed evenly over the Basin and Range, the model predicts a recurrence interval for slip along normal faults in the vicinity of Yucca Mountain of 29,300 years.

Appendix A - Derivation of the Mode II Stress Intensity Factor

The mode II stress intensity factor solution for the model in Figure 4 is based on the solution for an edge crack of length l at right angles to the free surface in a body of width b, and subjected to shear tractions, τ, at the ends of the body. This solution is given by (Tada et al., 1973):

$$K_{II} = \tau \sqrt{\pi l}\ Y_{II}(l/b) \tag{A1}$$

where

$$Y_{II}(l/b) = \frac{1.12 - 0.56(l/b) + 0.085(l/b)^2 + 0.180(l/b)^3}{\sqrt{1-l/b}}$$

The function $Y_{II}(l/b)$ takes into account interaction effects as the edge crack approaches the opposing free surface. Equation (A1) is modified to account for the edge crack at an angle β as in Figure 4, and subjected to a tensional stress, σ, rather than shear along the boundaries of the body. The mode II stress intensity factor results from the shear component along the edge crack due to σ ($\sigma \sin\beta \cos\beta$). It is assumed that the interaction effect, $Y_{II}(l/b)$, is the same as long as it is evaluated as $Y_{II}(\frac{l\sin\beta}{b})$. Based on the above solution, the stress intensity factor becomes:

$$K_{II}^{tect} = \sigma \sin\beta\cos\beta \sqrt{\pi l}\ Y_{II}(\frac{l\sin\beta}{b}) \tag{A2}$$

Equation (A2) is the K_{II} solution for tectonic extension. This solution has been checked against numerical solutions to the edge crack at angle β under tension, and it agrees within 5% for $l\frac{l\sin\beta}{b}$ up to 0.95. Next the effects of gravity are taken into account. a vertical

stress due to gravity of ρgz, and a horizontal stress due to gravity of $F\rho gz$ are assumed, where F is a constant, and where z varies from 0 to b. These represent linearly varying loads in both the horizontal and vertical directions. The solution for an edge crack with a linearly varying load from 0 at the crack tip to σ at the edge is 0.44 times the solution for a constant σ across the whole crack (Tada et al., 1973). From this relationship and some algebraic manipulation, the mode II stress intensity factor for the gravity loads becomes:

$$K_{II}^{grav} = \rho g b \left(1.12 - 0.68\frac{l\sin\beta}{b}\right)(1 - F)\sin\beta\cos\beta\sqrt{\pi l}\ Y_{II}\left(\frac{l\sin\beta}{b}\right) \tag{A3}$$

Equation (A3) is the K_{II} solution due to gravity. The final component of the stress intensity factor is that due to friction. Friction along the edge crack is given by $\sigma_n\mu_f$, where μ_f is the coefficient of friction and σ_n is the compressive stress acting normal to the crack. The normal force has components due to the vertical and horizontal gravity loads, and also the tectonic extension. After some manipulation, the stress intensity factor for the friction forces becomes:

$$K_{II}^{frict} = -\sigma_n\mu_f \sin\beta\cos\beta\sqrt{\pi l}\ Y_{II}\left(\frac{l\sin\beta}{b}\right) \tag{A4}$$

where

$$\sigma_n = \left[\sigma - \rho g b\ (1.12 - 0.68\chi)\left(\frac{1}{\tan^2\beta} + F\right)\right]\sin^2\beta$$

By superposition, the total stress intensity factor is given by:

$$K_{II}^{tot} = K_{II}^{tect} + K_{II}^{grav} + K_{II}^{frict} \tag{A5}$$

as given in equation (1).

Appendix B - Calculation of Seismic Moment

The seismic moment is proportional to the average shear displacements along the crack surface, given by equation (4). The average displacements can be calculated by using the relationship between K_{II} and the crack energy, given by equation (2), and an energy theorem such as Castigliano's theorem (Sokolnikoff, 1956). This can be put in the form:

$$\bar{\delta} = \frac{1}{2l}\frac{\partial}{\partial\sigma}\left[\frac{1}{E}\int_0^l K_{II}^2\, dl\right] \tag{B1}$$

The mode II stress intensity factor given in equation (1) is plugged into equation (B1), and the derivative with respect to σ is taken. After some algebraic manipulation, it remains to solve the two integrals:

$$I_1 = \int_0^{\chi} l\, Y_{II}^2\, dl$$

and (B2)

$$I_2 = \int_0^{\chi} l^2\, Y_{II}^2\, dl$$

where

$$\chi = \frac{l\sin\beta}{b}$$

and where Y_{II} is the part of the stress intensity factor that takes into account interaction effects and is given in equation (1). The solutions to these two integrals are given below equation (5). The seismic moment, M_0, is calculated from $\bar{\delta}$ by using equation (4). The result is presented in equation (5).

Appendix C - Calculation of Unloading Factor

The far field stress, σ, is first put in terms of the average displacement of the crack, $\bar{\delta}$. This gives:

$$\sigma = \frac{E\ \bar{\delta}}{2b\sin\beta\cos\beta} \tag{C1}$$

Using (4), this is put in terms of the seismic moment:

$$\sigma = \frac{(1 + \nu)\ M_o}{2d\sin\beta\cos\beta\ b\ t} \tag{C2}$$

Taking the derivative of this with respect to M_o gives the unloading factor as given in equation (6).

Acknowledgements

The helpful comments by Neville G. W. Cook and Larry Myer are greatly appreciated. This work was partially supported by the U. S. Department of Energy under contract DE-AC03-76SF00098.

References

Aki, K., and Richards, P. G. 1980. Quantitative Seismology, Freeman and Co., NY.

Andrews, D.J. 1978. Coupling of energy between tectonic processes and earthquakes. *J. Geophys. Res.* **83**:2259-2264.

Da Costa, J. A. 1964. Effect of Hebgen Lake earthquake on water levels in wells in the United States. U.S. Geological Survey Professional Paper 435-O, U.S.G. S., Washington, D.C.

Davis, G. A., and Lister, G. S. 1988. Detachment faulting in continental extension; perspectives from the southwestern U.S. cordillera. Geological Society of America, Special Paper 218, 133-159.

Detournay, E., and Cheng, A. H-D. 1988. Poroelastic response of a borehole in a non-hydrostatic stress field. *Int. J. Rock Mech. Min. Sci. & Geomech. Abstr.* **25**, 171-182.

DOE, 1988a. Site Characterization Plan Overview, U.S. Department of Energy report DOE/RW-0198.

DOE, 1988b. Yucca Mountain Site Visit UNR Briefing Package, U.S. Department of Energy, May 9, 1988.

Doser, D. I. 1985. Source parameters and faulting processes of the 1959 Hebgen Lake, Montana, earthquake sequence. *J. Geophys. Res.* **90**, 4537-4555.

Doser, D. I., and Smith, R. B. 1985. Source parameters of the 28 October 1983 Borah Peak, Idaho, earthquake from body wave analysis. *Bull. Seism. Soc. Am.* **75**, 1041-1051.

England, P. and Jackson, J. 1987. Migration of the seismic-aseismic transition during uniform and nonuniform extension of the continental lithosphere. *Geology* **15**, 291-294.

Hamilton, W. 1987. Crustal extension in the Basin and Range province, southwestern United States. *From* Coward, M. P., Dewey, J. F., and Hancock, P. L. (eds), *Continental Extensional Tectonics*, Geological Society Special Publication No. 28, 155-176.

Jaeger, J. C. and Cook, N. G. W. 1979. *Fundamentals of Rock Mechanics*, Chapman and Hall, London.

Johnson, A.G., Kovach, R. L., Nur, A., and Booker, J.R. 1973. Pore pressure changes during creep events on the San Andreas Fault. *J. Geophys. Res.* **78**:851-857.

Kanamori, H. 1986. Rupture processes in subduction-zone earthquakes, *Ann. Rev. Earth Plan. Sci.*, **14**, 293-322.

Kanamori, H., and Anderson, D.L. 1975. Theoretical basis of some empirical relations in seismology. *Bull. Seis. Soc. Am.* **65**:1073-1095.

Kemeny, J.M. 1988. The mechanics of asperity failure using realistic boundary conditions. *EOS*, **69**:1448.

Kemeny, J. M. and Cook, N. G. W. 1986. Frictional stability of heterogeneous surfaces in contact. 27th U.S. Rock Mechanics Symposium. Society of Mining Engineers, Littleton, CO., 40-46.

Kemeny, J. M. and Cook, N. G. W. 1987. Determination of rock fracture parameters from crack models for failure under compression. 28th U.S. Rock Mechanics Symposium. A.A. Balkema, Rotterdam, 367-374.

Lawn, B. R. and Wilshaw, T. R. 1975. *Fracture of Brittle Solids*. Cambridge University Press, London.

Li, V.C., and Rice, J.R. 1987. Crustal deformation in great California earthquake cycles. *J. Geophys. Res.* **92**:11533-11551.

Li, V. C., Seale, S. H., and Cao, T. 1987. Postseismic stress and pore pressure readjustment and aftershock distributions. *Tectonophysics* **144**, 37-54.

Lin, J. and Parmentier, E, M. 1988. Quasistatic propagation of a normal fault: a fracture mechanics model. *J. Struct. Geology* **10**, 249-262.

Martel, S.J., and Pollard, D.D. 1989. Mechanics of slip and fracture along small faults and simple strike-slip fault zones in granitic rock. *J. Geophys. Res.* **94**:9417-9428.

Minster, J.B., and Jordan, T.H. 1987. Vector constraints on western U.S. deformation from space geodesy, neotectonics, and plate motions. *J. Geophys. Res.* **92**:4798-4804.

McGarr, A. 1988. On the state of lithospheric stress in the absence of applied tectonic forces. *J. Geophys. Res.* **93**, 13609-13617.

Nolan, T. B. 1964. The Hebgen Lake, Montana Earthquake of August 17, 1959. U.S. Geological Survey Professional Papers 435A-T, U.S.G. S., Washington, D.C.

Pollard, D.D., and Segall, P. 1987. Theoretical displacements and stresses near fractures in rock: with applications to faults, joints, veins, and solution surfaces, in Fracture Mechanics of Rock, B.K. Atkinson, ed., Academic Press, London, pp. 277-349.

Rice, J. R., and Cleary, M. P. 1976. Some basic stress diffusion solutions for fluid-saturated elastic porous media with compressible constituents. *Rev. Geophys. and Space Phys.* **14**, 227-241.

Schwartz, D.P., and Coppersmith, K.J. 1986. Seismic hazards: new trends in analysis using geologic data, Chapter 14 in Active Tectonics - Studies in Geophysics, National Academy Press, Washington, D.C. pp. 215-230.

Scott, R. B. 1986. Extensional tectonics at Yucca Mountain, southern Nevada, *Geological Society of America Abstracts with Programs*, **18**, p. 411.

Sibson, R. H. 1981. Fluid flow accompanying faulting: field evidence and models. *From* Simpson, D. W. and Richards, P. G. (eds), *Earthquake Prediction: an International Review*, AGU, Washington, D. C.

Sibson, R. H. 1982. Earthquake rupturing as a mineralizing agent in hydrothermal systems. *Geology* **15**, 701-704.

Smith, R. B., and Bruhn, R. L. 1984. Intraplate extensional tectonics of the eastern Basin-Range: Inferences on structural style from seismic reflection data, regional tectonics, and thermal-mechanical models of brittle-ductile deformation, *J. Geophysical Res.*, **89** 5733-5762.

Sokolnikoff, I.S. 1956. Mathematical Theory of Elasticity. Krieger Pub. Co., Malabar, Florida.

Stein, R. S., and Barrientos, S. E. 1985. Planar high-angle faulting in the Basin and Range: geodetic analysis of the 1983 Borah Peak, Idaho, earthquake. *J. Geophys. Res.* **90**, 11355-11366.

Tada, H., Paris, P. C., and Irwin, G. R. 1973. *The Stress Analysis of Cracks Handbook*, Del Research Corp., Hellertown.

Turcotte, D.L., Clancy, R.T., Spence, D.A., and Kulhawy, F.H. 1979. Mechanisms for the accumulation and release of stress on the San Andreas fault. *J. Geophys. Res.* **84**:2273-2282.

Walsh, J.B. 1965. The effect of cracks on the compressibility of rock. *J. Geophys. Res.* **70**:381-389.

Wong, T.-f. 1982. Shear fracture energy of Westerly granite from post-failure behavior. *J. Geophys. Res.* **87**, 990-1000.

Wong T.-f. 1986. On the normal stress dependence on the shear fracture energy. In *Earthquake Source Mechanics*, Geophysical Monograph 37, AGU, Washington, D. C.

Zoback, M. L., Anderson, R. E., and Thomson, G. A. 1981. Cainozoic evolution of the state of stress and style of tectonism of the Basin and Range province of the western United States. *Phil. Trans. R. Soc. Lond.* A **300**, 407-434.

Zoback, M. L. and Zoback, M. 1980. State of stress in the conterminous United States. *J. Geophys. Res.* **85**, 6113-6156.

Figure Captions

Figure 1. East-West cross section through Yucca Mountain, showing the proposed nuclear waste repository in relation to local normal faults and the water table (redrawn from DOE, 1988a).

Figure 2. Two scenarios for the downward extension of normal faults in the vicinity of Yucca Mountain. In a), the faults continue straight, and in b), the normal faults become listric and merge into a detachment fault (redrawn from DOE, 1988b).

Figure 3. The effect of a slip event on a pre-existing normal fault in the Basin and Range. The stress state in the elastic Lithosphere is the superposition of compressive stresses due to gravity, and tensile stresses due to viscous extension at depth (figure a). A slip event will reduce the tensile stresses while the stresses due to gravity remain unchanged (figures b and c). The result is an increase in compressive stress due to slip along normal faults in the Basin and Range.

Figure 4. Mechanical model for a slip event along a pre-existing normal fault in the Basin and Range. The normal is represented by the angle crack, and a slip event along the normal fault is modelled as the propagation of the crack from its initial position towards the top of the plate.

Figure 5. Analysis of the 1959 Hebgen Lake earthquake using the model in Figure 4 (parameter values given in text). Slip between the surfaces of the initial crack initiates at point A, and crack propagation starts at point B. Unstable rupture (point B to point C) results in a seismic moment of about 4.6×10^{26} dyne-cm and a stress drop of about 125 bars.

Figure 6. Analysis of a slip event along normal faults at Yucca Mountain, assuming a detachment fault at a depth of 3 km. The other parameter values are from the Hebgen Lake analysis. The unstable rupture (point B to point C) results in a seismic moment of about 3×10^{24} dyne-cm and a stress drop of about 110 bars.

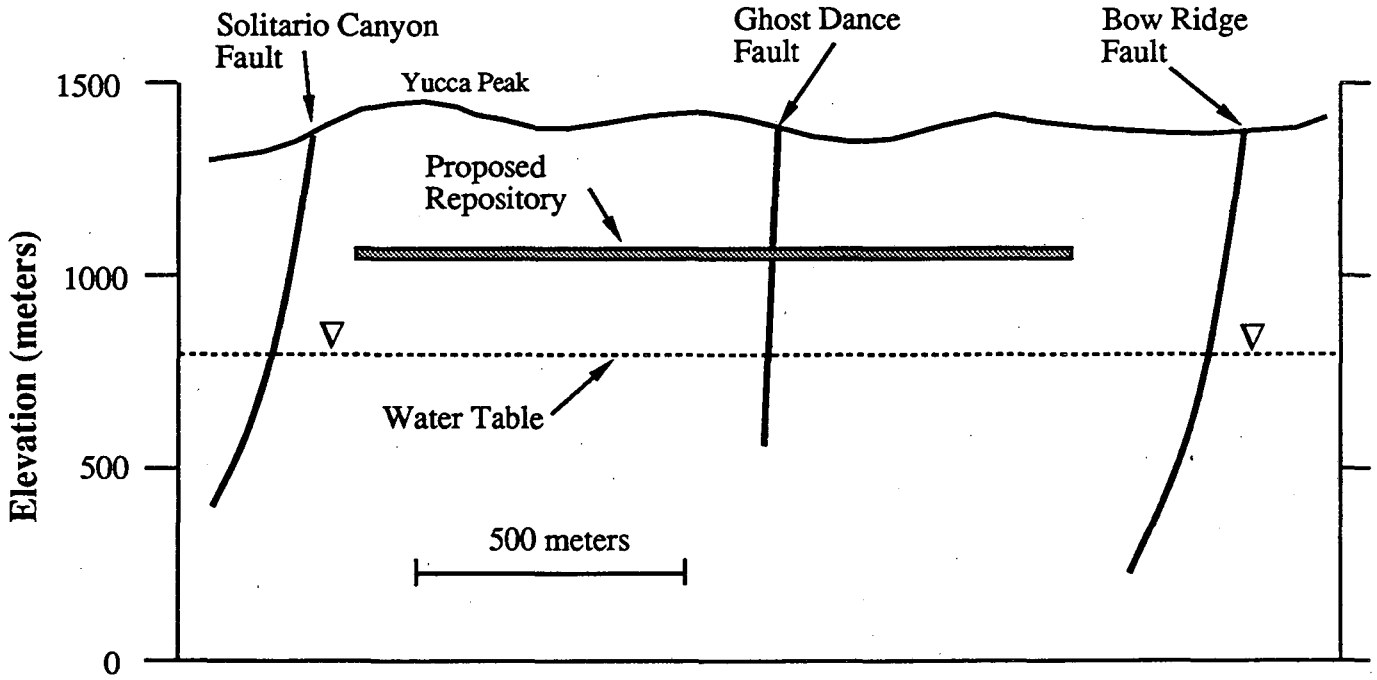
Solitario Canyon Fault
Ghost Dance Fault
Bow Ridge Fault
Yucca Peak
Proposed Repository
Water Table
500 meters
Elevation (meters)
1500
1000
500
0

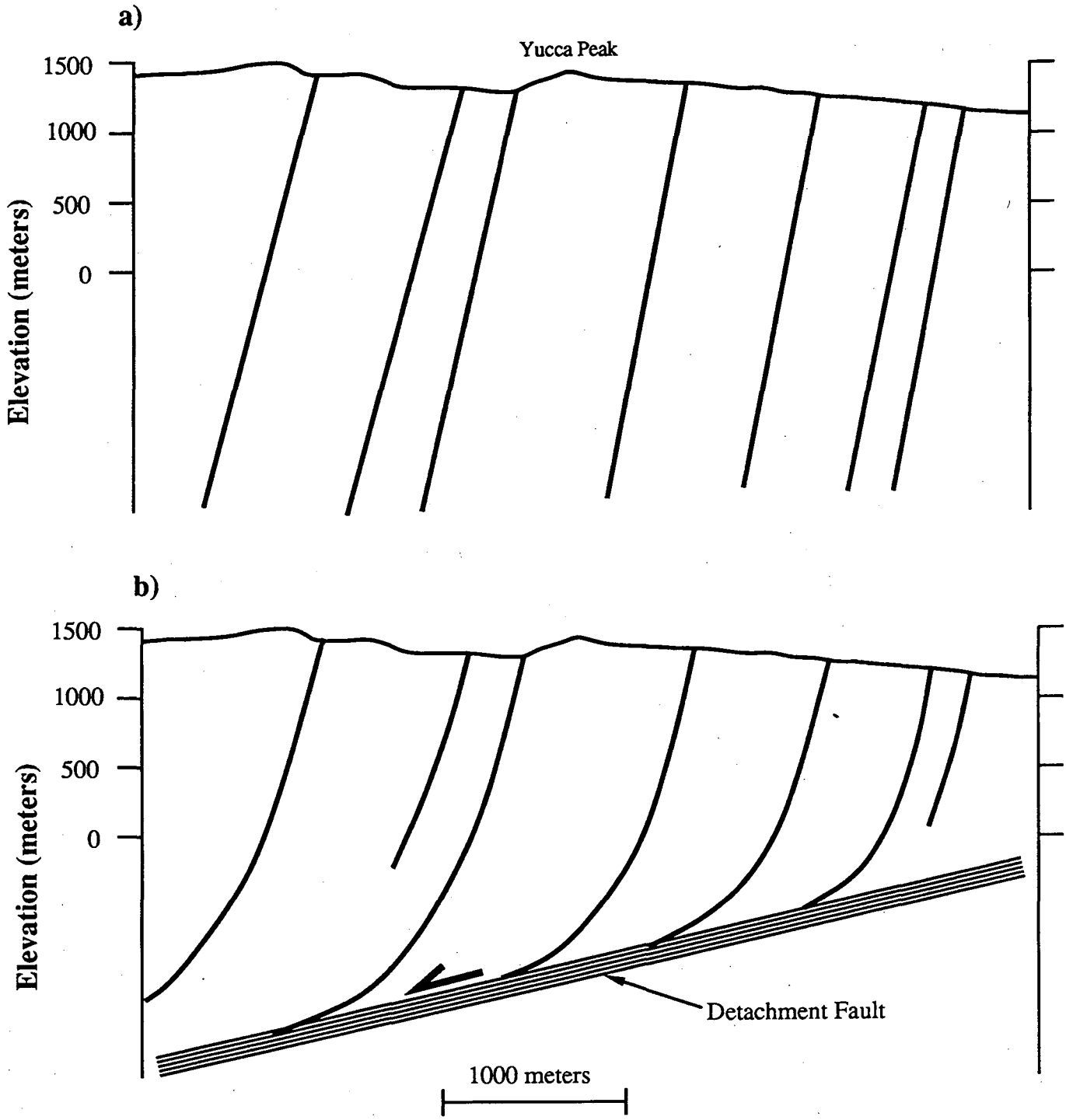
a)
Yucca Peak
1500
1000
500
0
Elevation (meters)
b)
1500
1000
500
0
Elevation (meters)
Detachment Fault
1000 meters

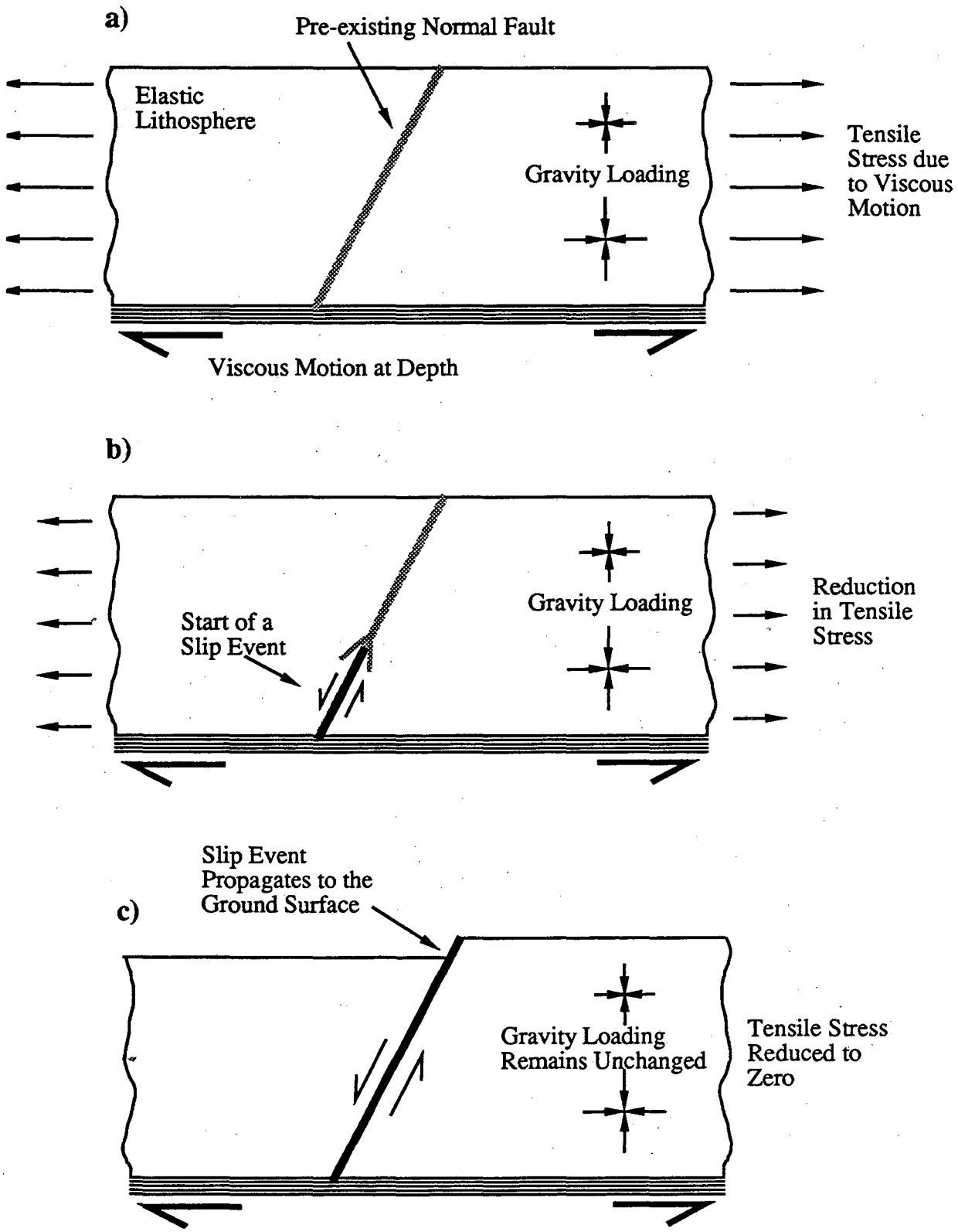
a)
Pre-existing Normal Fault
Elastic
Lithosphere
Gravity Loading
Tensile
Stress due
to Viscous
Motion
Viscous Motion at Depth
b)
Start of a
Slip Event
Gravity Loading
Reduction
in Tensile
Stress
c)
Slip Event
Propagates to the
Ground Surface
Gravity Loading
Remains Unchanged
Tensile Stress
Reduced to
Zero

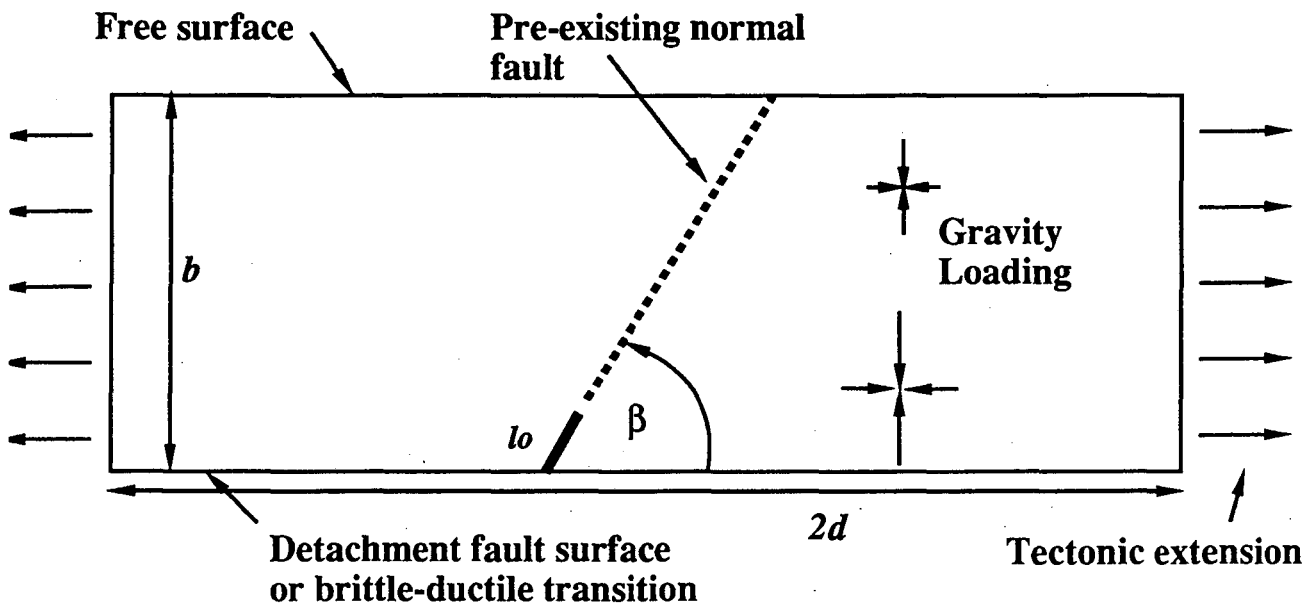
Free surface
Pre-existing normal fault
b
Gravity Loading
lo
β
2d
Detachment fault surface or brittle-ductile transition
Tectonic extension

Figure 4

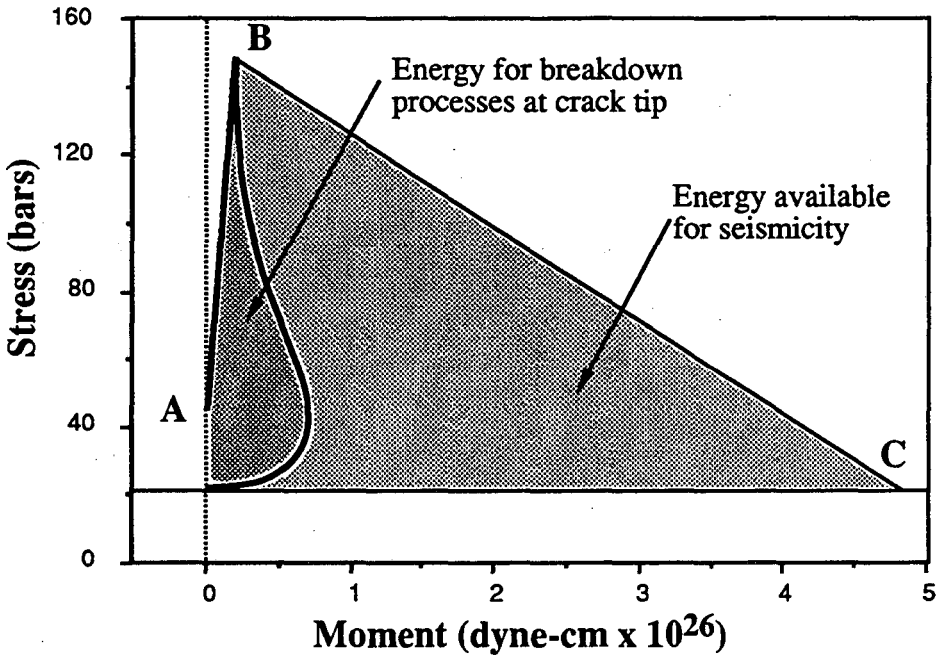
160
120
80
40
0
Stress (bars)
B
A
C
Energy for breakdown
processes at crack tip
Energy available
for seismicity
0
1
2
3
4
5
Moment (dyne-cm x 10^26)

Figure 5

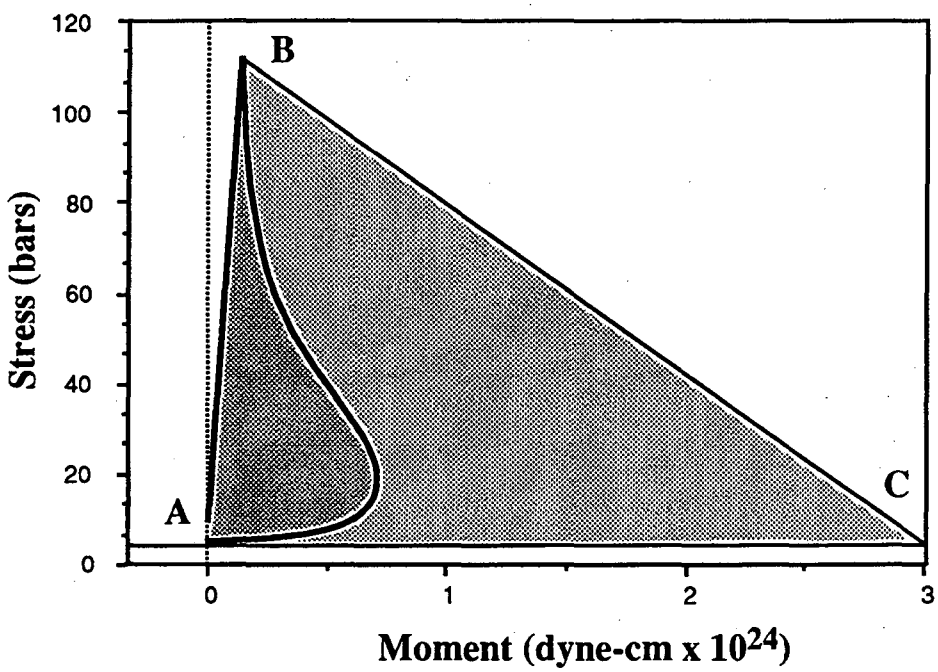

Figure 6

Lawrence Berkeley Laboratory
Geologic Repository Project (GRP)
Publications List — Alphabetical, 1986–1989

Asch, T., and Morrison, H. F., "Mapping and monitoring electrical resistivity with surface and subsurface electrode arrays," Geophysics, Vol. 54, No. 2, pp. 235-244, 1989.

Carnahan, C. L., "Coupling of precipitation/dissolution reactions to mass diffusion", report LBL-26183, Chemical Modeling in Aqueous Systems II Symposium, 196th National Meeting of American Chemical Society, Division of Geochemistry, Los Angeles, CA, Sept. 25-30, 1988.

Daley, T. M., McEvilly, T. V., and Majer, E. L., "Multiply-polarized shear-wave VSPs from the Cajon Pass drillhole," report LBL-25289, submitted to Geophysical Research Letters, 1988.

Ewy, R. T., Cook, N. G. W., and Myer, L. R., "Hollow cylinder tests for studying fracture around underground openings," report LBL-25308, 29th U.S. Symposium on Rock Mechanics, University of Minnesota, 1988.

Ewy, R. T., Kemeny, J., Zheng, Z., and Cook, N. G. W., "Generation and analysis of stable excavation shapes under high rock stresses," report LBL-22747, Proceedings of 6th International Congress on Rock Mechanics, Montreal, Canada, Vol. II, pp. 875-881, 1987.

Flueh, E. R., Mooney, W. D., Fuis, G. S., and Ambos, E. L., "Crustal structure of the Chugach Mountains, Southern Alaska: A study of pegleg multiples from a low velocity zone," report LBL-24699, Journal of Geophysical Research, Vol. 94, No. B11, pp. 16,023-16,035, 1989.

Flueh, E. R., and Okaya, D. A. "Near-vertical and intermediate offset seismic reflection data from west of the Whipple Mountains, SE California," report LBL-24641, Journal of Geophysical Research, Vol. 94, No. B1, pp. 625-639, 1989.

Gajewski, D., and Psencik, I., "Vertical Seismic Profile Synthetics by Dynamic Ray Tracing in Laterally Varying Layered Anisotropic Structures", report LBL-27739, submitted to Journal of Geophysical Research, 1989.

Hopkins, D. L., Cook, N. G. W., and Myer, L. R., "Fracture stiffness and aperture as a function of applied stress and contact geometry," report LBL-25312, 28th U.S. Symposium on Rock Mechanics, Tucson, AZ, June 29-July 1, 1987.

Javandel, I., "On the Field Determination of Effective Porosity," Invited Paper, Proceedings of Conference on New Field Techniques for Quantifying the Physical and Chemical Properties of Heterogeneous Aquifers, Dallas, Texas, pp. 155-171, March 20-23, 1989.

Kemeny, J., and Cook, N. G. W., "Frictional stability of heterogeneous surfaces in contact," report LBL-25313, Proceedings of the 27th U.S. Rock Mechanics Symposium, Tuscaloosa, AL, 1986.

Kemeny, J., and Cook, N. G. W., "Crack models for the failure of rocks in compression," report LBL-25311, Proceedings 2nd International Conference Constitutive Laws for Engineering Materials, C.S. Desai et al., editors, Elsevier Science Publ. Co., Inc., NY, pp. 879-887, 1987.

Kemeny, J., and Cook, N. G. W., "The origin of slip weakening along faults in rocks," report LBL-25306, submitted to Mechanics of Materials.

Kemeny, J., and Cook, N. G. W., "Constraints on moment, stress drop and strain energy release due to slip weakening," report LBL-25306, in preparation.

Meike, A., "Specimen cage modification for TEM in-situ shearing, report LBL-24145, Proceedings Materials Research Society, Fall Meeting, 1988.

Moreno, L., Tsang, Y. W., Tsang, C. F., Hale, F. V., and Neretnieks, I., "Flow and tracer transport in a single fracture: A stochastic model and its relation to some field observations," report LBL-25049, Water Resources Research, Vol. 24, No. 12, pp. 2033-2048, 1988.

Muralidhar, K., and Long, J. C. S., "A scheme for calculating flow in fractures using numerical grid generation in three-dimensional domains of complex shapes," report LBL-24453, September 1987.

Pyrak-Nolte, L. J., and Cook, N. G. W., "Fluid percolation through single fractures," Geophysical Research Letters, Vol. 15, No. 11, pp. 1247-1250, 1988.

Pyrak-Nolte, L. J., Cook, N. G. W., and Myer, L. R., "Seismic visibility of fractures," report LBL-25310, Proceedings of 28th U. S. Symposium on Rock Mechanics, Tucson, AZ, pp. 47-51, 1987.

Pyrak-Nolte, L. J., Myer, L. R., and Cook, N. G. W., "Transmission of seismic waves across single fractures," report LBL-26616, to be submitted to Journal of Geophysical Research.

Pyrak-Nolte, L. J., Myer, L. R., Cook, N. G. W., and Witherspoon, P. A., "Hydraulic and mechanical properties of natural fractures in low permeability rock," report LBL-22718, Proceedings of 6th International Congress on Rock Mechanics, Montreal, Canada, Vol. 1, pp. 225-232, 1987.

Tsang, C. F., "A new approach to tracer transport analysis: From fracture systems to strongly heterogeneous porous media," Keynote address, International Workshop on Appropriate Methodologies for Development and Management of Groundwater Resources in Developing Countries, Hyderabad, India, Feb. 28-Mar. 4, 1989.

Tsang, C. F., "Tracer travel time and model validation," report LBL-26518, Invited Paper, American Nuclear Society Annual Meeting, San Diego, California, June 13-16, 1988, to be published in the International Journal of Radioactive Waste Management and the Nuclear Fuel Cycle, 1989.

Tsang, C. F., Tsang, Y. W., and Hale, F. V., "Tracer transport in fractured rocks," report LBL-25657, Invited Paper, Proceedings of International Conference on Flow in Fractured Rocks, Atlanta, Georgia, May 16-18, 1988.

Tsang, Y. W. and Hale F. V., "A study of the application of mercury porosimetry method to a single fracture," report LBL-25489, Proceedings of International Conference on Flow in Fractured Rocks, Atlanta, Georgia, May 16-18, 1988.

Tsang, Y. W., and Tsang, C. F., "Channel model of flow through fractured media," report LBL-21310, Water Resources Research, Vol. 23, No. 3, pp. 467-479, 1987.

Tsang, Y. W., and Tsang, C. F., "Flow channeling in a single fracture as a two-dimensional strongly heterogeneous permeable medium," report LBL-26596, Water Resources Research, Vol. 25, No. 9, pp. 2076-2080, 1989.

Tsang, Y. W., Tsang, C. F., Hale, F. V., Moreno, L., and Neretnieks, I., "Channeling characteristics of flow and solute transport through a rough-surfaced fracture," report LBL-23195, June 1987.

Tsang, Y. W., Tsang, C. F., Neretnieks, I., and Moreno, L., "Flow and tracer transport in fractured media--A variable-aperture channel model and its properties," report LBL-25048, Water Resources Research, Vol. 24, No. 12, pp. 2049-2060, 1988.

Wollenberg, H. A., and Flexser, S., "Evidence for mobility of uranium in fractured, heated rock," report LBL-26137, submitted to Applied Geochemistry, 1988.

Zheng, Z., Kemeny, J., and Cook, N. G. W., "Analysis of wellbore breakouts," report LBL-23941, Journal of Geophysical Research, Vol. 94, No. B6, pp. 7171-7182, 1989.

Zheng, Z., Myer, L. R., and Cook, N. G. W., "Borehole breakout and stress measurements," report LBL-25655, Proceedings, 29th U.S. Symposium on Rock Mechanics, University of Minnesota, 1988.

LAWRENCE BERKELEY LABORATORY
UNIVERSITY OF CALIFORNIA
TECHNICAL INFORMATION DEPARTMENT
BERKELEY, CALIFORNIA 94720

ABG984
LBL Libraries